Energy Transfer in Organic-Inorganic Semiconductor Structures

Dissertation

zu Erlangung des akademischen Grades

Doctor Rerum Naturalium
(Dr. rer. nat.)
im Fach Physik
Spezialisierung: Experimentalphysik

eingereicht an der

Mathematisch-Naturwissenschaftlichen Fakultät

Institut für Physik

Humboldt-Universität zu Berlin

von

M.Sc. Francesco Bianchi

Präsidentin der Humboldt-Universität zu Berlin:
Prof. Dr.-Ing. habil. Dr. Sabine Kunst

Dekan der Mathematisch-Naturwissenschaftlichen Fakultät:
Prof. Dr. Elmar Kulke

Gutachter/innen:

1. Prof. Oliver Benson
2. Dr. Sylke Blumstengel
3. Prof. Francesco Meinardi

Tag der mündlichen Prüfung: 29. Juni 2018

CONTENTS

LIST OF FIGURES

ABSTRACT

Energy Transfer in Organic-Inorganic Semiconductor Structures

Hybrid inorganic/organic structures (HIOS) are promising candidates for achieving new and improved opto-electronic functionalities. Taking advantage of the complementary beneficial properties of two different material classes.
In HIOS structures based on a quantum well and an adjacent organic overlayer, efficient conversion of Wannier excitons into Frenkel excitons via Förster-type resonant energy transfer (FRET) has been demonstrated. The design here in use consists of a ladder-type oligo(p-phenylenes) (LOPPs) derivative, in the specific case a spiro-annulated ladder-type quarter-phenyl (L4P-SP3), deposited on ZnO-based single quantum wells (SQW) to obtain incoherent electronic coupling. The SQWs we use are grown with extremely thin (2 nm) capping layer, in order to keep the two species spatially close to maximize the coupling. With photoluminescence excitation and time-resolved spectroscopy, we demonstrate that these hybrid structures exhibit energy transfer from the inorganic material to the organic molecules with an efficiency up to 77%. However, UPS measurements show a type-II energy level alignment between ZnO and the molecular layer, resulting in a very efficient charge separation process (η_{CT}=0.9) that suppresses the molecular emission.
To overcome this issue, two different strategies are here proposed.

The first idea relies on a fast and highly efficient cascade FRET: following the primary transfer step from the QW, the excitation is conveyed away from the hybrid interface by a secondary transfer-step within the organic layer. As final acceptor we select ladder-type sexiphenyl (L6P). In such a structure, we demonstrate a recovery of the molecular emission by a factor eight, showing that the intermolecular FRET outpaced almost entirely the charge separation process.

As alternative option, we tune the energy levels at the interface by introducing an organometallic donor monolayer [RuCp*mes]. The interlayer reduces substantially the ZnO work function, aligning the frontier levels of the inorganic and organic semiconductor. Optical experiments show the benefits of the interlayer: while the FRET efficiency is unaffected, the L4P-SP3 emission and its photoluminescence lifetime increase by a factor of seven, when compared to the same structure without interlayer.

ZUSAMMENFASSUNG

Energy Transfer in Organic-Inorganic Semiconductor Structures

Hybride anorganisch/organische Strukturen (HIOS) stellen vielversprechende Kandidaten zur Entwicklung neuartiger und verbesserter opto-elektronischer Bauteile dar. In HIOS-Strukturen, die auf einem Quantengraben und einer angrenzenden organischen Deckschicht basieren, wurde eine effiziente Umwandlung von Wannier-Exzitonen in Frenkel-Exzitonen mittels resonantem Förster Energietransfer (FRET) demonstriert.
Das hier verwendete Design besteht aus einem spiro-annulierten Quarterphenyl (L4P-SP3), das auf einen ZnO-Einfach-Quantengraben (SQW) aufgewachsen wurde, um inkohärente Kopplung zu erreichen.
Mittels optischer Spektroskopie haben wir demonstriert, dass diese hybriden Strukturen Energietransfer vom SQW zu den organischen Molekülen mit einer Effizienz von bis zu 77% zeigen. Allerdings zeigen UPS-Messungen eine typ-II-artige Energieniveau-Anpassung zwischen ZnO und der molekularen Schicht, die zu einem sehr effizienten Ladungstrennungsvorgang (η_{CT}=0.9) führt, der die molekulare Emission unterdrückt.
Zur Überwindung dieses Problems werden in dieser Arbeit zwei verschiedene Strategien vorgeschlagen.

Die erste beruht auf einer schnellen und hocheffizienten Energietransfer-Kaskade: nach der ersten Transferstufe wird die Anregungsenergie von der hybriden Grenzfläche weggeleitet, indem eine zweite Energietransferstufe ein-geführt wird, bevor die Dissoziation der Exzitonen an der Grenzfläche statt-finden kann. Wir verwenden ein Oligophenylen (Sexiphenyl, L6P) als endgültigen Akzeptor. In solch einer Struktur können wir eine Wiederherstellung der molekularen Emission um einen Faktor acht demonstrieren und zeigen, dass der Energietransferprozess zwischen L4P-SP3 und L6P den Ladungstrennungsprozess fast vollständig überholt.

Als andere Option haben wir die Energieniveaus angepasst, indem eine organometallische Donor-Monolage [RuCp*mes] ergänzt wird. Diese Zwischenschicht senkt die Austrittsarbeit von ZnO deutlich ab und führt so zu einer Anpassung der Niveaus zwischen dem anorganischen und dem organischen Halbleiter. Optische Messungen zeigen die Vorteile der Zwischenlage: während die Effizienz des Energietransfers unverändert bleibt, steigen die Emission von L4P-SP3 sowie die Lebenszeit der molekularen Photoluminescenz um einen Faktor sieben verglichen mit entsprechenden Strukturen ohne Zwischenlage.

DECLARATION OF AUTHORSHIP

Hiermit erklre ich, die Dissertation selbststndig und nur unter Verwendung der angegebenen Hilfen und Hilfsmittel angefertigt zu haben.

Ich habe mich nicht anderwrts um einen Doktorgrad in dem Promotionsfach beworben und besitze keinen entsprechenden Doktorgrad.

Die Promotionsordnung der Mathematisch-Naturwissenschaftlichen Fakultt, verffentlicht im Amtlichen Mitteilungsblatt der Humboldt-Universitt zu Berlin Nr. 126/2014 am 18.11.2014, habe ich zur Kenntnis genommen.

Ort, Datum Francesco Bianchi

LIST OF PUBLICATIONS

Parts of this work have already been published in:

[1] B. Kobin, F. Bianchi, S. Halm, J. Leistner, S. Blumstengel, F. Henneberger, and S. Hecht. Green Emission in Ladder-Type Quarterphenyl: Beyond the Fluorenone-Defect. Advanced Functional Materials, 24(48):7717-7727, **2014**.[1]

[2] F. Bianchi, S. Sadofev, R. Schlesinger, B. Kobin, S. Hecht, N. Koch, F. Henneberger and S. Blumstengel. Cascade Energy Transfer versus Charge Separation in Ladder-type oligo(p-phenylene)/ZnO Hybrid Structures for Light-Emitting Applications. Applied Physics Letters, (23), **2014**.[2]

[3] R. Schlesinger, F. Bianchi, S. Blumstengel, C. Christodoulou, R. Ovsyannikov, B. Kobin, K. Moudgil, S. Barlow, S. Hecht, S. B. R. Marder, F. Henneberger, and N. Koch. Efficient Light Emission from Inorganic and Organic Semiconductor Hybrid Structures by Energy-Level Tuning. Nature Communication, **2015**.[3]

ACKNOWLEDGEMENT

Questa tesi e' dedicata un po' a tutti...ai presenti, ma soprattutto agli assenti...
La dedica piu' grande va ovviamente ad un uomo in particolare...

un uomo che per 24 anni mi ha detto:
"fai i compiti appena ti vengono dati, non aspettare l'ultimo momento!"

finche' un giorno non l'ho beccato a fare i SUOI compiti a pochi minuti da una SUA lezione...

d'altronde, il sangue non e' acqua...

Sempre farina del mio sacco, e senza pressione da esterni, voglio aggiungere la frase:
"Infiniti ringraziamenti a mia sorella".

Scherzi a parte, un grosso ringraziamento va a mia madre e a mia sorella per avermi concesso la possibilita' di fare il mio dottorato. E' stato soprattutto per i loro sforzi e per i loro sacrifici che che mi sono potuto trasferire a Berlino e vivere questa avventura, dall'inizio sino alla fine.

1

INTRODUCTION

1.1 BEYOND THE LIMITS...

Nowadays, society has an insatiable demand for new opto-electronic functions like biomedical imaging, nanoscale white-light emitters and ultra-fast data processing. These are but a few areas where technology requires increasing capabilities like higher efficiency, high-speed processing and lower energy consumption - compressed into even smaller volumes. However, standard materials have already been pushed close to their intrinsic limits.

Inorganic semiconductors are well established materials for opto-electronic applications. They offer full control during the growth process and can be prepared on high purity levels. Inorganic semiconductors allow for growth of thin layers and single crystals. This enables to reach high charge carriers mobilities and efficient electrical injection. However, optical properties such as quantum yields and absorption cross sections are relatively low. Furthermore, many applications require great flexibility regarding the range of absorption and emission wavelengths, but inorganic semiconductors typically cover only wavelength ranges in the order of few nanometers.

Recently, organic materials have found their way into opto-electronic devices as well. Organic molecules or polymers with unsaturated bonds possess outstanding optical properties defined by their π-electrons. In particular, when π bonds are conjugated, the resulting species stand out by a strong light-matter coupling and, thus, large absorption cross-sections and quantum yields. This class of materials possesses a tremendous structural variability, yielding to large ranges of electronic and optical properties, including high wavelength tunability. However, organics are limited by low charge carrier densities and mobilities, and by the difficulty of carrier injection. A big limitation of optically active organic species is their low temporal stability: subsequently to the absorption of a photon, molecules can decompose, i.e. change their structure and thus lose their optical peculiarities.

From an application perspective, novel opto-electronic functions could be realized by combining these two classes of materials within the same Hybrid Inorganic/Organic System for Opto-Electronics device (HIOS).
High-brightness white-light emitters could be implemented with this approach: bright emissivity within a wide wavelength range, readily available through

conjugated organic molecules, could be combined with the high excitation densities of inorganic semiconductors.[4–6]

Hybrid Structures: a new kind of Light?

In high-quality inorganic semiconductors and in organic materials, optical properties near and below the band gap are dominated by bound electron-hole pairs called excitons.[4,7,8] Thus, a fundamental requirement for a hybrid system is efficient coupling between the excitons of the two materials. Consider a hybrid structure with energy levels as shown in Fig. 1A: a single quantum well (QW) in close contact with a thin layer of molecules.

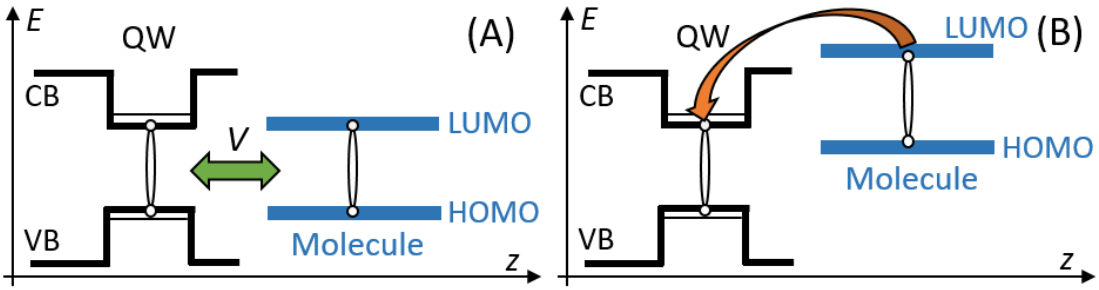

Figure 1: *(A) Coupling of optical excitations: Excitonic states, in the inorganic QW (black line) and in the conjugated organic material (blue line). When the energy levels of the two species (CB and LUMO, VB and HOMO) are resonantly adjusted and in close proximity, the two excitations can be coupled by dipole-dipole-type interactions (V). (B) Energy levels in a realistic hybrid system. Position of the LUMO is usually at higher energy than the CB because of the low electron affinity of organic species.*

When the energy levels of the two species are resonantly adjusted, i.e. the valence band (VB) of the QW matches the highest occupied molecular orbital (HOMO) of the molecule, and the conduction band (CB) of the QW matches the lowest unoccupied molecular orbital (LUMO) of the molecule, the two excitonic states can couple via Coulomb interaction (V). When this happens, the system eigenstates are no longer pure states of the individual species, but rather a coherent superposition. In the coupled state, any excitation in one component oscillates periodically between the two species.[8,9]
In most organic materials this superposition is destroyed by dissipative processes[9] and the excitation is resolved by light emission from the molecules. This transfer process from the QW (donor) to the molecule (acceptor) is actuated by non-radiative resonance energy transfer (ET).[5,6,10]
Such kind of hybrid structures could be the foundation for novel white-light emitting devices, in which the excitation from an inorganic heterostructure is efficiently transferred by ET to an adjacent organic material where the emission takes place subsequently.

The way to a ET-based Hybrid Device

A novel hybrid ET-based device would compete with already commercialised technologies: white organic light emitting diodes (WOLEDs) and inorganic solid state white light emitting diodes (WLEDs).

Commercial WLEDs combine an inorganic LED (GaN or InGaN based) and an external yellow emitting Phosphor Ce^{3+}:YAG (Yttrium Aluminium Garnet doped with Cerium): the inorganic semiconductor emits in the blue/ultra violet (UV) and the phosphor acts as a down-converter with subsequent emission of a broad yellowish band (green+red). However, because of this mixture of emissions, the colour quality for these devices is not yet optimal. Furthermore, the efficiency of the radiative down-conversion is limited (65-67%[11]), as the absorption coefficients and emission yields for phosphors are still relatively low. These types of structures suffer from thermal management issues that limit the durability and because of the long decay times of phosphors (in the order of milliseconds), these devices cannot be modulated at high frequencies.[11]

The simplest design of a WOLED combines an UV/blue light-emitting host material doped with green and red emitting molecules.[12] The internal colour conversion relies on ET and on carrier trapping effects within the mixture. The main deficiency of this technology is the limited temporal stability of the organic blue hosts, which defects the long time colour quality of the devices.[12]

The realization of a hybrid device could easily overcome all the above deficiencies.[5] Fig. 2 shows a possible configuration of a hybrid device of an inorganic semiconductor QW and a layer of conjugated organic molecules in close proximity.

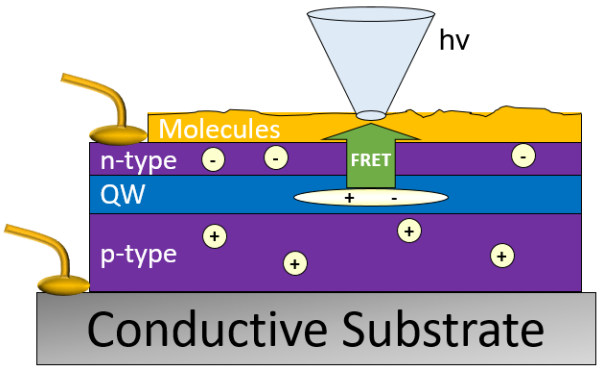

Figure 2: *Possible design for a hybrid light-emitting device. A QW (blue area) lies between two barriers for n and p injections (violet areas). The organic molecules (yellow area) are non-radiatively sensitized by the excitons collected in the well, with subsequent emission of light.*

The inorganic and organic constituents are selected such that an efficient coupling of the excitations and, thus, ET is achieved. The two constituents are integrated in a p-i-n configuration to allow the electrical injection of the QW.

Recombination of carriers takes place in the well layer, and light is emitted from the molecules.
This approach promises higher colour conversion efficiencies with lower power consumption, as the ET is not limited by the molecular absorption coefficients. Better colour rendering can be achieved as the emission of molecules can be finely tuned to match the receptors of the eyes. Further, the device can be downsized to nm-scale, as both QW and organic layer can be few nanometers thick and must be in close contact. Finally, the resulting device is expected to combine the high time stability and high carrier injection of the inorganic blue/UV component with the fast decay times (usually in the nanosecond order) of an organic emitter, so that ultra-fast modulation is also achievable.

However, when an organic molecule is in direct contact with a semiconductor surface, the resulting level alignment is almost never as shown in Fig. 1A, but rather as shown in Fig. 1B. The above considerations about the hybrid pair are still valid, but the different energy level alignment at the hybrid interface hinders the usability of the device.
When the energy level configuration is like in Fig. 1B, excitons in the molecular layer are dissociated because electrons in the LUMO relax back into the semiconductor CB,[13] and light emission is suppressed.
This is key factor for light-emitting applications, as the molecular luminescence pumped via exciton transfer is dissipated by the exciton dissociation process at the interface.

Despite several studies on this kind of systems,[14–19] an electro-luminescence ET-based device has not been realised yet. Such a hybrid device must meet several challenges:

- Structures must be designed for efficient incoherent coupling between the inorganic semiconductor and the organic molecules.
- Donor-Acceptor pair must be chosen to maximize their spectral compatibility for energy transfer.
- The energy transfer must persist at room temperature.
- Alignment of the frontier energy levels must be understood and eventually engineered to prevent dissociation of excitons at the interface.
- The device must be designed for electrical injection of carriers.

This thesis concentrates on the first three points of the above list.
The first step was to develop an optimized hybrid sample for efficient energy transfer which persists up to room temperatures. Later, this work focussed on the alignment of the frontier energy levels at the hybrid interface.
Efficient strategies are proposed to deactivate the dissociation of excitons, paving the way for a hybrid system with high ET efficiencies and bright luminescence yield.

1.2 STATE OF THE ART

The potential of HIOS was first discussed more than 20 years ago. In a series of theoretical works, it was predicted that superior functionalities of such structures would arise thanks to electronic coupling of optical excitations amongst the constituents.[6,20,21]

Non-radiative energy transfer in a hybrid structure with an organic overlayer was first experimentally studied by S. Blumstengel[17] using ZnO as inorganic donor and by Heliotis[14] using InGaN. Starting from these results, efficient conversion of excitons via energy transfer has been demonstrated experimentally for hybrid systems based on ZnCdO/ZnO, InGaN/GaN and GaAs/AlGaAs QWs in conjunction with various conjugated organic molecules, aggregates or polymers.[14,16–19]
The design is in all cases similar: the QW structure is realized with the upper barrier layer sufficiently thin, and subsequently covered by a thin layer of the organic material. In such a setting, excitation energy can be transferred from the QW to the molecules.
Energy transfer in both directions was discussed for multilayer structures composed of alternating monolayers of CdSe quantum dots (QDs) and J-aggregates.[22] In blends of colloidal QDs with polymers, efficient energy transfer from the organic to the inorganic components was observed as well.[23]

For above examples the energy transfer is mediated by long-range Förster dipolar interactions, but there are also some cases of Dexter type exchange transfer, where triplet excitons were transferred from PbBr6 layers in a perovskite structure to naphthalene layers[24] or from pentacene to PbSe nanocrystals.[25]

1.3 MATERIALS

Inorganic Semiconductor: Donor

Most of the interest for new light emitters concerns down-conversion from UV to visible light, thus, inorganic materials selected as a hybrid-donor are usually GaN,[19] InGaN[14,26] or ZnO.[17,18] ZnO is the inorganic semiconductor selected for this thesis. ZnO is a II-VI alloy with a 3.4 eV wide band gap and strong exciton binding energy (60 meV). It is highly available and non-poisonous. In addition, it exhibits strong excitonic resonances with large optical dipole moments, ensuring efficient coupling with the organic excitations.
ZnO can be epitaxially grown with high crystalline perfection at exceedingly low substrate temperatures (100 °C[27,28]). Due to stable bond reconstructions, II-O materials form chemically inert interfaces and are, thus, especially well-suited candidates to pair with organic molecules, as no passivation of the inorganic surface is required for an unperturbed ordered growth of an organic overlayer.[29] Most importantly, ZnO heterostructures fabricated at low temperatures still exhibit sharp optical features with widths in the meV-range (10-20

meV[17,30,31]). Heterostructures like quantum wells allow to confine the excitons close to the molecular overlayer, as these structures can be prepared with a thin or even without capping layer.

Organic Semiconductor: Acceptor

An organic semiconductor must fulfil several requirements to be selected to pair the inorganic donor. These requirements are not exclusively associated with the energy transfer process. In the "standard" intermolecular or intra-molecular energy transfer, the coupling is naturally favoured by the broad molecular spectral features,[8] but, replacing the donor with an inorganic semiconductor imposes a different aptitude. Heterostructures are usually characterized by spectrally sharp features, so a possible molecular acceptor should display similar sharp vibronic transitions.
Upon the spectral overlap described above, the organic emitter must show the following properties:

- High luminescence quantum yield (QY), as the efficiency of a hybrid LED depends on the emitter emissivity.
- Small Stokes-shift, to assure a relatively high exciton diffusion length mediated by intermolecular ET.
- Durability. When applied in a device structure, the organic component should be as durable as possible. This relates to thermal, photochemical and electrochemical degradation processes.
- Stability to gas phase processing, as the sample fabrication is favoured to UHV based techniques.
- Thin films formation. As the device design consist of 2D structures, it is important that the components can be grown in closed homogeneous films. These may either be of high crystalline quality or totally amorphous. Films must also be stable over time.

Good candidates that fulfil all the above requirements are the so-called ladder polymers,[8,32–35] the unit cell of which is shown in Fig. 3 for one particular derivative of PPP (poly-/para-phenylene).

The presence of the two links between the phenyl rings prevents the relative rotation of neighbouring rings and ensures that the π-electron system is kept in one plane. The high intra-chain order, small Stokes shift ($\approx$ 0.06 eV), high quantum yield, and good film-forming properties make these molecules ideal materials for opto-electronic devices. The origin of the observed optical properties can clearly be linked to their rigid structure maximizing the π-conjugation. Such kind of polyfluorenes emerged as a very attractive class of conjugated polymers, especially for display applications, owing to their

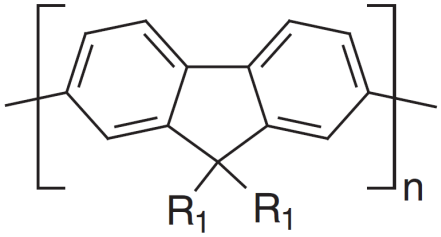

Figure 3: *Chemical structure of poly-(p-phenylene)*

efficient blue electro-luminescence coupled with relatively high charge-carrier mobility and good processability.

This work selects a class of molecules directly correlated with the PPP, in the specific ladder-type oligo(p-phenylene)s or LOPPs.[36] The newly synthesized LOPPs exhibit outstanding photophysical properties traceable to the PPP: sharp and intense optical transitions characterized by narrow absorption bands and very small Stokes shifts. LOPPs are also characterized by large extinction coefficients and high fluorescence quantum yields. Initial investigations demonstrate that these materials are applicable to gas deposition techniques allowing the controlled generation of organic (ultra)thin films on solid substrate surfaces.

The principal topic of this thesis is the realization of a hybrid light-emitting application based on ET combining an inorganic semiconductor as donor and an organic molecule as acceptor. Chapter 2 provides the general theoretical framework for the following investigations. Chapter 3 collects all experimental aspects: the samples design, the preparation techniques and the experimental setups.

Following chapters treat optical properties of LOPPs/ZnO hybrid structures. Chapter 4 introduces energy transfer between a ZnO heterostructure and a ladder-type quaterphenyl (L4P)/polymer spincasted layer. In addition to the ET experiments, this chapter condenses photo-degradation studies of the sole L4P in solution and solid state. After, the chemical modifications of L4P necessary to improve its photo-stability and, most important, its structural properties, are discussed. Spiro-substituted LOPPs (Section 4.8) are thus introduced.
Chapter 5 presents a systematic investigation of energy transfer between ZnO and a thin overlayer of the triply spiro annulated-L4P, namely L4P-SP3. The non-radiative transfer mechanism is investigated also for varying temperatures. Beyond demonstration of excitonic transfer, an inherent obstacle was observed: an unfavourable energy level offset between the two components causes an efficient charge transfer that completely quenches the molecular emission.
Chapter 6 and 7 give two solutions to the above obstacle.
In chapter 6, the molecular excitons are funnelled away from the detrimental interface by an intermolecular energy transfer. After introduction of a molecular companion for L4P-SP3, optical experiments show that the double, or cascade energy transfer, is a way to recover the otherwise quenched luminescence.
Chapter 7 focusses directly on the level alignment. Using an organometallic donor monolayer, the ZnO work function is substantially lowered, tuning the frontier levels of the two semiconductors. This approach also recovers the radiative emission yield of the molecules.
Finally, chapter 8 concludes this thesis and gives an outlook (Section 8.1) for future developments and experiments.

2

FOUNDATIONS

Energy transfer from inorganic to organic materials is the baseline for the targeted hybrid light emitting devices. This transfer founds on a resonant coupling of the different types of excitons which exist in the inorganic and the organic components.
In the following pages, these two types of excitons are introduced, and models for the energy transfer between them are discussed. Energy transfer requires a resonant coupling of the excitons, thus, the respective energy levels of the hybrid interface have to be aligned. Finally, questions of the energy level alignment is considered, as it is a key element for a functional HIOS device.

2.1 EXCITONS

An exciton is the fundamental electronic excitation in a dielectric medium. When a semiconductor with direct energy-gap (E_g) absorbs a photon with energy close to the band-edge $h\nu \approx E_g$, an electron gets promoted from the valence band (VB) into the conduction band (CB) leaving a positively charged hole behind. The two charges are attracted to each other by Coulomb forces, and the resulting neutral particle is called exciton.
Generally, excitons are described using two limiting cases: Frenkel[37] (F) and Wannier-Mott excitons[38] (WM). The distinction lies in the spatial separation, in the binding energies and in the different masses that the electron-hole pairs exhibit.[39]

Optical properties of pure semiconductor crystals are dominated by exciton absorption lines typically arranged in a hydrogenic series well described as Wannier-Mott, or weak binding, excitons. WM excitons have a large Bohr radii ($a_B \approx 100$ Å in III-V materials and $a_B \approx 30$ Å in II-VI ones[40,41]); in both cases, $a_B >> a$ (with a the lattice constant) as the two charges are spatially separated through the crystal lattice.[40,42]
Apart from a small reduced mass ($m_e^* \approx 0.1 m_e$[10,43]), the electron-hole attraction is screened by the large dielectric constant ($\epsilon = 5.24$ for ZnO,[40] 9.7 for GaN[42]). The exciton binding energy E_b, the difference between the 1S exciton line and the electronic band structure gap, is only a tiny fraction of the Rydberg, not more than a few tens of meV.[10]

Frenkel excitons are usually found in molecular crystals.[8,44] They represent the limiting case in which the exciton essentially is a molecular (or atomic) excitation, with an electron in the LUMO and a hole in the HOMO. The two charges are separated by a typical distance of 1 nm in a medium with a large dielectric constant ($\epsilon = 4$); the resulting binding energy of the pair is approx. 0.5 eV. Driven by electrostatic interaction, F excitons can propagate as a whole in the crystal. Interaction between transition dipole moments gives rise to a long-range excitation transfer and thus a formation of exciton bands.
Systems in which the charge overlap between neighbouring molecules or atoms is small, typically carry F excitons. Examples are Van der Waals (VdW) solids (molecular crystals and aggregates[8]), but also alkali-halide crystals.
The differences in the internal electronic structure of the excitons manifest themselves in the linear optical response of the two materials: the oscillator strength f_x scales with the inverse of the volume V_x occupied by the wave function of the electron-hole relative motion $f_x \approx (V/V_x)f$ with V being the volume of the unit cell and f the oscillator strength of the molecular or atomic transition. In the case of F excitons, V_F=V and thus $f_F \approx f$. In an inorganic semiconductor nanostructure counterpart, instead, if the dimensionality D and the confinement length l_C, the characteristic volume of the WM excitons is $V_{WM} \approx a_B^D l_C^{3-D}$. Since $V_{WM} >> V$, the oscillator strength f_{WM} of the inorganic specie is much smaller than for the organic counterpart.

Frenkel and Wannier-Mott excitons refer to two limiting cases with regards to the length scale of relative electron-hole interaction. Between these extremes lies the the intermediate case that is the charge-transfer exciton (CTE). CTE have an electron-hole separation of one molecule, where the hole is located at one molecule and the electron on the neighbouring one.[10] This is usually referred to as a "donor-acceptor" (D-A) complex.[8,45]

2.2 INORGANIC SEMICONDUCTORS

Electronic states of inorganic semiconductor crystals are usually well described by a band structure. These energy bands are calculated assuming an appropriate crystal potential V in a rigid lattice and using the one-electron approximation.[43,46] Electron-electron interactions are included only on average without considering correlation effects.
The single particle Hamiltonian is usually defined as:

$$\hat{\mathbf{H}} = \frac{p^2}{2m_0} + V(\mathbf{r}) \tag{1}$$

where m_0 is the free electron mass, p the momentum operator, and $V(r)$ the mean field potential including the full translational symmetry of the crystal. The single particle eigenstates have energies E_{nk} and present Bloch states which

are characterized by a wave-vector (k) within the first Brillouin zone and by a band index (n)

$$\psi_{nk}(\mathbf{r}) = \frac{1}{\sqrt{N}} e^{i\mathbf{k}*\mathbf{r}} \mu_{nk}(\mathbf{r}) \tag{2}$$

$\mu_{nk}(\mathbf{r})$ is periodic on the unit cell of volume Ω and the total volume of the crystal is $V{=}N\Omega$.[43] The highest occupied valence band and the lowest empty conduction band each have large bandwidths and small effective masses, corresponding to strongly delocalized electronic states.

BAND-GAP ENGINEERING AND QUANTUM CONFINEMENT

Band gap engineering is a crucial step for development of optoelectronic devices.[47] By alloying the starting semiconductor with another material of different energy gap, the electronic properties of the resultant alloy can be fine tuned, thus affecting electronic and optical properties of the confined semiconductor systems.
The basic example of an artificial low-dimensional structure is an epitaxially grown quantum well (QW) in which a central semiconductor layer (the well) is sandwiched between semiconductors having a larger band gap (the barriers). Doing this, the bottom profile of the conduction band along the growth direction confines the electrons within the well layer, and similarly for the holes in the valence band (i.e., a type I quantum well).[41,47]
If the coherence length of the electrons (and holes) is larger than the well thickness L_w, quantum confinement is realized.[41,47] In such regime, charges motion along the growth axis is discretized, while the one along the well plane remains free. For this case, the envelope function approach is well suited to describe WM excitons for quantum confined structures.[43] Assuming infinite barriers, the confinement energies are:

$$E_{c,m\mathbf{k}_\parallel} = \frac{\hbar^2 k_\parallel^2}{2m_e} \frac{\hbar^2}{2m_e} \left(\frac{\pi m}{L_w}\right)^2 \tag{3}$$

with envelope functions:

$$F_{c,m}(z) = \sqrt{\frac{2}{L_w}} sin\left(\frac{\pi m z}{L_w}\right) \tag{4}$$

For $m_{e\parallel} \approx 0.1 * m_0$ and $L_w \approx 3.5$ nm, the range of confinement energies is $E_{m=1,k_\parallel=0}$ in the range of few tens of meV. The states are thus organized into two-dimensional subbands.[39,41] Each subband comprises an ensemble of electronic states with the same state of quantized motion perpendicular to the interfaces, and continuously varying wave-vectors K to their unhindered in-plane motion. The population of electrons which occupying such a subband structure is referred to as two dimensional electron gas.

Inter-subband transitions lead to staircase like absorption spectra, with each step corresponding to a transition threshold of a electron-subband and hole-subband pair. The same consideration is valid also for excitons in the Well, not supposing excitation as the raising an electron from the valence to the conduction band, but rather to consider the creation of an electron-hole pair. This problem, supposing the attraction to be not too strong, is essentially the same problem as the states of the hydrogen atom, corrected for the different effective masses and dielectric constants in the semiconductor.
Energetic levels, including the in plane center-of-mass translational energy, are given by:

$$E_{n\mathbf{Q}\parallel} = E_{2D,g} + \frac{\hbar^2 Q_\parallel^2}{2M} - E_b \tag{5}$$

the binding energy E_b for the lowest exciton in the strictly two-dimensional limit is R^*_{2D}=$4R^*$. In the most relevant case of a quantum-well with thickness L_w comparable to the Bohr radius, the motion of the electron and of the hole along the growth direction are separately quantized and the binding energy and oscillator strength of the QW exciton are significantly increased compared to the bulk.
The electron-hole interaction leads to an enhancement of the absorption probability even for unbound electron-hole pairs at energies $\hbar\omega \geq E_{g,2D}$, by an amount given by the two-dimensional Sommerfeld factor[10,43] Fig. 4.
The two consequences of this are: (1) the electron and hole are even closer together than in the three-dimensional case, so the absorption strength to create such an exciton is even larger; (2) the exciton has a larger binding energy because the electron and hole are closer together, and hence it orbits "faster".[48]
The lowest bound state n=1 has the envelope function for the 1S state as:

$$F^{2D}_{1S}(\mathbf{r}) = \frac{2\sqrt{2}}{a_0\sqrt{\pi}} e^{-2r/a_0} \tag{6}$$

where the two-dimensional exciton radius is a_{2D}=$a_{Bulk}/2$. Although the binding energy never reaches $4R^*$, it usually can increases up to a maximum of 2 to 3 times R depending on the material parameters.[39,41,46]
As a result of the faster orbiting, the exciton is able to complete a classical orbit before being destroyed by the optical phonon, and hence it remains a well-defined resonance.[48] Equivalently, although the line-width of the quantum well exciton is comparable to that of the bulk exciton, the binding energy is larger, and the peak is still well resolved from the onset of the "interband" absorption at the band-gap energy. These two reasons explain why quantum well excitons are relatively stronger and also better resolved than bulk excitons. The practical advantage is that excitonic peaks for QW can be seen and used also at room temperature.

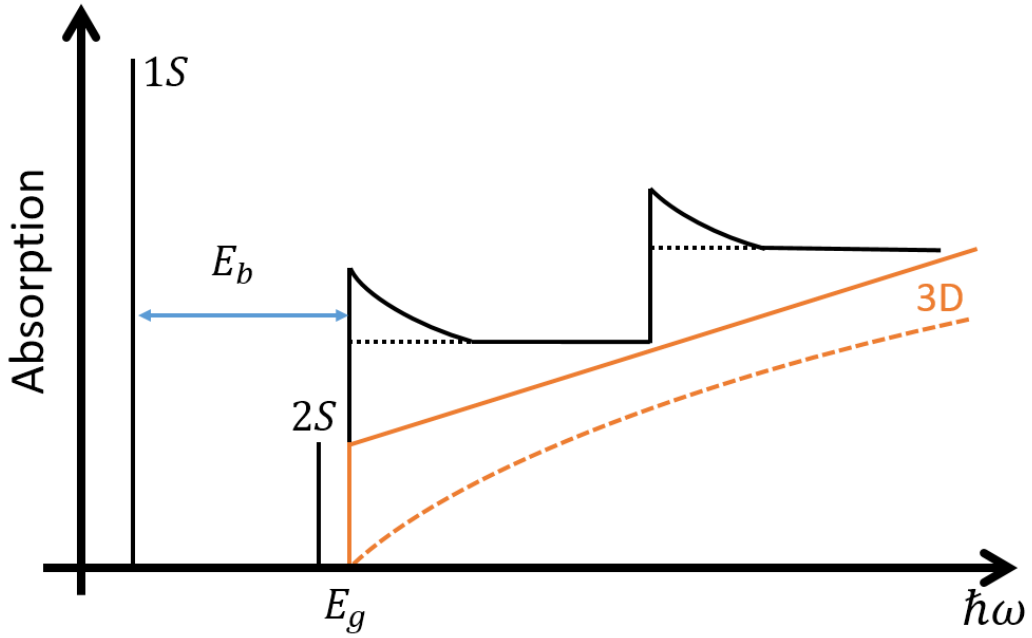

Figure 4: *Absorption spectrum for inorganic semiconductor: raw absorption spectrum for a 3D bulk semiconductor with and without excitons (orange line solid and dashed respectively). Absorption spectrum for a 2-dimensional systems with and without excitons (black line). In comparison to the case involving only free electron-hole pairs (dashed lines), excitons cause the emergence of discrete absorption lines below the effective quantum well band-gap, and each step resulting from continuum absorption is deformed by a range of Coulomb enhanced interband absorption (solid line). All curves are normalized on the same energy gap E_g.*

ZnO and ZnO/ZnMgO QW structures

Wurtzitic ZnO belongs to the group of II-VI compound semiconductor with a wide band gap (E_g= 3.437 eV at 2K[49]). The main advantage of ZnO as a light emitter is its large exciton binding energy (E_b=60 meV). The latter, is three times larger than the 20 meV of GaN,[49,50] which permits excitonic recombination and lasing up to room temperature.
In the case of ZnO, alloying with MgO is an effective means to increase the energy band-gap.[39,41,51] For the present work, the ZnO/ZnMgO heterosystem is of particular interest as it allows to realize QW structures with type-I band alignment.[30,49]
The ZnMgO alloy system enables band-gap engineering from E_g=3.37 eV (ZnO) to around 4 eV ($Zn_{0.67}Mg_{0.33O}$) at room temperature.[7] Photo-luminescence (PL) studies of ZnO quantum wells within ZnMgO and super-lattices have shown a possible tuning of the emission wavelengths from 3.36 to approx. 3.87 eV.
ZnO surfaces are chemically inert due to robust surface reconstruction.[48,49] In the HIOS contest, conjugated organic molecules can be adsorbed electronically intact onto such surfaces.
The excitonic properties of ZnO are determined by its band structure. The lowest CB is formed from the empty 4S states of Zn^{2+}. The VB, originating from the occupied 2p orbitals of O_2, is split under the influence of the hexagonal crystal field into two states. Inclusion of spin gives a further splitting into three twofold-degenerate sub-VBs.[40,51,52]
Moreover, the excitons in ZnO-based QW exhibit a strong stability compared to excitons in bulk semiconductors or in III-V QWs due to the enhancement of the binding energy and the reduction of the exciton-phonon coupling caused by quantum confinement. Exciton confinement in ZnO/ZnMgO heterostructures can be tuned independently by varying the well composition (x) or the well thickness (L_w).[7,46,48,53]

Excitonic recombination follows the same selection rules as the absorption. In addition, only the nS excitons can radiatively recombine. This means that the excitonic luminescence emitted below the E_m-HH_n band edge should consist of monochromatic lines. The emission consists most likely of a single line caused by the $1S$ excitons attached to the E_1-HH_1 band-gap.[43,46,52,54] Fig. 5 reports LT and RT spectra for the same ZnO/ZnMgO QW sample with 10% Mg contents in the barriers. Spectra are normalized to the peak maximum.

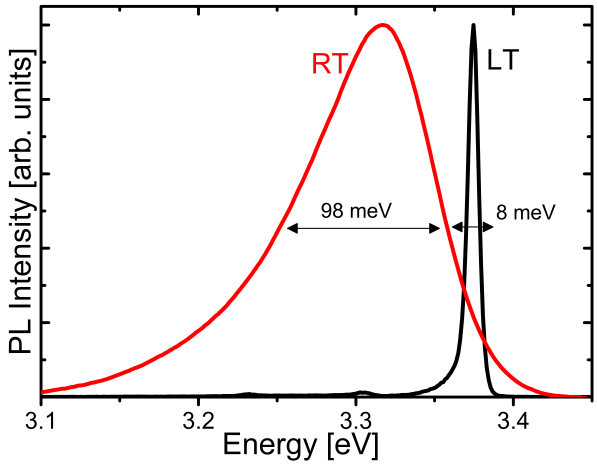

Figure 5: *PL spectra of ZnO/ZnMgO QW structures measured at liquid helium and room temperature excited with a Ti:Sapphire laser at* 3.46 *eV. The FWHM of the QW structure is of* 8 *meV at LT and* 98 *meV at RT. The sample was grown with a Mg content of* 10% *and a* L_w=3.5 *nm.*

For thick (20 nm) ZnMgO barrier, the low-temperature width of the QW emission (black curve) is 8 meV. The line shape of the LT spectrum exhibits a marked low-energy tail revealing exciton localization. A distinct QW emission is also visible at room temperature (red curve). The yield is more than one order of magnitude larger than for ZnO epilayers under comparable excitation conditions.[18,30]

The QW emission at low temperature, is due to localized excitons. Localization is favoured by the small exciton Bohr radius (approx. 1.8 nm) for ZnO (cit) leading to a less effective averaging over potential fluctuation caused by variation of the well width and depth, with the latter induced by alloy disorder in the ternary barriers. The QW luminescence line-width thus depends strongly on the QW thickness and on the Mg concentration. Previous studies showed a luminescence with FWHM of 7 meV[30] for samples with relatively low Mg concentration (min 0.1) and moderate QW thicknesses (d_{QW}=4-5 nm).

2.3 ORGANIC SEMICONDUCTORS

In recent decades the investigation of physical properties of organic solids has attained greatly increased importance and attention. By organic, one customarily means molecules or their ions with carbon atoms as their essential structural elements. Organic solids are single crystals, poly-crystals, or glasses build with organic molecules as building blocks.
The wide variety of these compounds and the possibility to modify them in a practically unlimited fashion using synthetic chemistry have aroused high expectations for the development of new materials and their applications. Current interest focuses in particular on solids composed of those organic molecules which contain conjugated systems of π electrons.[8,10,44,55]

CARBON CONFIGURATION AND π-ELECTRONS

The electron configuration of the free carbon atom in its ground state is $1s^2 2s^2 2p^2$. Carbon has the valence four and the electron configurations in chemically-bonded carbon are derived from the configuration $1s^2 2s 2p^3$. The peculiarity of carbon is its ability to hybridize its orbitals. Depending on how the orbital are mixed, two neighbouring atoms (carbon for simplicity) can be bond by a single, double or triple bonds.[8,56]
A so called double bond can form thank to the sp^2 hybridisation: three degenerate orbitals are constructed out of one s and two p orbitals. They are coplanar and oriented at 120 ° angles of degree. Chemical bonds formed by these orbitals are called σ bonds and are localised between the two C atoms. The fourth P_z orbital remains unchanged as it is directed perpendicular to the sp^2 orbitals plane (Fig. 6).

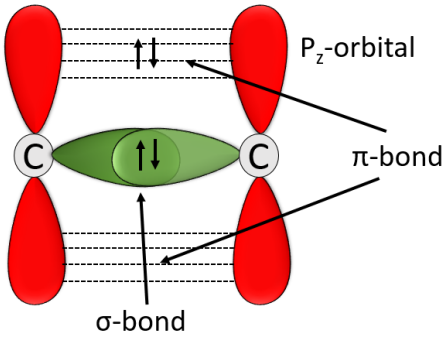

Figure 6: *Brief scheme of a σ bond and overlap between the two P_z orbitals to form a π bond between two carbon atoms.*

The P_z orbitals of neighbouring atoms overlap, enabling an additional bond, called π bond. This yields to a delocalized density of electrons above and below the $SP2$ plane which pass through the atoms. π bounds are weaker than σ bonds, thus, they possess electronic excitation energies in the range of

only a few eV.[8,10,56]
The degree to which the π-electron system of one molecule interacts with those of its neighbours lies at the crux of understanding collective properties in the organic molecules.

FREE ELECTRONS ON A CIRCULAR POTENTIAL WELL

Organic molecules considered in this publication are referred as conjugated aromatic hydrocarbons. The term conjugated refers to the alternating sequence of single and double bonds in the molecule and because of the high mobility of π electrons, they are considered to be shared or delocalized between the carbon atoms.[8,44]
The general chemical formula for such kind of molecules is:

$$C_{4n+2}H_{2n+4} \tag{7}$$

where n is the number of rings in the molecule. These molecules are generally flat (in the ground electronic state at least), and there are $(4\pi + 2)$ π-electrons per molecule, one from each carbon atom.

Because of the π-electrons peculiarities, optical properties of catacondensed poly cyclic aromatic hydrocarbon (PAH, like benzene,[56] or larger systems like antracene or tetracene) can be treated within some approximations with the perimeter free electron orbital theory (PFEO).[57] There, PAHs are considered analogously to a circular ring of atoms around which electrons can move freely (benzene is shown in Fig. 7).

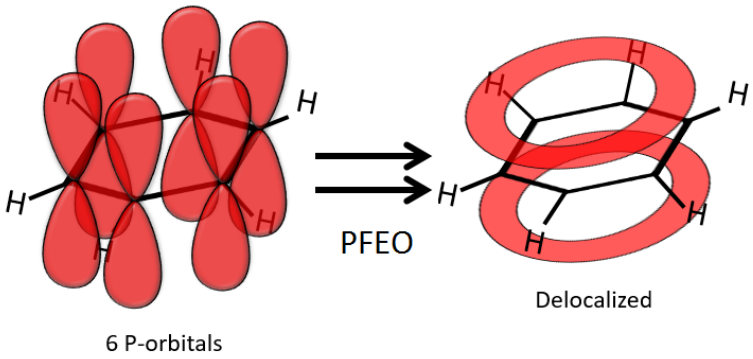

Figure 7: *Benzene π orbitals delocalized within the six carbon atoms. According to the PFEO, energy level can be calculated supposing electrons travelling freely along the ring.*

Potential V is supposed to be V=0 at the circumference of the circle (radius r) and V=∞ anywhere else, the energy eigenvalues can be obtained as:[8]

$$E_q = \frac{h^2}{8\pi^2 m r^2} q^2 = \frac{1.21 * 10^6}{l^2} q^2 \tag{8}$$

where m is, the electron mass: q is an orbital angular momentum quantum number and takes subsequent values $(0, 1, 2, ..)$, l is perimeter of the molecule

defined as l=2πr.
Unlike inorganic semiconductors, excitation energies of molecules (and polymers) can thus be shifted by changing the conjugated system length: going to higher(lower) energies after decreasing(increasing) the π-cloud delocalization. For example, the π-cloud can be enriched or depleted by specific substituting groups and the conjugation length can be maximized or limited by imposing specifics geometries.

OPTICAL PROPERTIES OF ORGANIC MOLECULES

In studying the electronic properties of the conjugated molecules, it is sufficient to focus on the properties of the π-electrons. They are in the highest-energy occupied orbitals and are therefore the most easily excited. Since the lowest-energy vacant orbitals are also π-orbitals, the electronic transitions from the filled to the unfilled levels are referred to as π-π^* transitions.
Optical properties of molecules can be predicted using simplified wave-functions. A major simplification is realized by assuming that the change nuclei distance is almost negligible over the time period required to effect an electronic transition. This is the basis of the so-called Born-Oppenheimer approximation.[8,55–57]

An isolated molecule in its ground state has two spin-paired electrons residing in its HOMO. The promotion of an electron into the LUMO leaves a hole in the HOMO, resulting in a F exciton.[8,10,56]
Scheme in Fig. 8 shows the Franck-Condon principle describing the intensity distribution of the vibronic states typical for organic molecules.

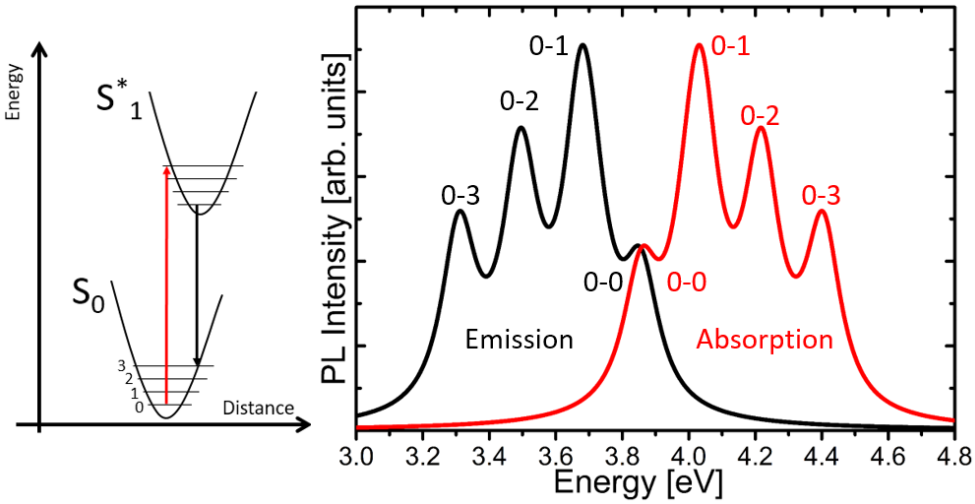

Figure 8: *Left: Diagram of the Franck-Condon principle of the vibronic transitions in molecules. Right: Schematic representation of a molecular absorption and emission spectrum with re-absorption at the* (0-0) *transition.*

The absorption (red arrow) and emission (black arrow) are illustrated by the

Jablonski energy level diagram. The ground, and first electronic states are depicted by S_0, S_l, respectively (Fig. 8), the figure reports a ground state with a harmonic potential, the excited state has a similar potential slightly with a shifted nuclei coordinate. At each of these electronic energy levels the fluorophores can exist in a number of vibrational energy levels, depicted by 0,1,2. If the molecule is excited by an optical pulse, an electron from the lowest vibrational level in the HOMO gets to an excited state depending on the absorbed energy. Since this electronic change is fast, the heavier nuclei will stay constant in their distance, hence the transition is drawn as a vertical line.[8,56] The electron relaxes non-radiatively to the lowest level of the LUMO and successively unwind to one of the vibrational levels of the ground state without a change in the nuclei coordinate. The transition probability depends on the ground and excited state wave-functions overlap.
Generally, the fluorescence spectra appear to be a mirror-image of the absorption spectra, particular in the case of the $S_0 \rightarrow S_l$ transition.[8,58] The symmetric nature of these spectra is a result of the same transitions being involved in both absorption and emission, and the similarities among the vibrational energy levels of S_0 and S_l.

4P AND L4P: EFFECTS OF BRIDGING GROUPS

Comparison between p-quaterphenyl (4P)[8,36] and ladder-type-quarterphenyl (L4P)[2,36] can give a good insight about π-electrons effects on the molecular optical properties. The two molecules share in fact the same π-core made of four phenyl groups, but display different optical properties. 4P is a commercial laser dye, room temperatures absorption and emission spectra measured in solution are shown in Fig. 9A.

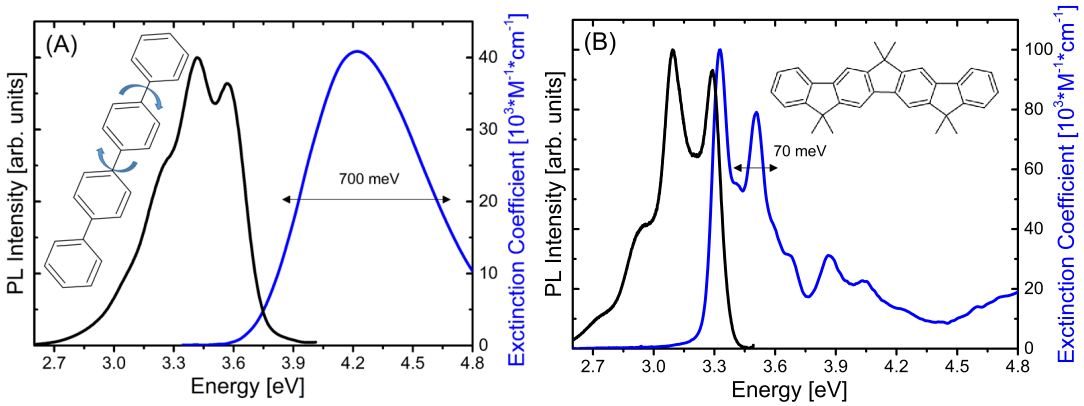

Figure 9: *4P/L4P comparison: absorption and emission spectra for 4P (A) and L4P (B) solution (Tetrahydrofuran, THF). All spectra are performed at room temperature and with an excitation of E_{exc}=4 eV. Chemical structures are also present within the graphs.*

Because of the rotational and torsional degrees of freedom between the phenylene ring, the π-delocalization is limited. 4P displays broad absorption and emission spectra ($\propto$ 700 meV). Since the oscillator strength is distributed on many energies, the resulting extinction coefficient is relatively low.
The absorption spectrum of 4P is devoid of structure, but some vibrational progression is visible in its emission. Such deviation from the mirror image rule usually indicate a different geometric arrangement of nuclei in the excited state as compared to the ground state.[8] The introduction of a rigid back-bone utterly changes the properties of the molecule (Fig. 9B). When the phenyl rings are fixed along the common plane, the oscillator strength is confined in sharp (50 meV) and intense vibronic lines both for emission and absorption.

2.4 ENERGY TRANSFER

Energy transfer is a mechanism of energy migration between two light-sensitive species.[9,59] These species are commonly defined donor and acceptor depending on the directionality of the transfer. Based on the geometry taken into consideration, several models have been developed to describe the transfer for such systems.[9]
When discussing the interaction of (spatially extended) excitations in hybrid structures, it is useful to recall first how the electric interaction between two closely spaced species (donor and acceptor) takes place.
In the model of non-radiative Förster resonant energy transfer[60] (FRET), the two molecules are approximated as dipoles with lengths much shorter than any interaction distance, i.e. point dipoles. Oscillations of the electric dipole polarization $\mathbf{P}_d$ in the excited donor molecule create an electric field:

$$E = \frac{\mathbf{P}_d - 3(\mathbf{P}_d \cdot \mathbf{s})\mathbf{s}}{\epsilon R^3} \tag{9}$$

at the position of the acceptor in R, with the unit vector in the donor-acceptor direction $\mathbf{s} = \mathbf{R}/R$ and ϵ the dielectric constant of the medium.
The electrostatic field in Eq. 9 causes the resulting nonradiative interaction with the acceptor polarization $\mathbf{P}_a$ described by the Hamiltonian:

$$\hat{H}_{int} = -E \cdot \mathbf{P}_a \tag{10}$$

The interaction of excitations in hybrid nanostructures possesses some analogies with the formalism just described: for both excitation species, the relevant spatial sizes are small in comparison with the light wavelength, and hence, one can neglect the retardation effects in the electric field calculation.[4,21] A substantial difference, however, is that for the spatially extended WM excitons, the approximation above (Eq. 9) is not always valid.

FÖRSTER RESONANT ENERGY TRANSFER

The famous work of Förster[60] provides a quantitative description of coupling between transition point-dipole moments of two molecular species at a distance r. Using the composite wave-function ψ_{tot} for the donor (D) and acceptor (A) states:

$$\psi_{tot}(t) = C_1(t)\psi_A^*(t)\psi_D(t) + C_2(t)\psi_A(t)\psi_D^*(t) \tag{11}$$

where ψ_A and ψ_D are the two species wave-functions and the symbol * stands for the excited state. $|C_1(t)|^2$ and $|C_2(t)|^2$ describe the probabilities of finding the excitation on one of the two species respectively.[8,61] The electronic energy oscillates coherently between the donor and the acceptor at frequency $|J|/\hbar$, where J is the strength of the interaction between the pair.[8] With a $J \propto R^{-3}$.

Applying Fermi's golden rule,[10,43] the dependence of the transfer rate is calculated as:[8]

$$\frac{1}{\tau_E T} = \frac{1}{\tau_D}(\frac{R_0}{r})^6 \tag{12}$$

where τ_{ET} and τ_D are the transfer rate and the donor rate respectively, and R_0 is the Förster radius.
The transfer time $T_{D\to A}$ is defined as the inverse of the transfer rate $K_{D\to A}$ and is:

$$\frac{1}{T_{D\to A}} = K_{D\to A} = \frac{4|J|}{\hbar} \propto \frac{1}{R^3} \tag{13}$$

for most systems, however, the energy received is quickly disperses between degenerate vibrational states, each of which can relax to level with lower energy. Such dissipation automatically introduce an irreversibility into the process.
Förster's energy transfer rate k_{ET}^F is defined as:[8,61]

$$k_{ET}^F = \frac{k^2 9c^4}{8\pi\tau_D n_0^4 R^6}\left(\int \frac{F_D(\omega)\sigma_A(\omega)}{\omega^4} d\omega\right) \tag{14}$$

with $F_D(\omega)$ the normalized fluorescence emission spectrum of the donor, $\sigma_A(\omega)$ the acceptor absorption cross section, n_0 the index of refraction of the solvent, c the speed of light and k^2 the orientation factor, usually approximated to 2/3.[8,61] τ_D is the effective donor decay time in absence of any acceptors.[8] The integration in Eq. 14 is performed over frequencies ω.

DISTANCE DEPENDENCE FACTOR

According to Försters theory, the dipoles coupling crucially depends on the distance R between the species and it scales with $1/R^{-P}$. For two point dipoles P=6. The R^{-6} factor has been derived by different authors[8,59,61] and takes into account that the energy transfer is the product of the inducing field and of the induced dipole, which are both varying with R^{-3}. For a point dipole which couples to a plane of acceptors, the exponent reduces to P=4,[62] and for two planes coupling to each other, the exponent reduces further to P=2.[63]

Although the application of this formalism to QW excitons is slightly incomplete, it has been reported that for a configuration similar to the one considered here, experimental data were fitted with a P=2 distance dependence, similar to the plane-to-plane coupling in the Förster theory.[64,65] Distance dependent measurements were also performed for polymer-InGaN/GaN hybrids yielding a $k_{ET} \approx R^{-2}$ dependence, which corresponds to the interaction of two dipole sheets.[14,15]
Regarding the system under study in this thesis, ZnO excitons in quantum

wells are localised justifying the simple model as a first approximation.[18] Previous experiments[17] with ZnO/Molecules pair used a rate $k_{ET} \approx R^{-4}$ for fitting the dipole-dipole coupling of an oscillating dipole with a layer of accepting dipoles placed at a distance d. Such an approximation was valid considering the localisation length of the QW exciton smaller than R.

EXCITATION ENERGY TRANSFER AS JOULE LOSSES

In a comprehensive work by Basko and Agranovich[4–6,20,21,66] energy transfer is modelled for hybrid systems. These authors supposed that the electric field $\xi(\omega)$ created by oscillations of the QW polarization penetrates into an organic component of the hybrid structure. There, the field energy is dissipates by exciting the organic species, given that the transitional frequency ω of $\xi(\omega)$ is close to a molecular resonance in the organic. The transfer rate is then modelled as Joule losses of the electromagnetic field in the acceptor material. The geometry of the problem considers a symmetric structure, consisting of a semiconductor QW of thickness L_w between two barriers of thicknesses L_b each, the whole semiconductor structure is surrounded by thick slabs of an organic material (actually, assuming each slab to be semi-infinite) as shown in Fig. 10.

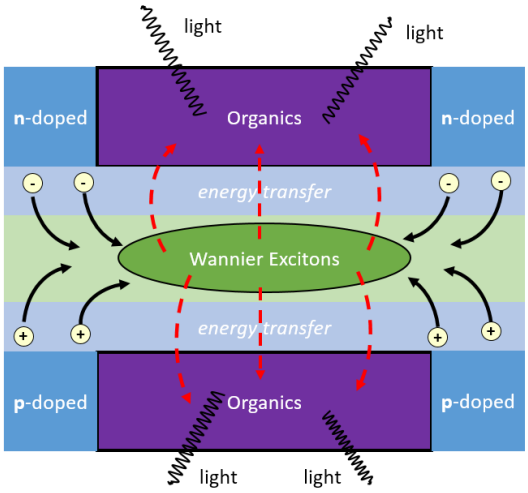

Figure 10: *Sketch of the planar structure that could be used for an energy-transfer-based LED.*

In the frequency region here considered the semiconductor background dielectric constant ϵ_b is real as the same value for both well and barrier. The acceptor overlayer is defined as some medium with its frequency-dependent (ω) complex dielectric tensor $\tilde{\epsilon}$:

$$\tilde{\epsilon}(\omega) = \epsilon'_{ij}(\omega) + i\epsilon'_{ij}(\omega) \tag{15}$$

the interaction Hamiltonian $\hat{\mathbf{H}}_{int}$ is similar to Eq. 10 and is:

$$\hat{\mathbf{H}}_{int} = -\int d^3\mathbf{R} \left(\hat{\mathbf{P}}^{org}(\mathbf{R}) \cdot \hat{\xi}(\mathbf{R}) \right) \tag{16}$$

$\hat{\xi}(\mathbf{R})$ is the electric field operator, produced by the QW polarization $\hat{\mathbf{P}}^{QW}(\mathbf{R})$. The transition rate $1/\tau_{i,f}$ is obtained by Fermi Golden's[8,56] rule as:

$$\frac{1}{\tau_{i,f}} = 2\pi\rho| < f|\hat{\mathbf{H}}_{int}|i > |^2 \tag{17}$$

the quantum mechanical problem is thus equivalent to the classical system reported before (Eq. 9).

FREE EXCITONS

Supposing that the inorganic donor excitation is composed by 2D WM free excitons, the QW polarization **P(r)** can be defined as:[21]

$$\mathbf{P}(\mathbf{r}) = \mathbf{d}^{vc} \sqrt{\frac{2}{\pi a_B^2}} \frac{2}{L_w} \cos^2\left(\frac{\pi z}{L_w}\right) \frac{e^{i\mathbf{K}r_{||}}}{\sqrt{S}} \tag{18}$$

where S is the in-plane normalization area, $\mathbf{K}$ is the in-plane wave vector of the center-of-mass motion, $r_{||} = (x, y)$ the in-plane component of r and a_B is the 2D 1S-exciton Bohr radius confined into a QW of width L_w.
The direction of the in-plane component of the exciton dipole moment $\mathbf{d}^{vc}$ is chosen to be along x, preferring to consider the polarization not with respect to the wave vector, but to some fixed frame. Defined $\mathbf{P}(r)$, it is possible to calculate the corresponding charge density $\rho(R)$ and the static electric field $\xi(R)$ can be obtained by solving the Poisson equation at the hybrid interfaces[21] using:

$$\varphi(z) = \rho_0 C_K e^{-K(z - L_B - L_w/2)} \tag{19}$$

the values of coefficient C_K depend on the orientation considered (in the QW plane or normal to it) and can be calculated solving the interface Poisson equation applying the correct boundary conditions.

The expression above is valid exclusively for the free excitons case, in which the excitonic function is described as a standing wave able to move freely through the QW plane. In this particular case, the final transfer rate takes is:

$$\frac{1}{\tau_{ET}} = \frac{Im[\epsilon]}{\pi^2\hbar} \frac{|d^{vc}|^2}{a_B^2} \frac{K|C_K^Z|^2}{L_w^4} \tag{20}$$

L_b represents the width of the spacer and C_K^Z is:

$$C_K^Z = \frac{8\pi^2 q}{K(K^2 + q^2)} \frac{\sinh(KL_w/2)}{\epsilon_b \cosh(KL_b + KL_w/2) + \epsilon \sinh(KL_b + KL_w/2)} \tag{21}$$

above equation (Eq. 20) can be used to calculate the transfer rate for the system under study, and the resulting curve is presented in Fig. 11 (numerical values used here are reported in the caption).

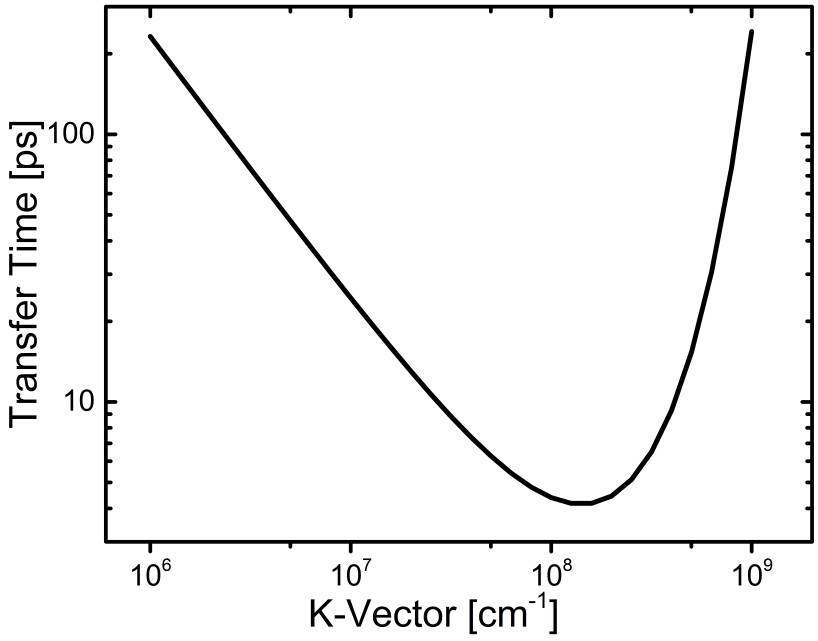

Figure 11: *Free Z-exciton lifetime τ(ns) with respect to energy transfer as functions of the in-plane wave-number k (cm^{-1}). The graph is obtained using Eq. 20 and: d_{vc}=0.1 $*$ $e * a_B$, L_w=6 nm, L_b=40 nm, ϵ_b=6, ϵ=4+3i.*

The trend shown in Fig. 11 is not unexpected: in fact it resembles the trend of the classical interaction between two dipoles-sheets. In this case, the coupling V between two planes at a distance d scales with:

$$V(k,r) \sim k * exp^{-kz} \tag{22}$$

with $\mathbf{k}$ the magnitude of the relative in-plane wave vector. This expression gives the correct asymptotic behaviours $\tau \sim 1/K$ for $K \to 0$ and exponential growth for $K \to \infty$ when applied with Fermi's Golden Rule.

Fluctuations of the QW width, alloy disorder or impurities lead to a localization of the 2D excitons.[7,40,67] For localized state, the wave function for the center-of-mass exciton motion $\Phi(\mathbf{r})$ is no longer a plane wave ($e^{i\mathbf{K}r_{||}}$ in Eq. 18), and the corresponding polarization $\mathbf{P}(\mathbf{r})$ is also localized:

$$\mathbf{P}(\mathbf{r}) = \mathbf{d}^{vc}\sqrt{\frac{2}{\pi a_B^2}}\frac{2}{L_w}\cos^2\left(\frac{\pi z}{L_w}\right)\Phi(\mathbf{r}_{||}) \tag{23}$$

in the limit of local states within a thin quantum wells ($L_b >> L_w$), where the Bohr radius and the length of localization $L \approx a_B$ are smaller than the barrier width L_b, energy transfer can be described using the point dipole approximation. This is the case where the interaction of the localized exciton with each molecule of organic material can be considered as satisfying Förster relation Eq. 14 summarized over all molecules.

A solid interface is defined as a few atomic layers that separate two solids in contact with one another. Directly correlated to the above definition, a heterojunction is the interface that occurs between two layers or regions of dissimilar crystalline semiconductors, with unequal band gaps.[68–70]
From the applications viewpoint, heterojunctions are the baseline for a number of engineering branches and advanced technologies; since most of modern semiconductor technology bases on the latter years research and understanding on surfaces and interfaces.

ENERGY LEVEL ALIGNMENT AND BAND OFFSETS

The central problem of a heterojunction can be summarized by a question: "How do the band structures of two semiconductors line up in energy with respect to each other, when the materials are joined together to form a heterojunction?".[68] This question has profound fundamental and technological implications. Supposing a heterojunction composed of two different materials with gaps $E_{g1} < E_{g2}$. Figure 12A,B show cases valid both for inorganic, organic and hybrid semiconductors pairs.

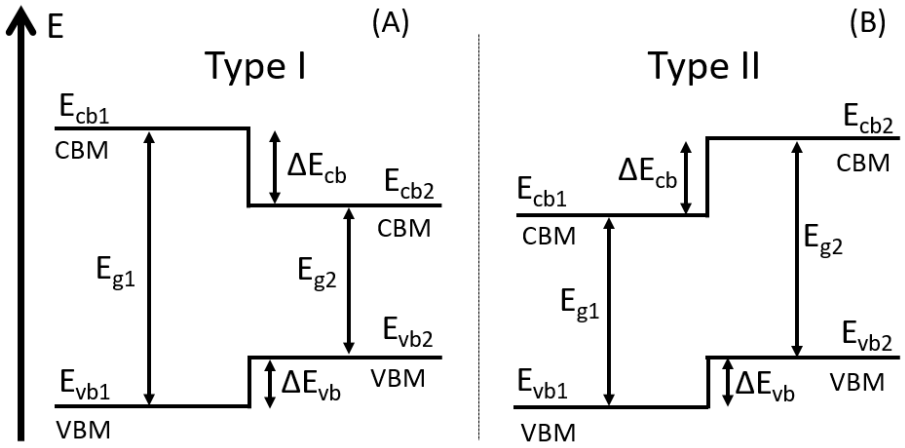

Figure 12: *Frontier energy level alignment for the two type of Heterostructures considered. (A) Type I interface. (B) Type II lieterostructures. CBM refers to conduction band minimum, VBM to valence band maximum, $E_{g1,2}$ are to the energy band gaps, $\Delta E_{vb,cb}$ refer to the energy offsets between the two materials.*

The difference $E_{g1} - E_{g2}$ must be accommodated by discontinuities in the valence and conduction bands edges, ΔE_{vb} and ΔE_{cb}. It is clear that such discontinuities play the leading role in determining the heterojunction properties: such as the transport and optical response, determining the behaviour and performances of the corresponding device.

Depending to the energy of the bands producing the discontinuity, interfaces have historically been organized into four types:[41,68,70] Type I, Type II heterostructures, Type II misaligned and Type III. These sections and this publication concentrate only on Type I and Type II, since Type II misaligned occurs only for some types of inorganic semiconductors and Type III manifest in case of a semiconductor and a semi-metal with inverted bands.[68]
In Type I heterostructures (Fig. 12A), the band gap of one material overlaps with that of the other. Both electrons and holes are confined in the lower-band-gap material for these heterostructures.
In Type II heterostructures (Fig. 12B), $E_{v1} > E_{v2}$ and ΔE_{cb} may be larger than E_{g1}. Also, E_{g2} is not necessarily smaller than E_{g1}. Both the conduction-band edge and the valence-band edge of one material being lower than the corresponding band edges of the other material, the electrons are confined in one material, while the holes are restrained in the other.

ENERGY LEVEL ALIGNMENT AT INORGANIC/ORGANIC INTERFACES

A hybrid interface is obtained when an organic species is in direct contact with an inorganic substrate. Applying the same definition reported above, the relative position of occupied and unoccupied bands (VB, CB) and energy levels of organic molecules (HOMO, LUMO), will determine the opto-electronic functionality of the HIOS.
Between the cases reported above, a type I interface will be the most suitable for light-emitting application,[3] while a light-energy conversion system will relay mostly in the charge transfer favourite by a type II interface.[71]
Due to the complexity of interface-formation between inorganic and organic species, involving processes such as redistribution of charges, interface dipole formation till chemical bonding, it is impossible to predict the energy offsets for a given material pair basing on the listed values of ionization potential and electron affinities: both semiconductors are influenced by the presence of the other. Adsorbed molecules reorganize the electronic structure of the contact surface which, in turn, determinates the molecular efficiency of photo-or electron-luminescence.[72]
When a molecule is deposited on a ZnO substrate, the resulting interface is of Type II.[13,31,73–75] This is due to the electron affinity of ZnO (approx. 4.2 eV) being larger than the respective value for most conjugated organic molecules. When a type-II energy level alignment is formed, electrons from the excited organic component quickly relax into the conduction band of the substrate, yielding a fast and efficient non-radiative deactivation of the molecular luminescence.[76] In fact, it was shown that the photoluminescence of a spiro-bifluorenene derivative is substantially quenched when in contact with ZnO due to interfacial exciton dissociation.[31] Such a configuration, detrimental when targeting light-emitting applications, is therefore fundamental for realization of photovoltaic systems.[71]

3

EXPERIMENTAL

This chapter contains information regarding the experimental conditions of the measurements discussed in following chapters. Section 3.1 gives the general hybrid sample design used in this work. The preparation techniques for the inorganic heterostructures and organic overlayers are described in sections 3.2 and 3.2.1 respectively.
Following their preparations, hybrid samples were investigated about their structural and optical behaviour. Brief descriptions for the used techniques and setups are reported in the latter sections (3.3) of this chapter.

3.1 HYBRID SAMPLES DESIGN

The realisation of a hybrid sample with efficient energy transfer requires to meet two fundamental requirements:

- Spectral overlap between the donor and the acceptor.[21,60]
- Small distance between the excitonic species involved.[18,64]

While the first point influences the donor-acceptor pair choice, the second determinates the arrangement of the two components and the general sample structure. Samples used in this work are generally structured as shown in Fig. 13.

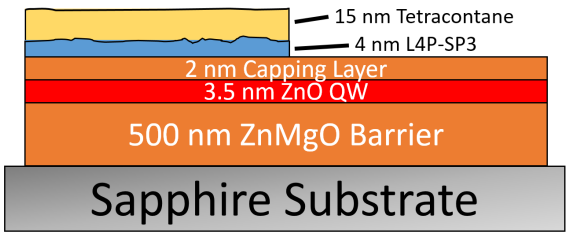

Figure 13: *Schematic of the hybrid sample consisting of a ZnO QW (red coloured) as donor and L4P-SP3 emitting layer (blue coloured) as acceptor. The QW is sandwiched in ZnMgO barriers (orange coloured) grown on a Sapphire substrate (grey coloured). A protection layer of tetracontane[77] (yellow) prevent contacts between air and molecules.*

ZnO excitons are confined into a 3.5 nm single QW embedded between a thick ZnMgO barrier and a thin ZnMgO capping layer. The thick barrier ($>$ 500 nm) guarantees a good crystal quality of the heterostructure,[30] as growth defects like dislocations annihilate before reaching the ZnO cap. The thin cap (approx. 2 nm), instead, maximizes the inorganic/organic coupling still granting good quantum confinement in the well. Half of the sample surface is covered with a thin (approx. 3-4 nm) molecular overlayer, notably in this case L4P-SP3 (Ch. 5). The half coverage allows to compare hybrid and reference sample on the same QW substrate. The thickness of the overlayer is also a crucial point for ET experiments, as only the molecules closest to the interface will be sensitized. For excessive thick overlayers, signal contribution from the farer molecules will interfere with the ET measurements. On top of the molecular layer, approx. 15 nm of Tetracontane[77] are evaporated to prevent contacts between the molecules and air.

3.2 SAMPLES PREPARATION

The realization of a high quality hybrid interface requires considerable efforts. In the preparation of the organic layers, exposure to air can have dramatic effects: oxygen can strongly reduce the photo-stability of organic molecules,[1,78] and air can harm the structural stability of thin films.[74]
To prevent any exposure of the samples to air, the heterostructures and the organic overlayers are prepared using ultra high vacuum (UHV) techniques such as molecular beam epitaxy (MBE) and organic molecular beam deposition (OMBD). To prevent any air-contamination, the intermediate transport between growth chambers also takes place in UHV environments.

Molecular Beam Epitaxy and QW growth

Molecular Beam Epitaxy (MBE or solid-source MBE) is the defined deposition of epitaxial films onto heated substrates using atomic and molecular beams under UHV conditions. MBE is an extremely versatile technique for preparing thin semiconductor heterostructures, because it yields precise control over the growth parameters and in-situ diagnostic capabilities. These are vital for efficient energy transfer: any ET investigation depends on the precision and control over the thicknesses and morphologies of both the capping and the QW layers.
The QW structures are prepared with atomically smooth interfaces in a layer-by-layer growth regime.[30] Heterostructures produced for this work are grown on a-plane sapphire substrates which induce a growth along the c-axis of a wurtzite crystal and result in the O-terminated (000-1) ZnO surface. To achieve quantum confinement and good excitons capturing in the well, ZnO is embedded between two ZnMgO barriers with a Mg composition of 11%. Since the barrier band-gap $E_{g,ZnMgO}$=3.6 eV is higher than for ZnO ($E_{g,ZnO}$=3.4

eV), a later selective excitation of the sole well is enabled. A more detailed description of the QW preparation can be found elsewhere.[30,79]

A particular advantage of MBE is the preparation of atomically smooth, largely intrinsic surfaces as the starting point for a subsequent deposition of molecules. While hydrogen impurities are frequently observed in ZnO crystals, secondary-ion-mass spectroscopy of MBE-grown films used here demonstrates that the hydrogen concentration is below 10^{16} cm^{-3}.[30,79]

Sample Transport and Storage: All-UHV Procedure

ZnO heterostructures produced by MBE must be transferred into the organic molecular beam deposition (OMBD) without intermediate breaking of the UHV. This is the first critical part in the realization of an hybrid structure[74] and for this purpose, a special transport vacuum chamber (Fig. 14) was realized:

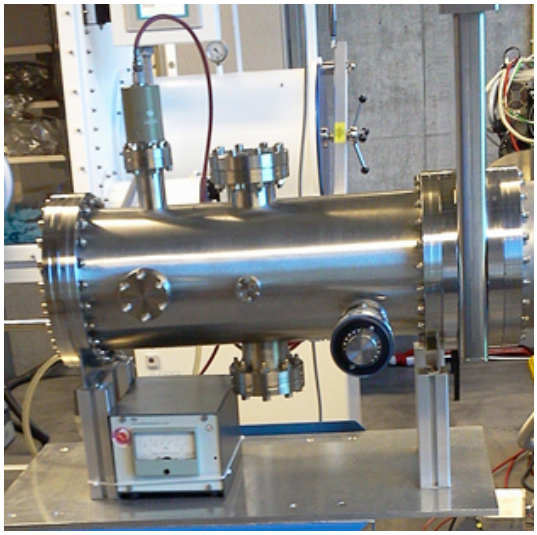

Figure 14: *Vacuum chamber used for sample transportation: this chamber is designed to stand UHV and to be connected to MBE and OMBD lock-in; a special external adaptor allows connection to a glove-box.*

The transport chamber is compatible with load-locks of both the MBE and OMBD chambers, and can store samples with an internal pressure of 10^{-8} mbar. Thanks to this transport chamber, the inorganic samples can be either transferred to a glove-box for further characterizations, or to the OMBD for additional growth of organic overlayers. In the glove-box a nitrogen atmosphere, with oxygen and water concentrations less than 0.01 ppm, replaces the UHV. Samples are than extracted and for optical characterization.

If an additional organic film should be grown on the sample, the transport chamber is connected to the load-lock of the OMBD, where the organic overlayer is grown. After deposition, hybrid samples are than transferred into the glove-box through the vacuum chamber. Once under nitrogen atmosphere, samples can be installed into the flow cryostat.

A drop of silver paint between sample and sample-holder ensures optimal thermal conductivity. Once inside of the cryostat, samples are transported to experimental setups for optical characterization.
This procedure has two important consequences:

- The ZnMgO surfaces under study can be considered "pristine", despite the extra deposition and the experiments being carried outside of the growth chamber.
- The organic layers can be considered Water and Oxygen free, resulting in a better photo- and structural stability.

3.2.1 *Organic Molecular Beam Deposition*

Molecular layers within this work are prepared using an Organic Molecular Beam Deposition (OMBD) apparatus which is similar, in many respects, to conventional molecular beam epitaxial growth systems.[80] Typically, growth occurs by the evaporation in an UHV ranging from 10^{-8} to 10^{-9} mbar of a highly purified powder by a Knudsen-type effusion cell. The flux of the molecular beam is controlled by the Knudsen cell temperature: typical growth rates range from 0.1 to 4 Å/s. A mechanical shutter allows the beam flux to the substrate and is thus a key element, since it allows to start the organic deposition only at the desired growth rate. The lower end of this range has a danger of adsorbing contaminants onto the surface, whereas at higher rates, growth is extremely difficult to control. Growth rate is measured using a quartz crystal micro-balance.[55]
Before a growth run, the Knudsen cell is heated below the material sublimation temperature in order to continuously out-gas the source. The UHV storage of the source material at elevated temperatures is a key factor in eliminating impurities and moisture.[80]

A shadow mask allows to deposit the organic layer only on a portion of the sample surface, leaving always a pristine area for reference measurements. Upon deposition of the molecular layer, a 15 nm layer of Tetracontane[77] (C40) is deposited on the samples (Fig. 15) at approx. 5 Å/s .

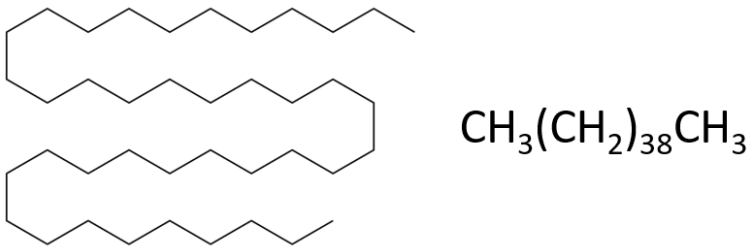

Figure 15: *Chemical structure and formula for tetracontane.*

Tetracontane ($C_{40}H_{82}$) is a wide gap saturated alkane that grow up-right

standing on ZnO and sapphire surfaces.[77] Being the C_{40} chain approximately 5 nm long, 15 nm correspond to 3 layers of the molecules.

The particular morphology and structure of deposited films is a balance between the molecule-substrate and molecule-molecules interactions.[69] In general, growth is divided into three predominant modes:

- Frank-van der Merve growth: For this case substratemolecule interactions outweigh the molecule-molecule interactions. Molecules will grow in a layer-by-layer fashion, closing proceeding layers first.
- For the opposite case of superior molecule-molecule interactions the molecules nucleate to islands, which is called Volmer-Weber growth.
- There further exist an intermediate case (Stranski-Krastanov growth), in which one or a few closed monolayers are formed before subsequently island growth prevails. Here, the first closed monolayer modifies the substratemolecule interactions to a point that continued layer-by-layer growth is unfavourable.

Knowledge of the growth mode is critical for the interpretation of ET data.

3.2.2 *Non-UHV Layer Preparation: Spin Coating*

Spin coating is technique to create organic layers from solutions. The achievable layer thickness range from few nm to μm. For the present work, this technique was selected to prepare homogeneous films of a polymer (polymetilmetacrilate, PMMA or polystyrene, PS) containing a certain weight percentage (wt. %) of the molecular species under study. The spin coater used for the fabrication of samples was a Schaefer Technologies GmbH SCI-20 with adjustable top speed.
Layers are prepared by dripping few drops of a solution are tapped on a substrate which is successively pivoted at a constant speed (40-50 rotation per seconds) thus, removing all the excess solvent from the surface. The thickness of the polymeric layer adjusted by the concentration of the solution and by the rotation speed.[81] This technique creates a surface with high flatness and nearly constant thickness. Because of its straightforwardness samples can be prepared in short time. On the other side, since the film preparation takes place under ambient conditions, species like oxygen and water are always incorporated into the films, with detrimental effects on the molecules stability.[1]

3.3 CHARACTERIZATION TECHNIQUES

This section contains short summaries of the measurement techniques used in the coming chapters.

3.3.1 *Optical Measurements*

PHOTOLUMINESCENCE SPECTROSCOPY

Photoluminescence is the emission of photons from electronically excited states.
Standard photoluminescence spectroscopy is performed using the Xenon lamp for optical excitation. A scheme of the setup in shown in Fig. 16.

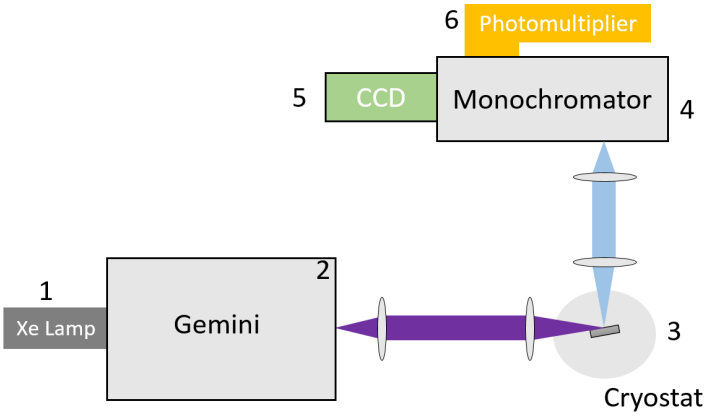

Figure 16: *Experimental setup for angular photoluminescence and photoluminescence excitation spectroscopy.*

The excitation wavelength is selected by a double Monochromator Horiba Gemini-180(2) in additive configuration. A double monochromator has the advantages of a high scattered light suppression and high spectral resolution (dispersion = 1.77 nm/mm). The Xenon lamp(1) allows for an excitation range from UV (4.2 eV) down to visible (2.3 eV). The samples are mounted in a helium bath cryostat(3) custom built by the "Klaus Schaefer Gesellschaft fuer Verfahrenstechnik GmbH" with three quartz windows for optical access. The light emitted by the samples is collected and focused into a ACTON SP2300 monochromator(4) with a focal length of 0.3 m. The monochromator mounts two gratings with 300 and 2400 lines/mm, respectively.
PL spectra are acquired with a CCD camera PIXIS256E(5). The recorded wavelength are corrected for the vacuum wavelength and converted into electron volts using the relation: 1 eV correspond to 1239.842 nm.

Closely associated with photoluminescence is the photoluminescence excitation spectroscopy (PLE). An excitation spectrum is the dependence of emission intensity at a single wavelength, upon the excitation wavelength. PLE is similar to absorption in some sense, with much better sensitivity. Detection limits can be three orders of magnitude smaller than those encountered in absorption spectroscopy.[58] For these measurements, the ACTON SP2300 monochromator(4) is set to some wavelength value inside the emitted photoluminescence band and excitation energy is scanned with the GEMINI(2), intensity changes of the emission are recorded by a photomultiplier tube(6). The advantage of this technique is its sensitivity. Like photoluminescence, excitation spectroscopy doesn't require thick samples, as it must be used in the case $\alpha * d \ll 1$ (with α the absorption coefficient and d the sample thickness). This technique, thus, can be used to resolve absorption spectra of thin molecular layers (2-4 nm) and of single heterostructures (2-3.5 nm). An example of PL/PLE measurement is reported in Fig. 17A,B.

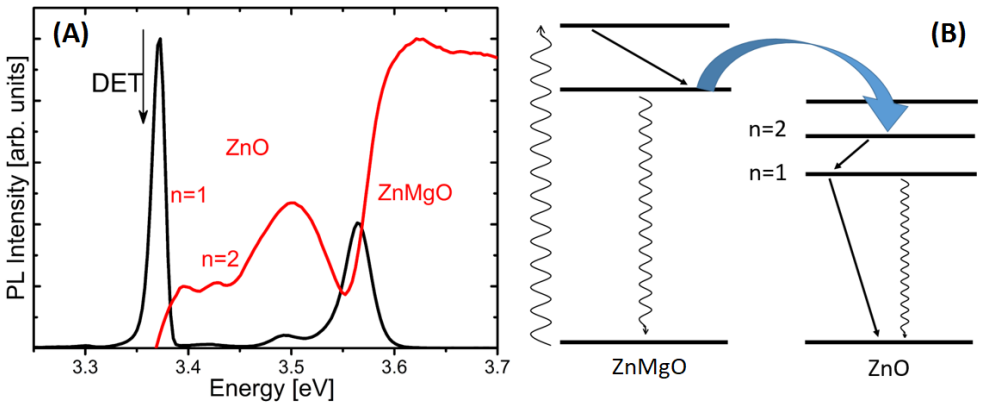

Figure 17: *Photoluminescence and excitation spectra: (A) Low temperature PL spectrum (black line) for a ZnO/ZnMgO SQW, the red line is the excitation spectrum acquired at approx. 3.35 eV (black arrow). (B) Jablonski diagram showing the electronic transition measured with the PLE spectrum in (A).*

The above figure reports the low temperature emission (black line) and excitation (red line) spectra of a ZnO/ZnMgO SQW acquired with the PL/PLE setup. The excitation spectrum performed on the QW emission (E_{det}=3.37 eV) allows to unveil the physical origin of the emitted signal from the heterostructure and can be understood with the Jablonski diagram shown if Fig. 17B.
The excitation is scanned from 3.3 eV with increasing energies, for $E_{exc} > 3.4$ eV, the QW begins to absorb, and the luminescence signal increase as the GEMINI scans over the excitonic resonances n=1 and n=2 (E_{exc}=3.41 and 3.45 eV). For higher energies ($E_{exc} > 3.55$ eV), the PLE spectrum displays the absorption band edge of the ZnMgO barrier. The latter feature indicates efficient capture of photo-excited carriers by the QW. For higher excitation energies ($E_{exc} > 3.6$

eV) the PLE spectrum saturates, as the thickness of the barrier invalids the $\alpha * d \ll 1$ limit.

μ-PHOTOLUMINESCENCE SPECTROSCOPY

The μ-PL setup is shown in Fig. 18. The excitation source is a mode-locked Titan Sapphire laser Mira 900(2) from Coherent (5 W/cm^2, 76 MHz), pumped by a VERDI V18 Nd:YAG laser(1). The setup allows μ-meter resolution as the laser is focused by micro optics(3) Olympus LUCPlan FLN to a radial symmetric spot of about 3 μm in diameter. An interchangeable holder, enables to switch to a M PLAN APO NUV microscope with 100X magnification for high spatially resolved (spot size approx. 1 um) experiments. The MIRA produces pulses shorter than 200 fs. Due to these short pulses, the spectral width is approx. 6 nm (FWHM). The red emission of the MIRA is converted into UV light by a frequency-doubling crystal(4). Luminescence signal is recorded using an Acton SpectraPro 2500i spectrometer(5) with 0.5 m focal length. The monochromator mounts two gratings with 300 and 2400 lines/mm and enables a dispersion of 1.6 nm/mm. PL spectra are acquire by a liquid nitrogen cooled Acton SPEC-10:100 CCD camera(6). The emitted light is detected in backscattering geometry as the sample are cooled by a flow cryostat Oxford Instrument MicroHR2(7).

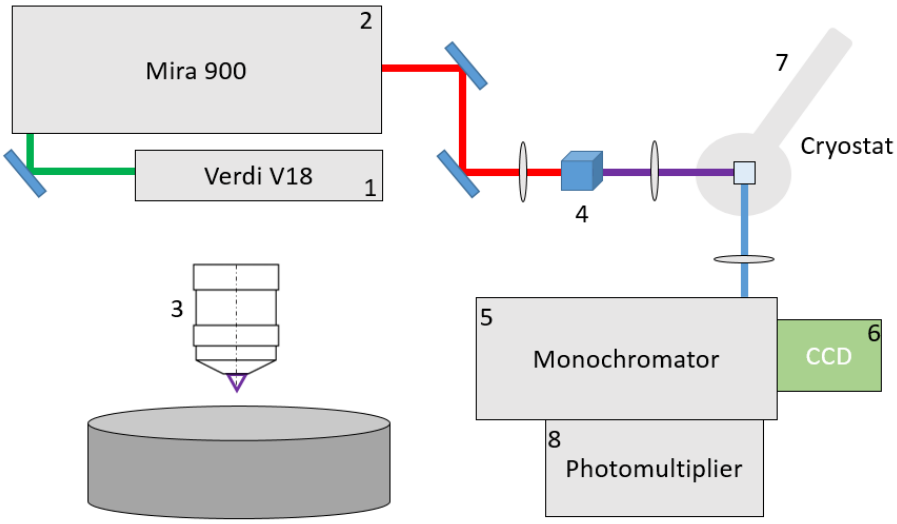

Figure 18: *Experimental setup for angular photoluminescence and photoluminescence excitation spectroscopy.*

Time-resolved PL measurements (TRPL) were performed using the same pulsed Ti:Sapphire. In these experiments PL transients are obtained by time-correlated single-photon counting using a microchannel plate photomultiplier(8) HAMAMATSU R3908 mounted to the side exit of the same monochromator.

The overall time resolution obtained is of 30 ps. Data fits, and so the decay time of PL transient curves are obtained by:

$$I_{QW}(t) = \int_0^t dt' K(t') N(t - t') \tag{24}$$

where $K(t)$ represent the system response to the excitation pulse, the deconvoluted exciton population $N(t)$ yields to the lifetime τ.

QUASI-CONTINUOUS LASER CHARACTERIZATION

The lasers called quasi-continuous wave have a repetition rate of around 80 MHz. For such type of measurements, the excitation source selected is a synchronized Coherent 700 dye laser(2) pumped by a frequency doubled Nd:YVO_4 laser(1). The dye laser emits in the red range and it can be again frequency doubled(3) to UV/blue light. The laser light is focused on the sample with a spot of approx. 0.1 mm diameter. The samples are mounted in a helium bath cryostat(4) equivalent to the one for PLE characterization.

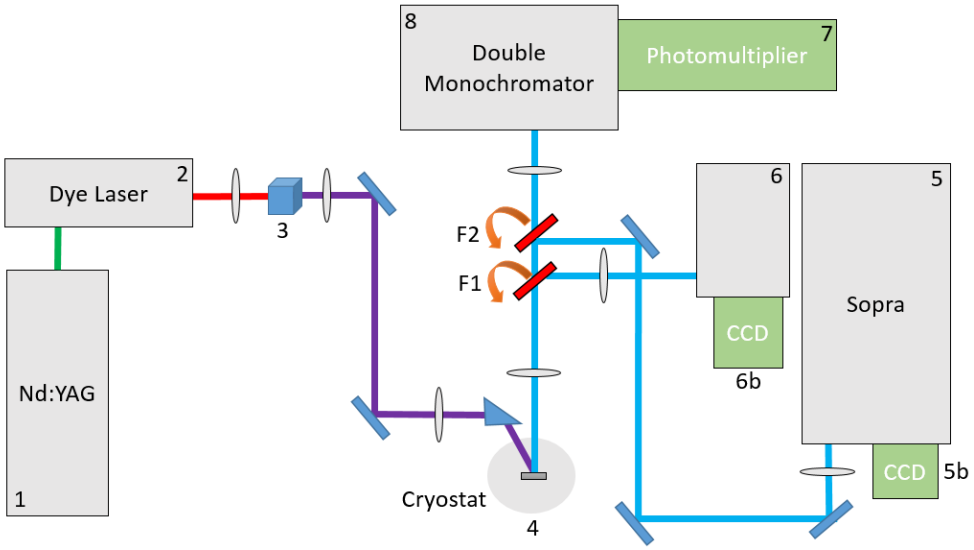

Figure 19: *Experimental setup for angular photoluminescence and photoluminescence excitation spectroscopy.*

The advantages of this setup compared with the μ-PL equivalent, is the least laser width of the dye laser (approx. 1 meV). Unlike the above geometry, here the light emitted from the sample can be collected by three different apparatus.

In one case, the light is dispersed by a 1.1 m monochromator SOPRA(5), with a 600 lines/mm grating and a dispersion of 1.6 nm/mm, the spectra are acquired by a liquid nitrogen cooled camera(5b) EG&G Princeton Applied Research CCD Mode. High resolution is important for characterization of heterostructures. By switching a flipping mirror(F1), the light emitted by the sample is dispersed by a 0.3 m ISA Instruments monochromator(6) with a

300 lines/mm, spectra are acquired by a CCD analogous to (5b). This "low resolution" detection arm is used for molecular emission measurements.
Upon turning the two flipping mirrors(F1,F2), PL transients are obtained by time-correlated single-photon counting using a micro-channel plate photomultiplier(7). Before reaching the photomultiplier, incoming light is dispersed by a double monochromator in subtractive mode(8) Yobin Yvon HR 250.

UV-VIS SPECTROMETER

A widely automatic UV-VIS spectrometer Shimadzu UV-2101PC is used as standard characterization method. This device allows precise and reproducible transmission measurements at room temperature. A combination of tungsten and a deuterium lamp enables to measure on a range of wavelength from 190 to 900 nm. The resolution can be tuned down to a minimum of 0.1 nm.

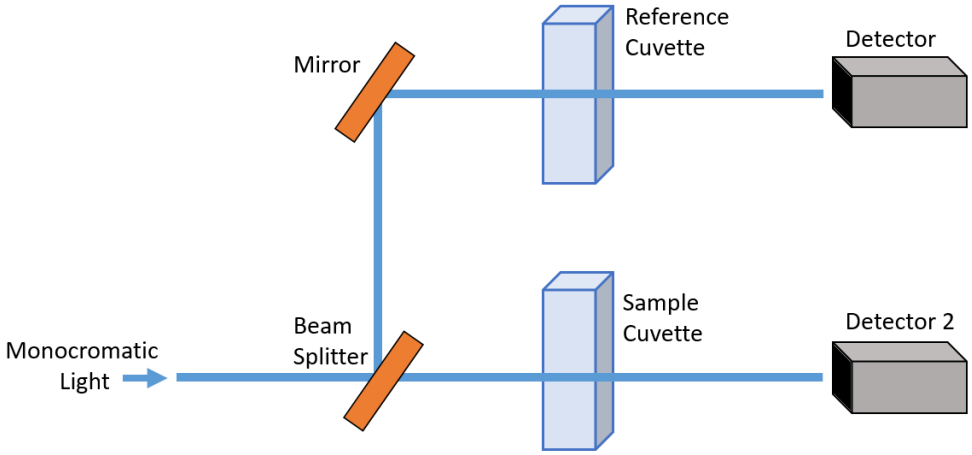

Figure 20: *Experimental setup for angular photoluminescence and photoluminescence excitation spectroscopy.*

Transmission and absorptions spectra were used to characterize magnesium concentration in heterostructures and molecular concentration/thickness for a organic samples respectively. In the specific, magnesium content of the ZnMgO barrier can be extracted from transmittance spectra, observing the position of the sample absorption band edge.[30]

3.3.2 *Ultraviolet Photoelectrons Spectroscopy*

Photoemission spectroscopy (PES) is a technique for electronic characterization of interfaces. It relies on the photoelectric effect: emission of electron from matter upon absorption a photon of given energy E_{photon}=$h\nu$. The kinetic energy E_{kin} of the ejected electron is given after Einstein by:

$$E_{kin} = h\nu - E_B - \phi \tag{25}$$

where E_B is the binding energy of the electron, and ϕ is the work-function of the material. Because of its nature, PES measurements give information about the occupied electronic structure, also called valance bands. Koopmans theorem[70] assumes that all the energy levels of a molecule remain unchanged during the ejection of an electron. Consequently, the first ionization potential I of a closed-shell system is equal to the negative orbital energy of the HOMO, i.e., the binding energy. Hence, PES maps directly the occupied density of states (DOS) in good approximation. Particularly, in ultraviolet photoelectrons spectroscopy (UPS), light emitted by a helium discharge lamp at $h\nu$=21.22 eV (He-I) is usually used to eject valence electrons in the proximity of the Fermi level E_F, and their kinetic energy E_{kin} is analysed.
There are two different main processes that are observed in a UPS spectrum:

- The primary (photo-)electrons: the ones that do not undergo inelastic scattering within the material.
- The secondary (photo-)electrons: the ones that undergo inelastic scattering events within the material as they travel out of it.

Primary electrons do not lose their energy and hence they do not lose information about the initial state they existed. They produce distinct spectral features, representing in first approximation the Density of States of the material. Binding energies of electronic states can be extracted from these features.
The majority of the secondary electrons undergo inelastic collisions, hence they are ejected out of the material with reduced kinetic energy. The secondary electrons give a continuous background that is superimposed with the distinct features given by the primary electrons. Signal onset stemming from these electrons is used to calculate the work function of the material.
Besides pinpointing the energy of detected electrons to the corresponding states in the sample one can also use PES to measure the samples work function ϕ via the position of the secondary electron cut-off (SECO). Inelastically scattered electrons having not enough energy to overcome the samples work-function cannot escape the sample, yielding a cut-off in the spectra. A more detailed description of UPS and SECO can be found elsewhere.[82]

UPS shown in this publication are performed at PM4 beamline at Bessy (Germany) consisting of an interconnected sample preparation analysis UHV apparatus with a base pressures between 10^{-8} and 10^{-10} mbar. Photoelectrons

excited with 35 eV UV light are detected by a Scienta SES 100 spectrometer with approx. 200 meV energy resolution.

3.3.3 *Atomic Force Microscopy*

Atomic force microscopy (AFM) is a valuable technique to resolve the morphology of deposited organic thin films. In contrast to X-ray techniques, AFM allows one to study the films in real-space and gain direct information about the densities of molecular islands, their size and shape.
An AFM consists of a cantilever with a sharp tip (probe) at its end that is used to scan the specimen surface. The tip scans a defined area of the sample (usually 100x100 μm^2), which is the reason for the AFM being also referred to as scanning force microscope (SFM). When the tip is brought into proximity of a surface, forces between the pair lead to a deflection of the cantilever. The latter is measured using a laser spot reflected from the top surface of the cantilever into an array of photo-diodes

In general, possible imaging modes are divided into static (also called contact) modes and of dynamic (intermittent-contact) modes.
In contact mode, the tip is "dragged" across the sample and contours of the surface are measured. Contact mode can also be used to modify actively the sample. By scraping the tip onto a surface, is possible to drag and/or sweep molecules physically adsorbed.
In intermittent-contact mode, the tip does not touch the sample surface instead, the cantilever is forced to oscillate near its resonant frequency at a fixed surface-ti distance. Interactions between sample and tip decrease the resonance frequency of the cantilever. The software reconstructs a topographic image of the sample surface by measuring the damping and the phase-shifting of the interaction.

AFM pictures shown in this publication were recorded using a JPK NanoWizard 3 apparatus performed under ambient conditions. Morphology images were recorded using the non-contact mode. Thickness of the molecular overlayer were extracted by scratching a section of the layer using the tip in contact mode and than remeasuring the morphology.

3.3.4 *X-Ray-Reflectometry*

X-Ray-Reflectometry (XRR) is a method used for monitoring the growth regime of a molecular layer. XRR can be used to characterize the out-of-plane crystallinity. However, the field of application is not restricted to well-ordered structures. The technique can also be applied to amorphous materials in order to unravel properties like electron densities, film thicknesses and roughnesses in the range of few Ångström.
In XRR, a monochromatic X-ray beam of wavelength λ irradiates a sample at a grazing angle ω and the reflected intensity at an angle 2θ is recorded by a detector. Reflections at the surface and interfaces is due to the different electron densities in the subsequent layers (films), which corresponds to different reflective indexes in the classical optics. For incident angles θ below a critical angle θ_c, total external reflection occurs.
The density of the material is determined from the critical angle, which is for most materials less than 0.3. Above θ_c the reflections from different interfaces interfere resulting in fringes. The period of the interference fringes and the fall in the intensity are related to the thickness and roughness of the layer (layers in case of multi-layers). The reflection can be analysed using the classical theory (Fresnel equation). The XRR curves of BPA, 5FBPA and 3FMBPA were acquired on an X-ray diffractometer with a rotating Cu-Kα anode source. The measurements shown in this publication, were performed in a high vacuum (HV) chamber at a pressure of 10^{-6}-10^{-7} mbar to avoid beam damage by Ozone. Measurements in the university laboratory (Hu Berlin; AG KOH) were performed with an EFG/Rigaku rotating anode Cu Kα x-ray system featuring a comparatively high flux of 500M counts/s in the primary beam. The diffractometer uses up to 4 rotational and 2 transitional degrees of freedom and is equipped with a scintillation detector counter.

4

PHOTOPHYSICAL PROPERTIES OF L4P AND DERIVATIVES

4.1 MOTIVATION

Innovative HIOS structures are meant to exploit efficient electrical injection and high excitation density of inorganic semiconductors with the high radiative emission yield of organic semiconductor. It is thus clear that the excitation transfer between the two components have a key role in the overall system design. Inspired by this combined route of function sharing, previous works already addressed theoretical and experimental aspects of HIOS, such as the presence of efficient energy transfer.[14,15,17,18,83]
However, most of the studies so far still have not truly demonstrate the HIOS superior potential for light emission. The low temperature transfer efficiency is still comparable with the radiative transfer for phosphors-based OLEDS (65-67%[11]) and the room temperature coupling has still to be achieved.[27]
In this chapter, a ladder-type quaterphenyl is chosen (L4P, chemical structure see Fig. 21), as energy transfer partner for ZnO.[1,36]

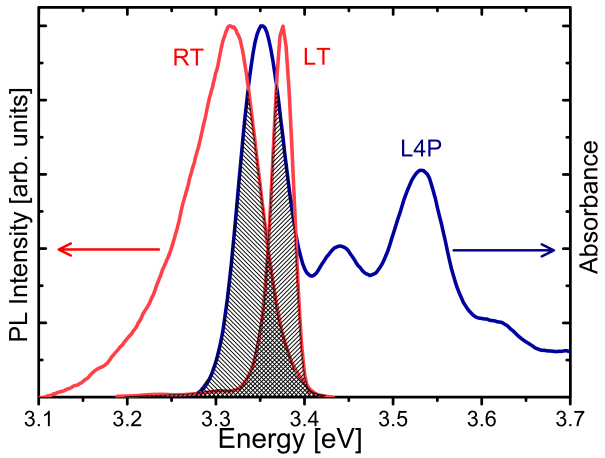

Figure 21: *Spectral overlap of the PL spectrum (red line) of the sole QW structure (L_{QW}=3.5 nm) and absorption spectrum of L4P (blue line) on sapphire.*

The selection of L4P as hybrid emitter is meant to target directly the limited performances of ”state of the art” hybrid devices, often relying on organic

polymers as final emitter.[64,65] The latter are, by their nature,[8,45] characterized by broad and unstructured spectra and thus showing a limited spectral overlap with the quantum structure donor, characterized by sharp optical transitions.

Because of its rigid planar geometry, L4P exhibits superior photophysical properties as compared to non-rigidified oligophenyls:

1. weakly Stokes-shifted absorption and emission,
2. spectra with well-resolved vibronic progressions,
3. QY close to unity in solution.

The small Stokes shift facilitates energy migration within the organic layer, and L4P $S_0 \rightarrow S_1$ transitions, characterized by prominent vibronic features, cover the exciton resonance region of ZnO.

4.2 STRUCTURE OF THE CHAPTER

This chapter presents energy transfer experiments between high quality ZnO SWQ and thin layer os L4P dissolved into an inert polymeric layer. Luminescence, excitation luminescence and time-resolved measurements are fist performed on a pristine ZnO sample. Energy transfer measurements are performed on the same QW after the deposition of the molecules.
Final sections of this chapter are dedicated to L4P degradation. Kinetics and mass spectrometry studies of L4P in solution, including results concerning the identification of the L4P-photo-degradation product, are reported elsewhere.[1] The later experiments focus on optical properties of L4P in solid state, considering in particular interactions between pristine and degraded L4P.

L4P FILMS PREPARATION: SPIN-COATING

Despite its stability to vacuum deposition, OMBD samples of L4P on Al_2O_3 (and other oxide surfaces) show a three-dimensional Volmer-Weber growth mode (Fig. 22A). High surface diffusivity and a strong tendency of L4P to crystallize favour the formation of large clusters with an average height of approx. 250 nm. The deposited amount of material corresponds to a nominal film thickness of 3 nm only. This grown regime was found to be independent of the substrate temperature, which was kept between 90 and 300 K.[36]
To obtain smooth thin films with a high concentration of molecules, L4P was dissolved in Polystyrene (PS) with a defined weight %. The resulting spincasted layer displays the targeted closed layer structure with the desired thickness (Fig. 22B).[81]

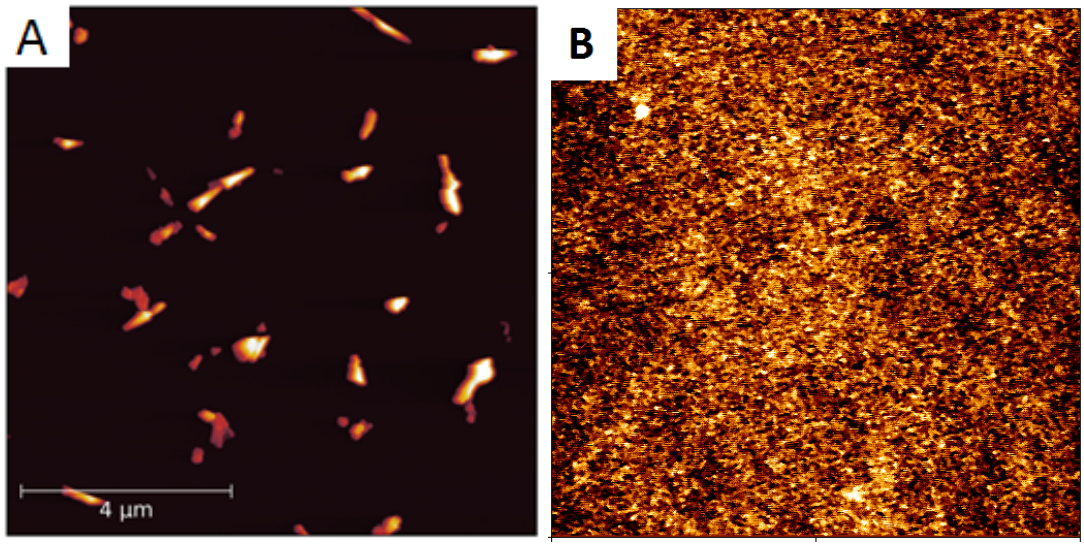

Figure 22: *AFM image for L4P samples. (A) AFM image for a L4P layer prepared by OMBD on a sapphire substrate. (B) AFM image for a L4P:PS layer on sapphire prepared by spin-coating.*

PS was selected because of its high glass transition temperature (T_g=120 °C), that should inhibit entirely molecular diffusion and prevent the formation of aggregates. PS, rather than other transparent polymers, was also selected because of its impermeability to air. Films were prepared from toluene solutions.[81]
For ET experiments, L4P was dispersed with a concentration of 20 wt.% and 3 nm films were spincasted on a 3.5 nm ZnO SQW. A 2 nm layer of $Zn_{0.9}Mg_{0.1}O$ acts as a spacer between the molecules and the ZnO well. Reference measurements were performed on equivalent films spincasted on sapphire substrates. Layers thicknesses were extracted from AFM measurements (Fig. 22B) and

absorption spectra. The latter were also used to monitor the L4P concentration in the films using:[8]

$$A = dM\epsilon \tag{26}$$

where A is the measured absorbance, d is the optical path-length and M is the molar concentration. ϵ is the L4P extinction coefficient (100000 $M^{-1}cm^{-1}$[36]) extracted by low concentration solution measurements. 20 wt.% samples were selected for ET experiments, being the latter value close to the L4P solubility limit in the polymer.

ENERGY TRANSFER EXPERIMENTS

The occurrence of ET are elucidated by photoluminescence excitation and time resolved spectroscopy. In order to limit the effects of photo-degradation during the experiments, low excitation density (0.35 W/cm^2) and short integration time (20 s) were chosen. In addition, each spectrum was acquired on a new, pristine sample position. All measurements here shown were acquired at Helium (approx. 4 K) temperature.

ENERGY TRANSFER BETWEEN ZNO AND L4P

PL and PLE spectra of the hybrid sample are shown in Fig. 23A,B. The luminescence spectrum of the sample displays both the QW emission at 3.37 eV and the L4P spectral features (Fig. 23A). The molecular signal is magnified by a factor of 10 for better visibility.
The sole QW excitation spectrum (E_{det}=3.35 eV, red line in Fig. 23B) reveals the substructure of the valence band and the ZnMgO barrier band edge, the latter being indicative of efficient carrier capture by the QW. Below the barrier edge, the excitonic n=1 and n=2 transitions are resolvable at 3.41 and 3.5 eV respectively. Energy transfer is evidenced by the prominent ZnO QW and ZnMgO barrier absorption features in the PLE spectrum acquired on the L4P emission (E_{det}=3.28 eV, black curve in Fig. 23B)

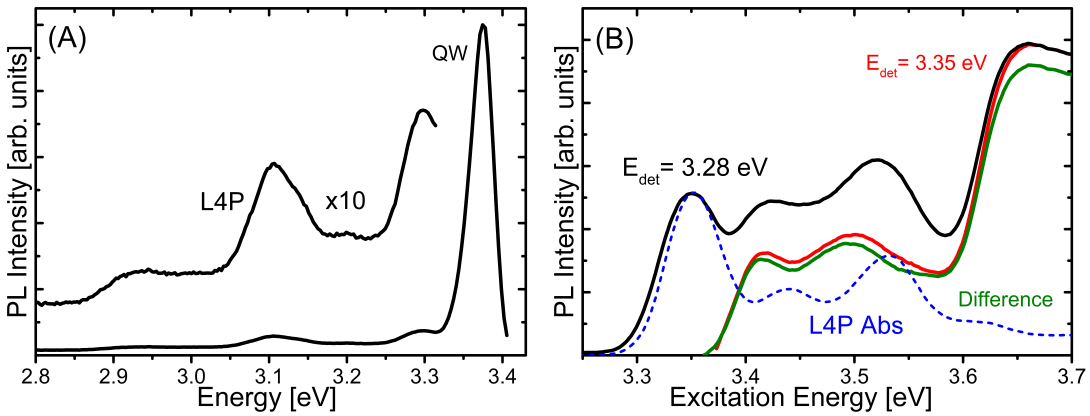

Figure 23: *Energy transfer in L4P/ZnO hybrid structures: (A) PL spectrum of the hybrid sample, luminescence generated by the L4P is magnified by* 10 *times for better visibility, E_{exc}=3.45 eV. (B) PLE spectra for the hybrid structure: spectrum of L4P on Al_2O_3 (blue dotted line), spectrum detected on the ZnO emission (E_{det}=3.35 eV, red line) and spectrum detected on the L4P emission in the hybrid sample (E_{det}=3.27 eV, black line). The green line is the result of subtracting the blue curve from the black curve.*

Subtracting the sole L4P absorption measured on a reference sample (blue line) from the "hybrid" PLE, the ZnO excitation spectrum is recovered (green curve): proving that the hybrid excitation spectrum is a convolution between inorganic and organic components, and that ZnO feeds the molecular luminescence.

The non-radiative character of the energy transfer is validated by QW PL-transient behaviour upon deposition of L4P, see Fig. 24.

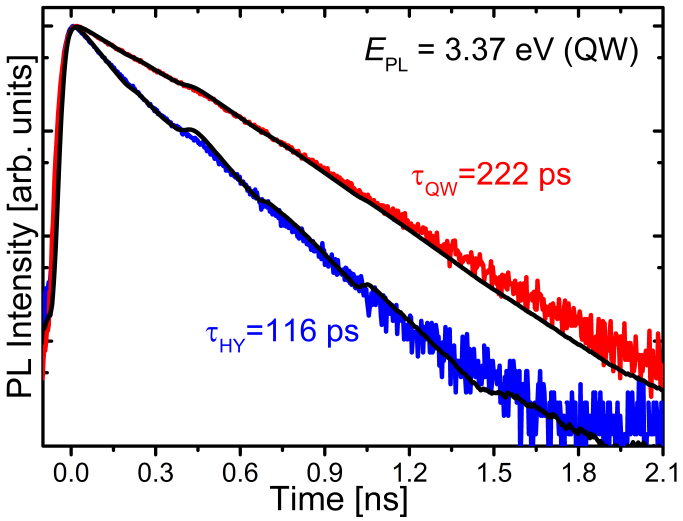

Figure 24: *PL(t) spectra for L4P/ZnO hybrid structure. Comparison of the normalized PL decay curves detected at the QW peak with (blue curve) and without (red curve) the L4P:PS overlayer. The black solid lines correspond to single-exponential fitting curves.*

For the pristine ZnO/ZnMgO QW, emission from the exciton ground-state decays in good approximation single exponentially with a time constant of τ_{QW}=222 ps (red curve). When in contact with L4P, the QW lifetime shortens to τ_{QW}^{H}=116 ps (blue curve).

Energy transfer can be described with a rate equation model of two two-level systems. Without any coherent effects, populations of the excited state for the QW and of L4P are respectively:

$$\begin{aligned} \dot{\eta}_{QW} &= g_{QW}(t) - \left(\frac{1}{\tau_{QW}} + \frac{1}{\tau_{ET}}\right)\eta_{QW} \\ \dot{\eta}_{L4P} &= g_{L4P}(t) + \frac{1}{\tau_{ET}}\eta_{QW} - \frac{1}{\tau_{L4P}}\eta_{L4P} \end{aligned} \tag{27}$$

where τ_{QW} and τ_{L4P} are the lifetimes for QW and L4P measured in separate samples, τ_{ET} is the non-radiative transfer time, $g_{QW}(t)$ and $g_{L4P}(t)$ are the generation rates for the QW and L4P excited states. Supposing an ultra-short excitation, the above system of differential equations can be solved as:

$$\eta_{QW} = \hat{g}_{QW} * exp^{(-t/\tau_{HB})} \tag{28}$$

$$\eta_{L4P} = \hat{g}_{L4P} * exp^{(-t/\tau_{L4P})} + \hat{g}_{QW}\frac{exp^{(-t/\tau_{L4P})} - exp^{(-t/\tau_{HB})}}{\tau_{ET}\left(\frac{1}{\tau_{HB}} - \frac{1}{\tau_{L4P}}\right)} \tag{29}$$

with:

$$\hat{g}_{QW/L4P} = \int_{-\infty}^{+\infty} g_{QW/L4P}(t)dt \tag{30}$$

Eq. 28 is crucial to understand the experimental evidence of Fig. 24, when in contact with an acceptor specie, the QW lifetime shortens to τ_{HB}=τ_{QW}-τ_{ET}.

Using the above model, measurements result can be used to estimate of the transfer time τ_{ET} with:

$$\frac{1}{\tau_{ET}} = \left(\frac{1}{\tau_{QW}} - \frac{1}{\tau_{QW}^{H}} \right)^{-1} \tag{31}$$

in this case τ_{ET}=232 ps.
The transfer efficiency is defined as:

$$\eta_{ET} = \frac{\tau_{HY}}{\tau_{ET}} = 1 - \frac{\tau_{QW}^{H}}{\tau_{QW}} \tag{32}$$

here η_{ET}=0.48 which means that 5 out of 10 QW excitons are transferred to the L4P.

TRANSFER EFFICIENCIES AND STRUCTURAL LIMITATIONS

Aside from proving the ET process, it's important to spend some words on the nominal efficiency obtained (approx. 50%). Molecules are dissolved into a matrix to obtain a homogeneous distribution of acceptors, nevertheless only species directly in contact with the hybrid interface are effected by ET, molecules further away are barely influenced.
Acceptors are randomly dispersed at any distance from the ZnO interface but it's possible to predict their average disposition among the thing film. As shown in Fig. 25A, L4P molecules can be approximated to cylinders of approx. 1.7 nm long and diameter of approx. 0.7 nm.

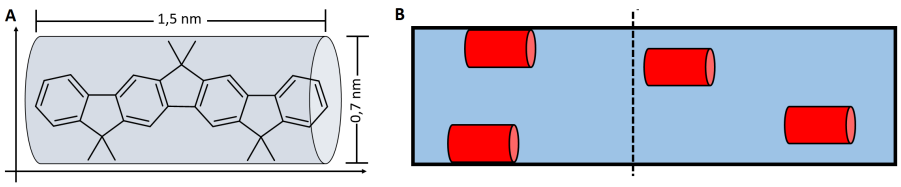

Figure 25: *L4P in Polystyrene. (A) L4P chemical formula approximating the structure to a cylinder of approx.* 1.5 *long and approx.* 0.7 *nm of diameter. (B) Space distributions of L4P cylinders in a PS layer.*

Supposing the absence of any aggregates previous spin-coating, it's possible to calculate the total number of molecules present and, their average distance for the 20 wt.% concentration, in this case approx. 1.5 nm. The latter number is

valid for all directions: when a molecule lies directly at the ZnO/PS interface, another can lie above it, in proximity of the PS/air interface. But when a molecule is situated further from the ZnO, than there is no space to fit a second acceptor in the vertical direction (Fig. 25B).
Collecting emission from a large spot, contribution from in-contact and further molecules will be averaged. The resulting mean distance of L4P will not be at the hybrid interface but in the proximity of the polymeric layer centre. Only molecules directly in contact will be influenced by the energy transfer, and only a fraction of those will have the right orientation to enable the transfer of energy.
Upon these considerations, the limited number of molecules eligible for energy transfer, both for distance and for orientation reasons, corresponds to a an effective lower absorption cross section and to a limited value of the orientation factor k^2 in the transfer rate (k_{ET}^F) definition (Eq. 14).
Although is impossible to measure that exact fraction of molecules actually eligible for energy transfer, both these effects can justify the low measured transfer efficiency.

This chapter presented ET measurements between L4P and a ZnO SQW. L4P was dispersed into a solid PS matrix to obtain homogeneous thin films spincasted from a solution. The highest efficiency measured was $\eta_{ET} \approx 50\%$ within a transfer time of 230 ps. Above results can be attributed to the matrix effectively "diluting" the molecules: with a 20 wt.% concentration, the minimal L4P-L4P distance can be estimated to approx. 1.5 nm. With such a distance (Fig.25B) the average distribution of molecules directly on the ZnO surface, and thus sensitizable by the energy transfer are limited. L4P must be chemically modified or substitute with a similar molecule that enables a better sample design.
The present work is a proof-of-concept study: electronic coupling of ZnO and L4P excitons is principally demonstrated but the sample geometry must be improved.

Another important push-back for L4P lies in its least photo-stability: L4P solutions exposed to UV excitation under ambient condition change their absorption spectrum. This can be directly observed in L4P solutions: after UV illumination, the pristine transparent liquid turns yellowish as shown in Fig. 26.

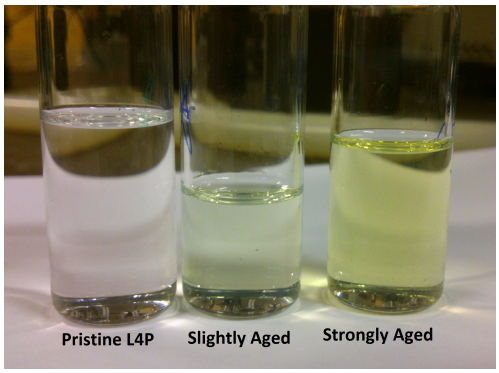

Figure 26: *Colour change of L4P solutions after different exposure time to UV light. The three cuvettes contain the same L4P solution* (10^{-4} *M) in Tetrahydrofuran (THF) and were exposed to* 10 *W/cm*^{2} *laser under ambient conditions. Slightly and strongly aged correspond to* 15 *and* 30 *minutes of laser exposure respectively.*

The same effect was also observed for L4P thin films. These changes are crucial for ET measurements, as they effect directly the overlap integral and thus the transfer rate (Eq.14).

4.6 POLYFLUORENES DEGRADATION: L4P CASE

For polyfluorenes, several studies commonly attribute the degradation reaction to oxygen species, with a consequent formation of fluorenone-type defects.[84–87] These model is generally accepted, and it supposes the cheto-defect to act as energy traps with a subsequent green-to-yellow light emission at rather low efficiency.[78,86,88]
All experimental data presented here after consistently demonstrate that the green emission observed for thin films, is the same photo chemically generated defect observed in solutions. By working with defined intermolecular distances, efficient ET between L4P and L4P-deg was demonstrated.
Although initial spectroscopic studies suggest the same to hold true for LOPPs, kinetic studies of the degradation process are not compatible with the established mechanism. A deeper and more complete study on the L4P degradation can be found elsewhere.[1] Further experiments about the L4P degradation must be performed to understand how the aging effects the measured transfer rate.

Sample Preparation

While photo-degradation kinetics of L4P are more conveniently studied in dilute solutions, interactions between L4P and L4P-deg are better studied in thin films with arbitrary molecular concentration. Films studies are also basilar for electronic and optoelectronic applications, since all devices must be in solid phase.
Pristine layers with notably different average intermolecular distances were investigated: three 100 nm thick films (A, B, and C) with increasing L4P concentrations (1, 10, and 20 wt.%) were spincasted on sapphire substrates. Assuming a homogeneous distribution of molecules in the matrix, the associated average intermolecular distances decrease from 4 nm over 2 nm and 1.5 nm for samples A, B, and C, respectively.

1,4-diazabicyclo[2.2.2]octane (DABCO)[89] was added to the L4P/PS layer B to understand the role of singlet oxygen in the photo-degradation. Integrated emission spectra with and without DABCO are reported in Fig. 27.

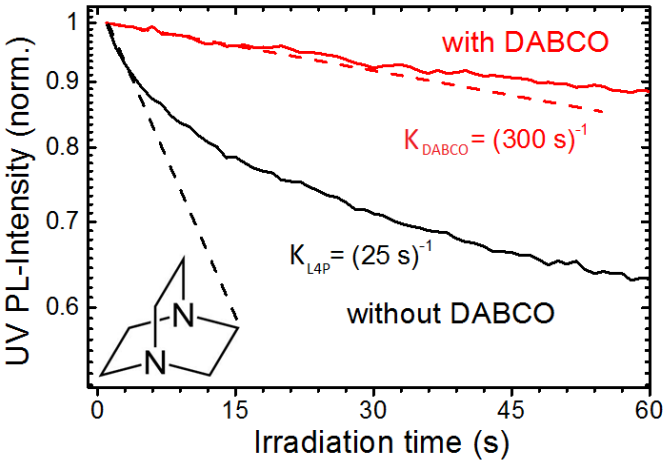

Figure 27: *Influence of singlet oxygen quencher DABCO on the aging rate. Black line: Integrated PL intensity of the L4P 0-0 transition over time under constant UV illumination for a 100 nm 10 wt.% L4P/PS layer. Red line: Integrated PL intensity for an equivalent layer in the presence of the same wt.% of DABCO as L4P. The chemical structure of DABCO is shown in the graph. Aging was performed with a Ti:Sapphire laser (E_{exc}=3.5 eV) under vacuum conditions (10^{-4} mbar) and an excitation density of 35 W/cm^2.*

Addition of DABCO thus results in a considerably slowing down of the degradation.[1] The time window was chosen to be 60 seconds in agreements with standard acquisition time for PL time resolved measurements. Approximating the first part of the two curves into straight lines (dashed black and red lines) is possible to extrapolate a rate of aging for the two samples. Values (K_{DABCO}=(300 s)$^{-1}$, K_{L4P}=(25 s)$^{-1}$) evidence the one order of magnitude (in time) increase of the stability caused by DABCO.

Fig. 28A shows PL spectra of the pristine films normalized on the 0-0 transition. These are rather similar to the PL spectra in solution.[36] However, the high L4P concentration results in reabsorption of the PL above 3.25 eV, hence the 0-1 transition dominates the emission spectra. Notably, a spectrally broad, blue-green emission becomes prominent at increasing concentration.

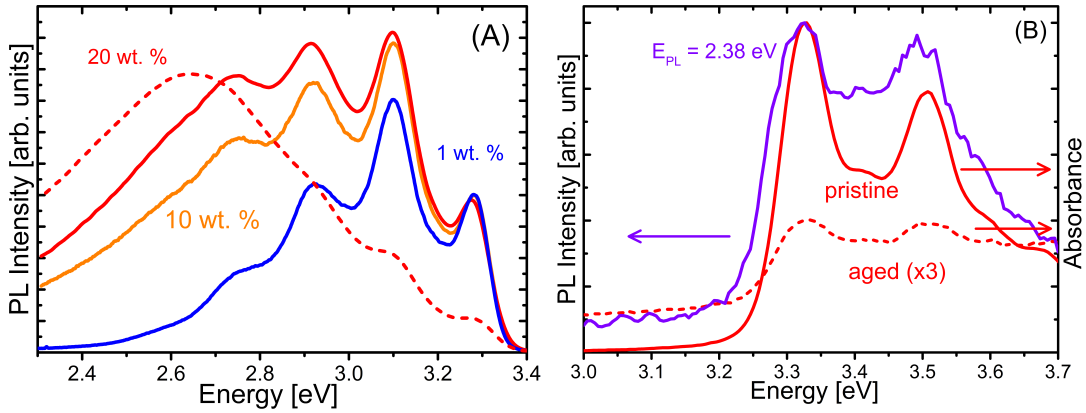

Figure 28: *Energy transfer from L4P to defects in L4P/PS layers on sapphire. (A) PL spectra of* 100 *nm thick pristine films with increasing amount of L4P:* 1 *wt.% (blue),* 10 *wt.% (orange), and* 20 *wt.% (red, solid). Spectra are normalized to the* 0-0 *transition. PL spectrum of the* 20 *wt.% sample after partial photo-degradation (red, dash-dotted). (B) Absorbance spectra of a pristine (solid, red) and a strongly photo-aged film (dash-dotted, red, enlarged by a factor of* 3 *for better visibility). PLE spectrum corresponding to the defect emission of a partially photo-aged film (solid, purple;* E_{det}*=2.38 eV) all samples are acquire on the* 20 *wt.% sample. "Partial" and "strong" aging denotes Ti:Sapphire laser irradiation (*E_{exc}*=3.5 nm) under ambient conditions for* 15 *min at* 5 *W/cm*^{2} *and* 30 *min at* 50 *W/cm*^{2}*, respectively.*

Laser irradiation of L4P/PS layers leads to a severe reduction of the UV emission and an increase of the blue-green PL component as illustrated exemplary for a photo-degraded layer with 20 wt.% L4P (red dash-dotted line in Fig. 28). The increase observed in the low-energy emission upon photo-degradation makes it unlikely to originate from aggregates. Because of the beneficial effect of DABCO showed before, the photo-oxidation process was assigned to be at least partially singlet-oxygen based. These conclusions are substantiated by studying the absorption of the layers (Fig. 28B). While the absorption of the pristine layer is that of L4P, the irradiated film exhibits a reduced and nearly featureless spectrum, which extends to energies below the L4P absorption onset at 3.25 eV. Again, this behaviour closely resembles that in solution: there, direct excitation of photo-created defects via the low-energy absorption tail is demonstrated (see Fig. 28B), leading to the exclusion of excimers as the main source of the blue-green PL.

PLE and time-resolved PL spectroscopy are used to prove Förster-type energy transfer takes place from L4P to the L4P-deg defects. With PLE, the defect emission at E_{PL}=2.38 eV of a partially aged layer of type C is monitored as a function of excitation energy. The resulting spectrum (Fig. 28, purple curve) is an envelope to the absorption spectra of the defects and of L4P, demonstrating that the defects can be excited either directly or indirectly via the L4P.

Dynamic of ET between L4P and L4P-deg was elucidated by time resolved PL. The decay of the L4P emission in layer C (Fig. 29A, red line) is markedly non-exponential and much faster than in layer A (Fig. 29A, blue line). Thus, an additional decay channel with a time-dependent decay rate has to be present here. Concerning the acceptor dynamics, a rise time is clearly observed in layer C (Fig. 29B, red line) but not in layer A (blue line). This proves the existence of a feeding process to the defect population in the first case.

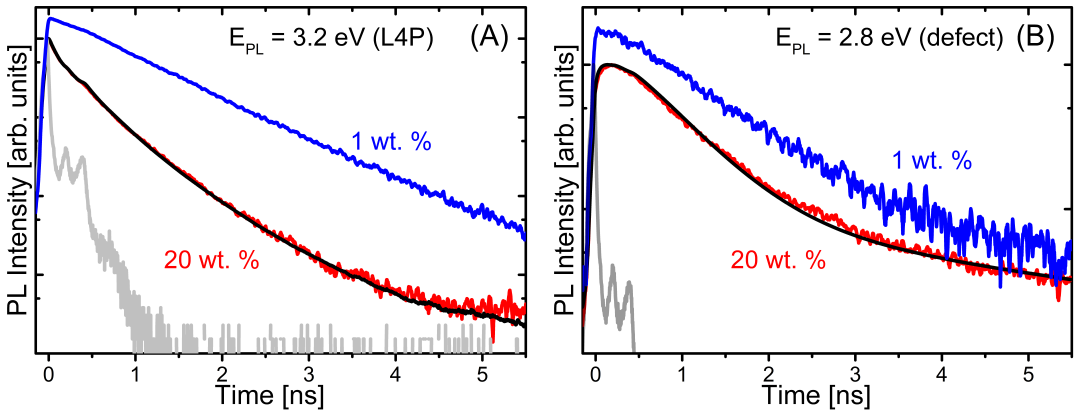

Figure 29: *PL decay of pristine films containing either* 1 *wt.% (blue, shifted for clarity) or* 20 *wt.% (red) of L4P. (A) PL of L4P (E_{PL}=3.28) and (B) defect PL (E_{PL}=2.38eV). Black curves are fitting results using a Förster type energy transfer model (for details, see text) convoluted with the instrument response function (IRF, grey lines).*

A Förster-type model that takes into account energy transfer from L4P donors to statistically distributed defect acceptors is readily employed to describe the dynamics in layer C. Accordingly, the number of excited donors N_D and acceptors N_A follow the rate equations:

$$\begin{aligned} \dot{N}_D &= -k_D N_D - k_T(t) N_D \\ \dot{N}_A &= -k_A N_A + k_T(t) N_D \end{aligned} \tag{33}$$

Herein, k_D and k_A are the intrinsic donor and acceptor decay rates, respectively, and $k_T(t)$=$\beta 2\sqrt{k_D/t}$ is the time-dependent energy transfer rate where the prefatory β is proportional to the number of unexcited acceptors of density ρ_A within a spherical volume V of Förster radius R_0. With the initial conditions:

$$\begin{aligned} N_D(0) &= N_{D,0} \\ N_A(0) &= N_{A,0} \end{aligned} \tag{34}$$

for a δ-like excitation pulse, the solutions to Eq. 33 are given by

$$\begin{aligned} N_D(t) &= N_{D,0} \exp^{-k_D t} \exp^{-\beta\sqrt{k_D t}} \\ N_A(t) &= N_{A,0} n_A(t) + (k_T N_D * n_A)(t) \end{aligned} \tag{35}$$

with $*$ being the convolution operator. The acceptor population $N_A(t)$ includes both direct excitation $n_A(t)$=$\exp^{-k_A t}$ and excitation via energy transfer $k_T \neq 0$. The model functions Eq. 35 are convoluted by the system's instrument response function (IRF) (Fig. 29A and B, grey curves) before fitting. As indicated by the black lines both the donor and acceptor decay curves are consistently described by one set of fitting parameters, namely k_D=(1.52 nm)$^{-1}$, β=3.82, k_A=(0.56 ns)$^{-1}$, α=$N_{A,0}/N_{D,0}$=0.12. Efficient energy transfer is evidenced by $\beta > 2$ which implies that $k_T(t) > k_D$ up to $t > k_D^{-1}$, that is, energy transfer dominates the total donor decay up to times that are larger than the intrinsic decay time.

Being aware of the limitations for such a model, as the assumed single exponential intrinsic donor and acceptor decays or the neglect of energy diffusion between donors, the obtained fitting parameters are not discussed in further detail. Finally, it is remarked that the observation of energy transfer from L4P molecules to photochemically created defects is not restricted to solid films, but equally applies to highly concentrated solutions as already predicted in other studies.[84]

It was shown that ladder-type L4P dispersed in solution as well as in a solid matrix degrade upon UV irradiation. The major source for such decomposition was attributed to singlet oxygen, as the addiction of a DABCO, a singlet-oxygen quencher, significantly slows down the degradation speed.
It was also proven that the photo-degradation mechanism commonly proposed in literature is not valid for L4P, as specifically synthesized structures such as L4P-O and L4P-O2 exhibit different optical properties of a photo-degraded solution.
Based UPLC-MS analysis, it was deduced that upon UV irradiation of L4P a formylation reaction occurs, that gives rise to various green-yellow emitting mono-formylated regioisomers denoted as L4P-deg.[1] The possible phtochemical reaction is reported in Fig. 30.

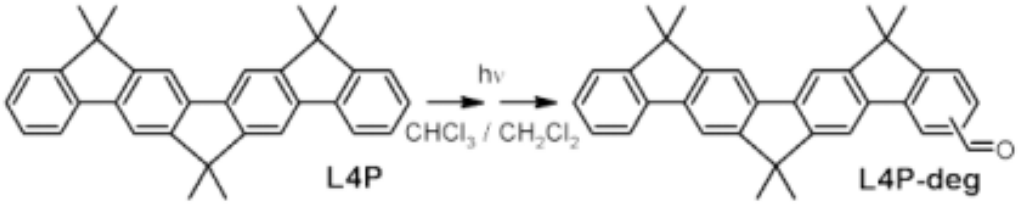

Figure 30: *Photochemical degradation of L4P in Chloroform (labelled as L4P-deg) identified by mass spectroscopy methods. For more information see*[1] .

It was also proven that for sufficiently small intermolecular distances, as the case of a few nanometers thick polymer/L4P layers, the L4P-deg species are efficiently excited via energy transfer from the pristine L4P.

4.8 SPIRO-MODIFIED LOPPS

Taking over from previous results, L4P was chemically modified to improve its stability without losing its optical peculiarities. One way to affect the sensitivity towards degradation is the substitution pattern. It was shown for polyfluorenes, as well as for LPPPs, that aromatic bridge substitution gives the most inert structures.[33,34] In the case of LPPPs the most common motif for aromatic bridge substituents is the spirobifluorene.[32]
Since aromatic substitution leads to enhanced photochemical stability molecules with subsequent increments of the spiro groups number were synthesized. Introduction of spirobifluorene units may affect the thin film morphology, since spiro-groups presence should modify the intermolecular interaction. Thus solid state packing and film-forming properties can thus be adjusted. Some spiro-modified L4P derivatives are shown in Fig. 31. Upon adding more spirobifluorene moieties in the bridges of L4P, the optical properties do not change dramatically. The spectra of L4P, L4P-SP2, and L4P-SP3 exhibit nearly the same shape with two main maxima due to vibronic progression in the absorption and emission. The Stokes-shift is small (around 40 meV) and the fluorescence quantum yield of all only-hydrocarbon derivatives is close to unity. However, with every additional spiro unit, absorption and emission are shifted bathochromically by about 2 nm.

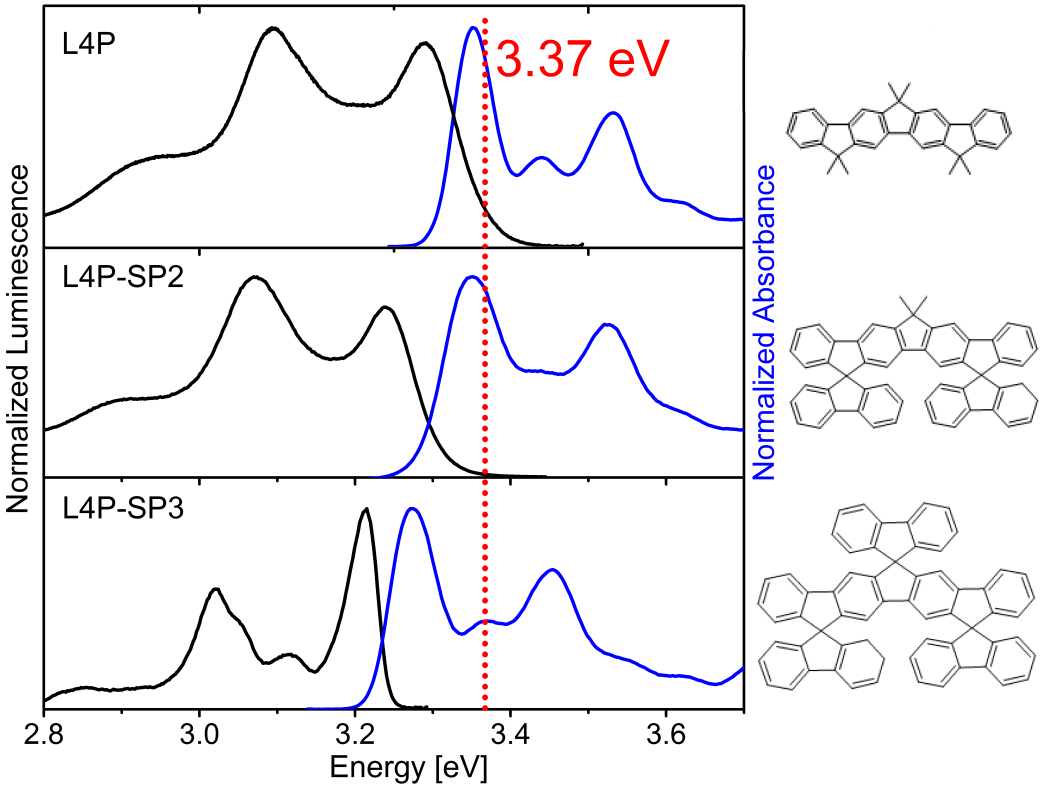

Figure 31: *Optical and structural properties of different LOPPs molecules. Top panel: L4P/PS layer absorption and emission spectra. Second panel: L4P-SP2 4 nm evaporated layer spectra, the chemical structure is shown left to the graph, the inset AFM picture show the 2D structure of the layer. Third panel: Spectra for a 4 nm L4P-SP3 layer, chemical structure of the molecule is also present. Bottom panel: iso-L4P-SP2 spectra,and its chemical structure, this molecules will be discussed in the conclusion chapter. Solid lines, ZnO emission position at LT (red dotted line) and at RT (blue dotted line). Spectra were acquire upon excitation at 4.2 eV by a Xenon lamp.*

L4P-SP2 was successfully used for strong coupling with ZnO:[90] the double spiro modification increase the photo-stability of the molecules but AFM pictures of OMBD samples still show the undesired 2D structure when grown on sapphire (picture not shown).
L4P-SP3 is the molecule selected for further energy transfer experiments. Despite having slightly red-shifted energies, it possesses the best spectral overlap with the RT ZnO emission (3.3 eV, blue dotted line Fig. 31) and shows the best photo-stability.
Fig. 32 compares the degradation for L4P, L4P-SP2 and L4P-SP3 molecular layers under comparable excitation conditions.

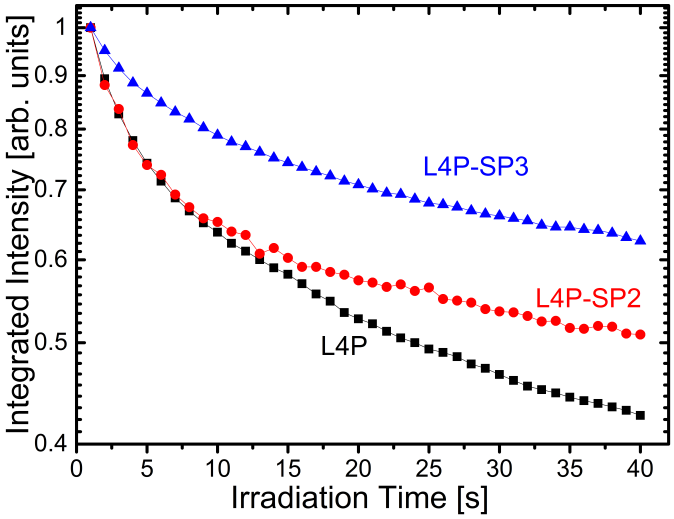

Figure 32: *Photo-stability of Spiro derivatives: integrated emission of L4P/PS 3 nm spincasted layer (black squares), 3 nm L4P-SP2 (red dots) and L4P-SP3 (blue triangles) OMBD layers respectively. All layers are grown on sapphire. Consecutive PL spectra were acquired under the same ambient conditions with an excitation of approx. 30 W/cm^2 with E_{exc}=3.5 eV. The integration was performed only on the first vibronic line of the emission spectrum to exclude the green-emission formation that accompany L4P degradation.*

L4P (black squares) is the fastest specie to decompose under UV light, as its emission halves in 30 s. L4P-SP2 (red dots) initially degrades at the same speed of L4P, but the degradation slows for longer times. L4P-SP3 (blue triangles), upon air and UV light exposure loses only 1/3 of the initial intensity within the first 30 s, which is the standard measurements time.

AUTHOR'S CONTRIBUTION

Heterostructures presented here are prepared by Dr. Sergey Sadovief who is responsible for the MBE apparatus.

Organic compounds were provided by Dr. Björn Kobin from the Prof. Stefan Hecht laboratories.

Spin-coating of thin films, optical characterizations and data evaluations were performed by the author. Time-transient deconvolution and fitting were performed by the author using a Matlab software provided by Dr. Sylke Blumstengel.

Dr. Björn Kobin performed L4P degradation studies for the solution phase, while the solid state measurements were performed by the author. Dr. Simon Halm provided the initial L4P-L4P-deg ET model as well as the Mathematica software for the fitting curves.

5

ENERGY TRANSFER IN ZNO/L4P-SP3 HYBRID STRUCTURES

The following pages present energy transfer experiments between a ZnO SQW and a blue emitting overlayer of triple-spiro substituted ladder-type oligo(p-phenylene) (L4P-SP3). Results shown in this chapter are published in.[2,3]

5.1 MOTIVATION

The possibility of vacuum deposition in combination with the relatively high quantum yield in solid state (approx. 50%), make L4P-SP3 an excellent candidate for inorganic/organic hybrid structures. Due to its rigid backbone, L4P-SP3 exhibits a distinct vibronic progression with the dominant $S_{0,=0}$-$S_{1,=0}$ transition practically in resonance with the room temperature photoluminescence band of the QW (grey area Fig. 33).

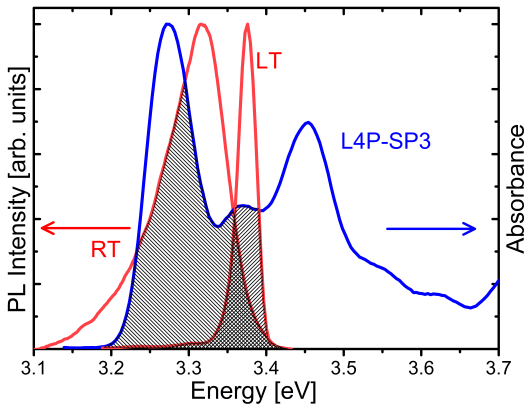

Figure 33: *Spectral overlap between a* 3.5 *nm ZnO QW emission measured at low and room temperature (red lines) and the absorption spectrum of L4P-SP3 deposited on sapphire (blue line). All spectra are normalized.*

Unlike measurements presented in the previous chapter, here a thin amorphous layer guarantees a distribution of molecular dipoles directly in contact with the ZnO surface.

Energy transfer in L4P-SP3/ZnO HIOS samples is evaluated applying the same set of measurements as the previous chapter (Ch.4). To disentangle different interaction and to focus only on the energy transfer, all experiments are performed at cryogenic temperature. Luminescence and time resolved measurements were carried upon laser excitation with photon energy E_{exc}=3.46 eV and a nominal excitation density of I_{exc}=5 W/cm^2.

5.2.1 *L4P-SP3 Layer Preparation and Characterization*

Molecular layers were grown by OMBD at a base pressure of 10^{-8} mbar on ZnO/ZnMgO heterostructures. The growth rate of the organic layers was monitored by a quartz microbalance. Layers shown in this chapter were prepared with a deposition rate of 0.3 nm/min.
Pristine L4P-SP3 layers were studied by atomic force microscopy (AFM) and X-Ray-Reflectometry (XRR)[91] to ensure the amorphous 2D growth. A representative AFM image is depicted in Fig. 34.

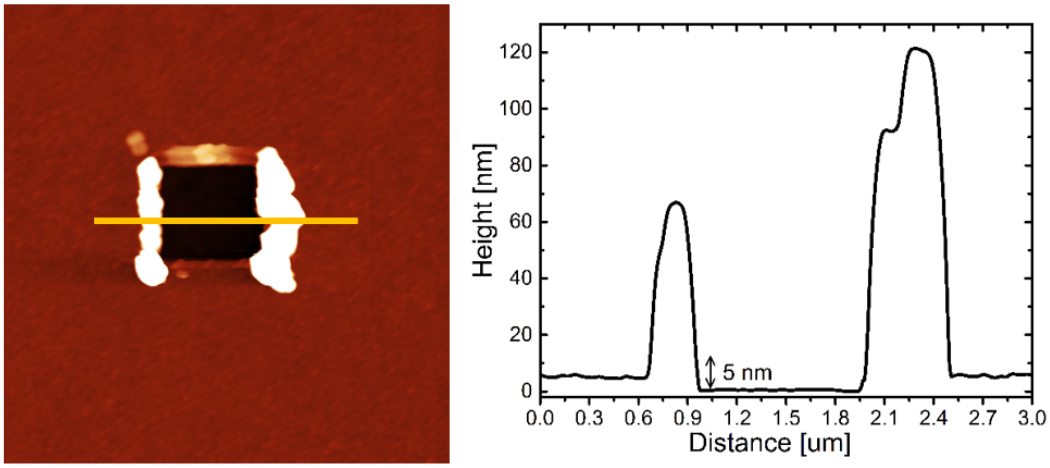

Figure 34: *AFM picture of a approx. 5 nm layer of L4P-SP3 grown on ZnO substrate. The height of the layer was deduced by scratching a portion of the sample (1μx1μm) using the AFM in contact mode.*

When deposited at room temperature on the Oxygen terminated (000-1) ZnO surface, L4P-SP3 displays a two-dimensional Frank-van der Merwe growth. The film thickness was measured by AFM in contact mode and applying sufficient force to break up the film.

The layer structure was evaluated by XRR measurements on a 20 nm thick film of L4P-SP3, the resulting curve is shown in Fig 35.

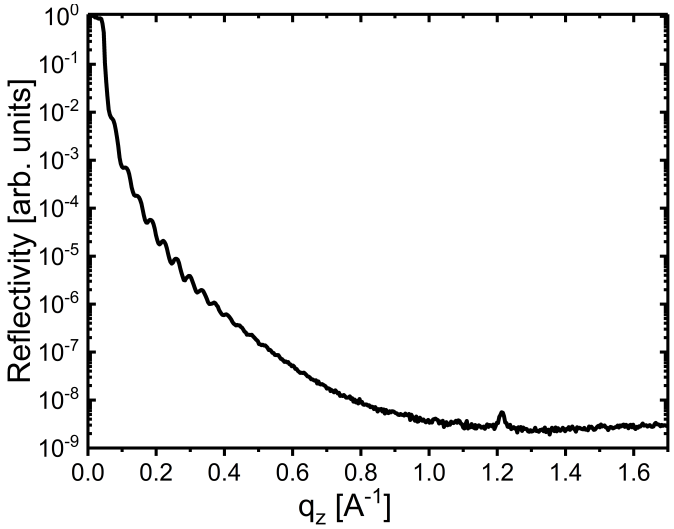

Figure 35: *XRR spectrum of L4P-SP3 during growth. The Kiessig oscillations at low q_z confirm a smooth film morphology. The Bragg peak at q_z=1.21 A^{-1} can be attributed to parasitic radiation from ZnO.*

The large number of pronounced Kiessig oscillations at low q_z values confirm a smooth film morphology. From the number of oscillations the film thickness can be determined to 19.6 nm, in agreement with the targeted 20 nm. The only Bragg peak at q_z=1.21 A^{-1} corresponds to a lattice constant of 5.19 Å and can be attributed to parasitic high energy radiation from ZnO.

5.2.2 *All-UHV Handling*

Fig. 36 (A,B and C) shows the structural evolution of three 3 nm thick layers deposited on identical ZnO substrates. When exposed to air, the L4P-SP3 films dewett in hours.

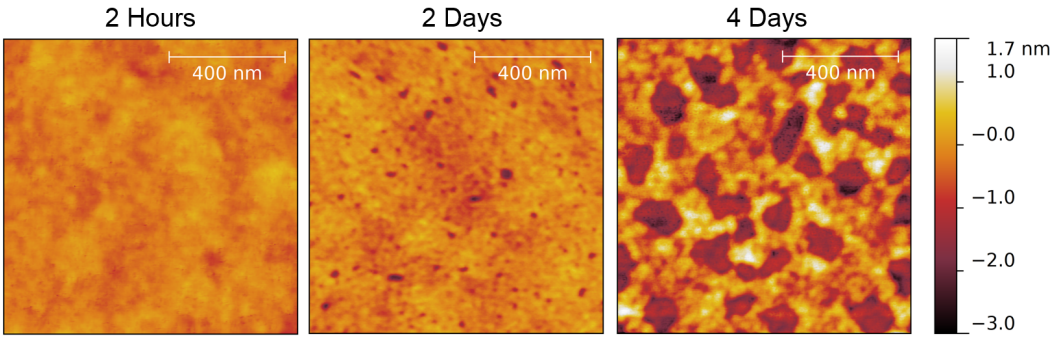

Figure 36: *Dewetting of L4P-SP3 thin films. (A) AFM picture measured in-situ 2 hours after deposition and storage in UHV. (B) AFM recorded ex-situ after exposure to air for 2 days. (C) AFM recorded ex-situ after exposure to air for 4 days. All films were grown at 300 K with a deposition rate of 0.3 nm/min*

However, no changes in the film morphology were observed when keeping the samples under vacuum or nitrogen atmosphere. For that reason, all hybrid samples were prepared and stored always in UHV or nitrogen-only (glove-box) atmosphere.

5.2.3 *Sample Structure*

The sample studied here is a 3.5 nm ZnO SQW embedded in a ZnMgO barrier with a Mg content of 11%. Details on the ZnO epitaxy can be found elsewhere.[30] By using a shadow mask during growth, the sample is divided into two areas: a half of the surface is left for reference measurements and the other half of the surface is covered with 4 nm of L4P-SP3 and by 15 nm of C40, a schematic drawn of the sample was depicted in in Fig.13 in Ch.3. The L4P-SP3 lifetime derived from the PL decay transients with the tetracontane spacer is τ_m=500 ps and agrees well with data for thick films on sapphire (data not shown).

5.3.1 *Energy Transfer Measurements*

PL spectra for the hybrid sample and for the pristine QW are reported in Fig. 37A. Both sides of the sample exhibit bright QW emission at 3.37 eV. PL spectra of the hybrid sample (black curve Fig. 37A) shows a barely detectable emission from the molecules, clearly visible only after a 20 times magnification. The quantum yield of L4P-SP3 is sufficiently high in solid state and cannot serve as explanation. Consequently, there has to be an efficient pathway for the loss of excitation energy at the ZnMgO/L4P-SP3 interface. This deposition design allows to directly compare inorganic and hybrid QW emission. In this case, the QW emission decreases after introducing the molecular overlayer, suggesting that a part of the ZnO excitons are transferred to the molecules.

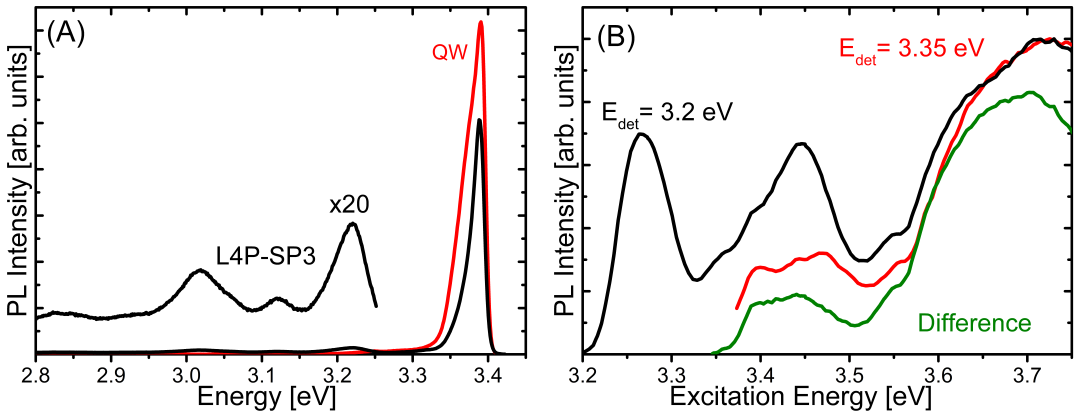

Figure 37: *Energy transfer in L4P-SP3/ZnO hybrid structures: (A) PL spectrum of the hybrid sample, luminescence generated by the L4P-SP3 is magnified by* 20 *times for better visibility. In these spectra* E_{exc}=3.46 *eV. (B) PLE spectra for the hybrid structure: spectrum detected on the ZnO emission* (E_{det}=3.35 *eV, red line) and spectrum detected on the L4P-SP3 emission in the hybrid sample* (E_{det}=3.2 *eV, black line). The green curve is the result of subtracting the blue curve from the black curve.*

PLE spectroscopy measurements support the excitonic transfer. Fig. 37 shows normalized excitation spectra recorded at low temperature. The excitation curve measured on the QW emission (E_{det}=3.352 eV, red curve) displays the exciton ground and excited-state absorption features, at 3.4 and 3.45 eV respectively, and the ZnMgO band edge ($E_{exc} > 3.55$ eV). Feeding of the barrier in the QW absorption indicates efficient capture of carriers by the QW. Detecting on the light emitted by the molecules (E_{det}=3.12 eV, black curve), the 0-0 and 0-1 transitions of the L4P-SP3 are visible at 3.27 and 3.45 eV, respectively. In addition to that, the ZnMgO absorption edge is visible for higher excitation energies, demonstrating unambiguously the exciton transfer from the ZnO QW to the L4P-SP3 layer.

The transfer time and the transfer efficiency are extracted from time-resolved spectroscopy. Focusing on the QW dynamics, decay transients are shown in Fig. 38. In absence of the L4P-SP3 layer, the QW decays is in good approximation single-exponentially with a time constant of τ_{QW}=200 ps (red curve). When in contact with L4P-SP3, the QW decay time shortens to τ_{QW}^{H}=56 ps (blue curve).

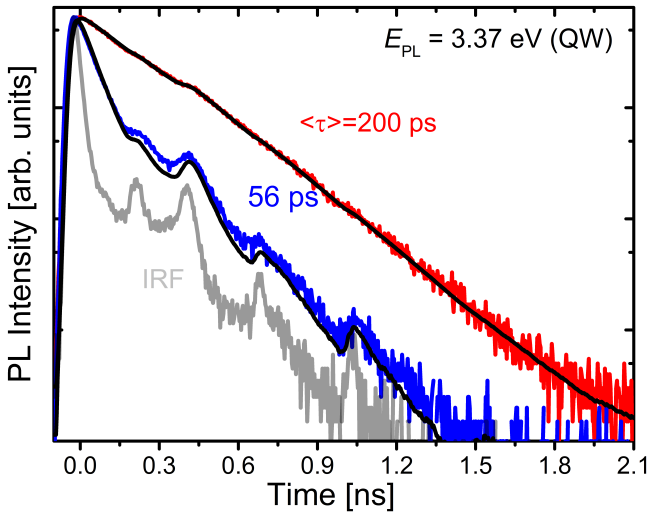

Figure 38: *Energy transfer in a L4P-SP3/ZnO/ZnMgO HIOS: PL transients of the ZnO QW in the uncapped (red curve) and hybrid part (blue curve) of the HIOS. Black solid lines are fits to the data obtained by convolution of a single-exponential decay law with the system response function (IRF) shown in grey. For these measurements, T=4 K, E_{exc}=3.46 eV and the excitation density was I_{exc}=5 W/cm^2.*

Quenching of the QW lifetime confirms the presence of an additional non-radiative decay channel. The system can be described using the same model used previously (Eq. 27). The corresponding transfer rate, τ_{ET}, and η_{ET} obtained with formulas (Eq. 31 and Eq. 32) are 77 ps and 72% respectively. Thus, about three out of four excitons photo-generated in the QW are transferred to the organic overlayer.

Another efficient strategy to prove the ET mechanism between the QW and L4P-SP3 is obtainable by exciting the sample above the ZnMgO band edge. Fig. 39 shows the PL transient for the ZnMgO barrier, the ZnO QW and the L4P-SP3 overlayer respectively.

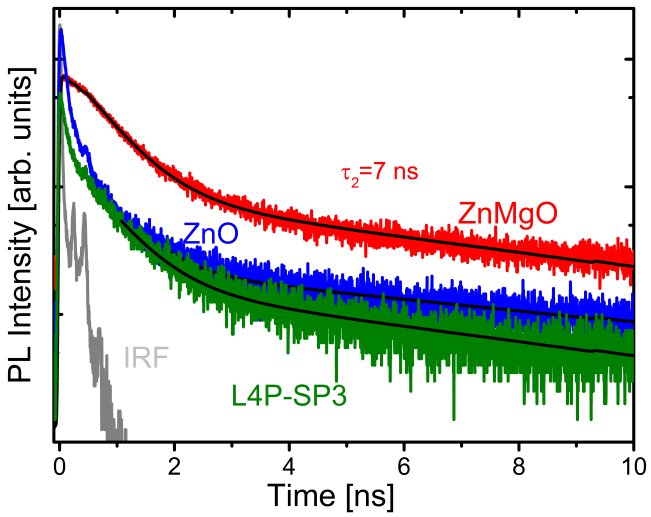

Figure 39: *L4P-SP3/ZnO Above ZnMgO barrier excitation: time trace for the ZnMgO (E_{det}=3. eV, red line), ZnO emission (E_{det}=3.37 eV, blue line) and L4P-SP3 (E_{det}=3.22 eV, green line). All spectra were acquired at T=4 K with E_{exc}=3.55 eV and I_{exc}=5 W/cm^2.*

For this excitation energy, an exponential fitting show the long-life component of the ZnMgO barrier in both the QW and the molecular time transient. In all three cases, the long decay component can be fitted (solid black lines) with the same time constant $\tau_2 \approx 7$ ns.

$$\begin{aligned}
\dot{\eta}_{ZnMgO} &= g_{ZnMgO}(t) - \left(\frac{1}{\tau_{ZnMgO}} + \frac{1}{\tau_{ET}}\right)\eta_{ZnMgO} \\
\dot{\eta}_{QW} &= g_{QW}(t) - \left(\frac{1}{\tau_{QW}} + \frac{1}{\tau_{ET}}\right)\eta_{QW} \\
\dot{\eta}_{L4P-SP3} &= g_{L4P-SP3}(t) + \frac{1}{\tau_{ET}}\eta_{QW} - \frac{1}{\tau_{L4P-SP3}}\eta_{L4P-SP3}
\end{aligned} \tag{36}$$

These measurements can be considered another prove-of-concept experiment for the transfer mechanism, as the carrier feeding from the ZnMgO barrier can be observed for the L4P-SP3 time trace.

5.3.2 *Level Alignment at the Interface*

UPS measurements can give valuable insights regarding the least molecular luminescence shown before (Fig. 37A). A more detailed discussion about UPS/XPS measurements is can be found in a following chapter (Ch.7) and in.[92] Nevertheless, the energy level alignment is of type-II and is depicted in Fig. 40.

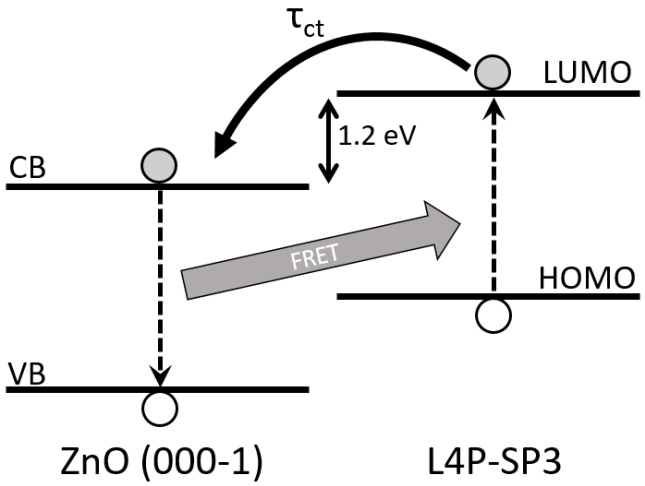

Figure 40: *Energy level diagrams for L4P-SP3 on the O-terminated ZnO(000-1). Back transfer of electrons from the L4P-SP3 to the ZnO QW. The energy offset between the CB and the LUMO is of 1.2 eV. Energy values are referenced to the Fermi level and in eV.*

The energy offset between the valence band maximum of ZnO and the L4P-SP3 HOMO deduced from the binding energy onsets amounts to 1.2 eV. Conduction band minimum and LUMO are estimated by adding the exciton binding energies (60 meV for ZnO and 450 meV for L4P-SP3[93]) to the optical band gaps (3.3 eV for ZnO and 3.25 eV for L4P-SP3) determined from the respective absorption spectra.
The Type II alignment, detrimental when targeting light-emitting applications, likely holds for many other conventional inorganic semiconductors as well.[23,29] Indeed, it was shown in previous work that the photoluminescence of a spirobifluorenene derivative is substantially quenched when in contact with ZnO due to interfacial exciton dissociation.[31]
In the above energy transfer study in L4P-SP3/ZnO hybrid structures, the ZnO QW collects the optically excited electron-hole pairs before they can reach the interface so that exciton coupling becomes predominant. Once the excitons are transferred to the organic layer, they are rapidly quenched due to charge separation at the ZnMgO/L4P-SP3 interface and thus the overall luminescence yield of HIOS is very low.

Time-resolved measurements on the L4P-SP3 emission fully confirms the charge separation process and is shown in Fig. 41.

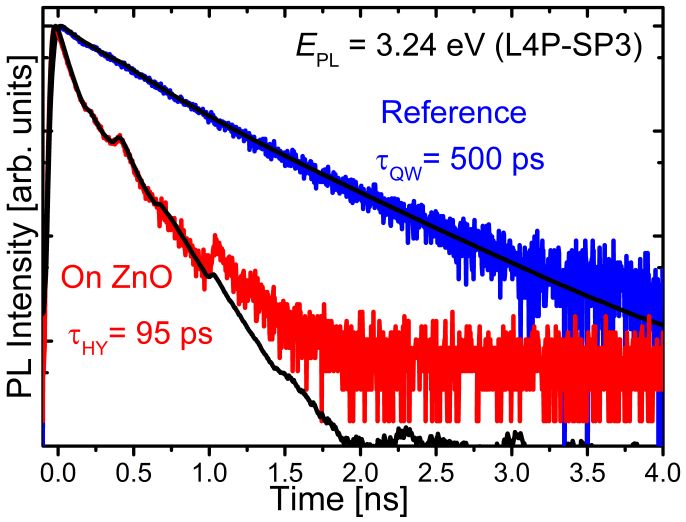

Figure 41: *Charge separation at the hybrid interface. L4P-SP3 time traces for a reference sample (blue curve, 20 nm film on Sapphire) and for the hybrid sample (red curve). The excitation energy is set below the absorption edge of ZnO at E_{exc}=3.35 eV. The Frenkel exciton decay is deduced from the experimental data by deconvolution with the system response. Solid black lines represent respective data fits.*

The molecular decay time for a reference layer is about τ_M=500 ps, but when deposited on ZnO, it shortens to τ_M^h=95 ps. The 95 ps overall decay can thus be taken as an upper limit for the characteristic time of the charge separation process defined as:

$$\tau_{CT} = \left(\frac{1}{\tau_m^H} - \frac{1}{\tau_m} \right)^{-1} \tag{37}$$

and:

$$\eta_{CT} = \frac{\tau_m^H}{\tau_{CT}} \tag{38}$$

the results are τ_{CT}=65 ps and η_{CT}=0.9 respectively. 9 out of 10 excitons generated (directly or indirectly) in L4P-SP3 are not converted into emitted light. This type of hybrid structure is thus unsuited for light-emitting applications. As a consequence, a large fraction of the excitation energy is not converted into light. To be of use in light-emitting applications, exciton dissociation at the hybrid interface must be prevented.

5.3.3 *Temperature Dependence*

The transfer mechanism was investigated from cryogenic up to room temperature. Fig. 42 reports decay time constants for pristine QW reference (black line and dots) and QW with overlayer (red line and dots) over a wide range of temperatures.
Decay times have been extracted after IRF deconvolution and single exponential fitting (curves not shown).

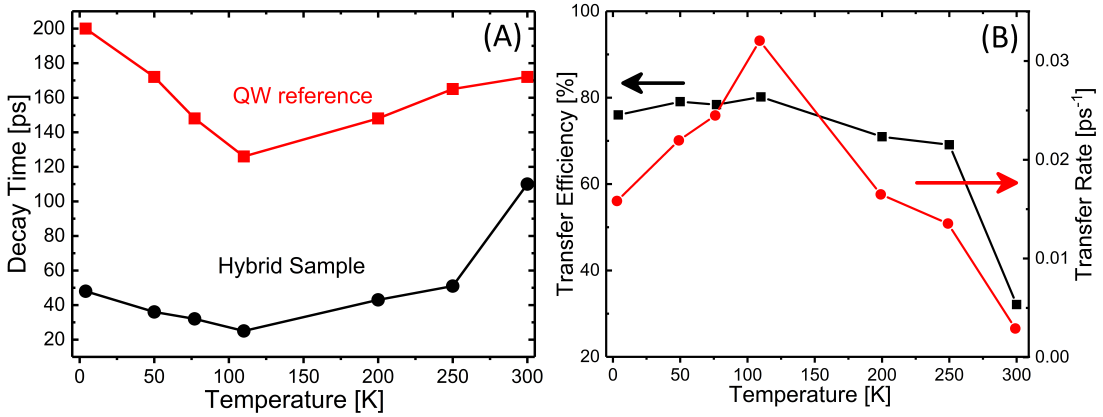

Figure 42: *(A) Photoluminescence decay time for the QW reference (red line) and with L4P-SP3 overlayer (black line) at different temperatures. The showed decay times are calculated according to the model described previously. In all cases* E_{exc}=3.46 *eV. (B) Transfer rates (red points) and efficiencies (black points) evaluated for the measured temperatures.*

Decay time of the QW in contact with L4P-SP3 is faster than in the reference sample for all measured temperatures suggesting the persistence of the ET mechanism. Using the equations previously discussed (Eq. 31, 32), ET rates $1/\tau_{ET}$ and efficiencies η_{ET} were extracted: results are reported in Fig. 42B.

τ_{ET} exhibits two regions of distinct behaviour. From 4 to 110 K, the rate slowly increases with temperature and, above that, it significantly decreases. The transfer time τ_{ET} measured of RT is approx. 340 ps. Directly correlated to τ_{ET}, the efficiency also shows two different phases as shown in Fig. 42B: between 4 to 110 K, η_{ET} can be considered constant as the slight increase from 76 to 82% is below the error bar for these measurements. At higher temperatures (T$>$ 110 K), η_{ET} decreases, setting at a value of 32% at RT. The highest measured efficiency corresponds to the transfer rate peak around 130 K. A similar thermal behaviour was already reported for several hybrid samples.
Between 50 and 110 K, the QW decay time for the hybrid sample τ^H_{QW} corresponds to the time resolution of the experimental setup (35 ps). In these cases, the real τ^H_{QW} are possibly shorter than values here reported, but the setup can't resolve it. Taking this into account, the η_{ET} extracted are an underestimation of the real values.

The system temperature can affect the energy transfer rate through:

- Possible variations of the spectral overlap between the QW emission and the molecular absorption.
- Variations of the QW transition dipole moments and thus radiative decay time (τ_{rad}).

These two steps are better treated separately.

Overlap Factor Changes

Spiro substitutions of L4P lead both to better photo-stability and amorphous grown but also to a significant red-shift of its optical properties. The latter shift has two main consequences: on one side, the LT overlap factor with the QW emission is limited (Fig. 33) but on the other side, the overlap factor will increase dramatically with rising temperature.
Recalling the definition for transfer time from previous chapter (Eq. 14):

$$k_{ET}^{F} = \frac{k^2 9c^4}{8\pi\tau_D n_0^4 R^6}\left(\int \frac{F_D(\omega)\sigma_A(\omega)}{\omega^4}d\omega\right) \tag{39}$$

the formula can be restructured supposing that most of the system constants are not affected by the temperature increases, leading to:

$$\frac{1}{\tau_{ET}^{F}} = \alpha \int \frac{F_D(\omega)\sigma_A(\omega)}{\omega^4}d\omega$$

where α collects all the above constant. The factors $F_D(\omega)$ and $\sigma_A(\omega)$ can be experimentally measured (curves not shown). The temperature behaviour of τ_{ET} can be roughly estimated by the changes of the overlap integral as a function of temperature. Integrals for the curves overlap, normalized on the 4 K value, are reported in Fig. 43A,B.

The overlap integral increases 3.5 times respect to the 4 K value. This result is in clear contradiction with the behaviour of transfer efficiencies previously evaluated, and thus cannot justify those results (Fig. 42).

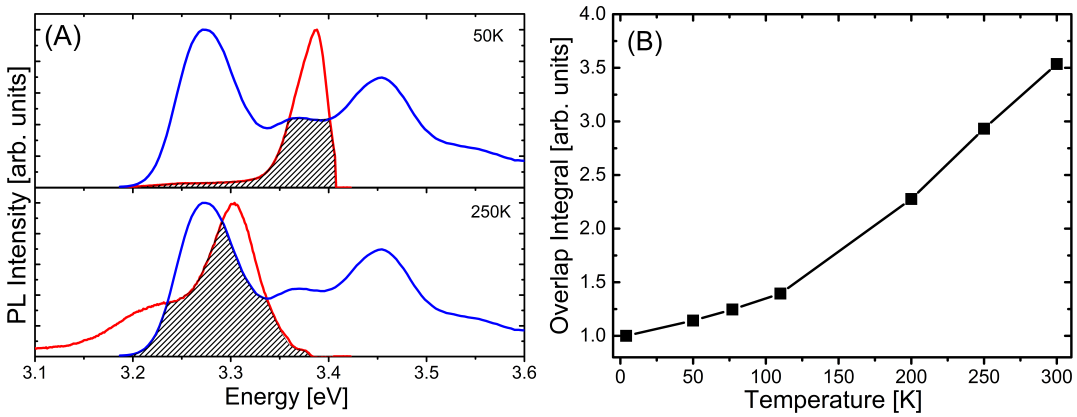

Figure 43: *Change of the spectral overlap: (A) Overlap spectrum between the QW emission at 5 K (top graph) and at 250 K (bottom graph) and L4P-SP3 absorption measured on sapphire (blue line). (B) Integrated overlap curve for several temperatures, all values were normalized on the 4 K result.*

QW Excitonic Properties

Energy transfer results from a direct coupling between the two different classes of excitons, and it's therefore sensitive to variation in the excitonic properties of both species.
Förster's model[60] considers Frenkel excitons bound to individual molecules and is temperature independent. In contrast, for inorganic semiconductors the electronic excitations are propagating Wannier-Mott excitons. For QWs studied in this thesis, only one emission peak is observed at all temperatures. Nevertheless many effects are contributing to the steady luminescence signal. As pointed out in previous studies,[7,94–96] the radiative recombination in alloys is strongly temperature dependent: at low temperatures, excitons are localized at potential fluctuations, as they represents energetically lower state, while for increasing temperatures the excitons ionize from the impurities and become free. Measuring what type of exciton is steaming the luminescence is extremely important to understand the transfer rate previously described, as the different excitons (localized and free) will experience different coupling with the molecular excitons.
Fig. 44 reports a logarithmic/logarithmic plot for the QW external quantum efficiency from cryogenic to room temperature, the colored solid lines are fitting curves resulting from two models to describe the population of states for localized and free excitons respectively.

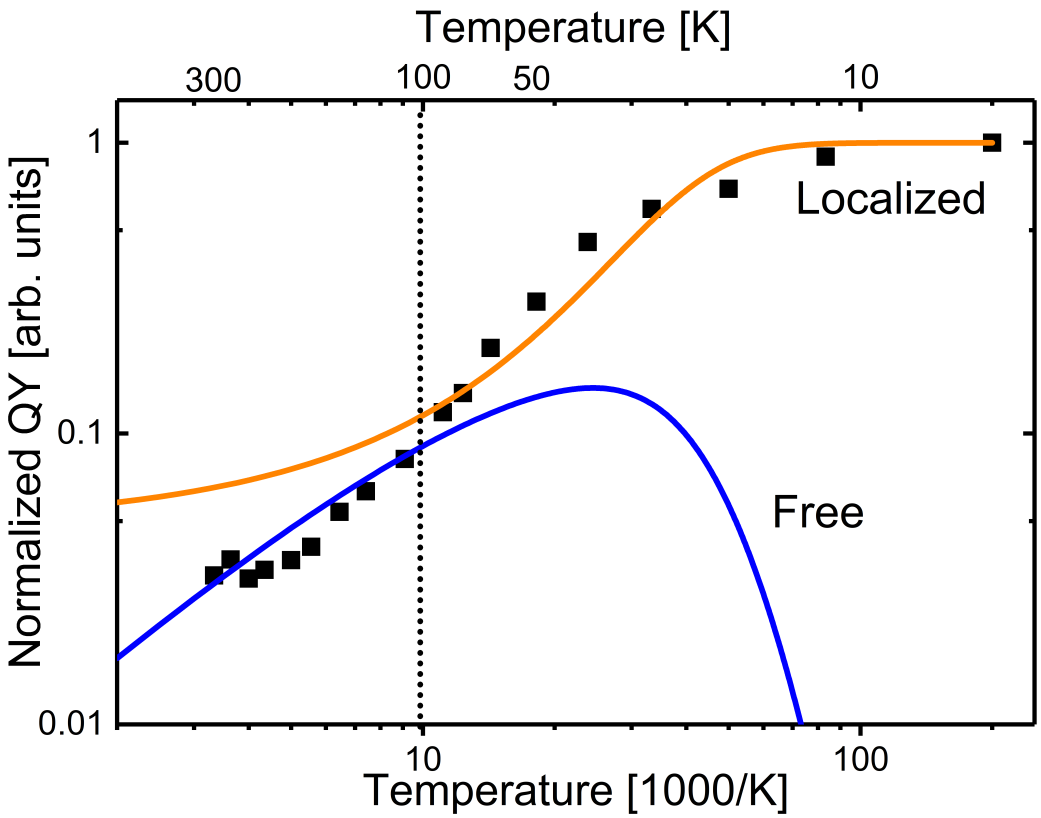

Figure 44: *Emission intensity from the ZnO QW: solid lines are obtained with Eq. 40 for the localized (orange) and Eq. 41 for the free excitons (blue) respectively. Note the logarithmic* 1000/*T-scale.*

Fig. 44 clarifies the balance between localized and free excitons at different temperatures. For temperatures below 110 K (dashed line), the QW luminescence is driven by localized excitons (orange line), in this case, initial increase of τ_{ET} can be attributed to the overlap factor increment discussed in the previous section. Above 110 K, free excitons dominate QW luminescence and thus the energy transfer.
Transfer rate decreases at higher temperatures (110-300 K) can thus be attributed to the free excitons wave vector enlarging, unable to efficient dipolar coupling. A similar behavior was already observed for AlGaN/GaN QWs based hybrid structures.[64,65]
The fitting function for localized excitons (orange curve Fig. 44) $I_{Loc}(T)$, according to[97–99] is:

$$I_{Loc}(T) = \left[1 + exp\left(-\frac{E_1}{K_B T}\right)\right]^{-1} \tag{40}$$

being C_1 the ratio of degeneracies of the involved level. The above formula supposes that the localized excitons start to delocalize with a single activation energy E_1.

The free exciton channel (blue line Fig. 44) is modeled as:[96]

$$I_{Free}(T) = (1 - I_{Loc}(T))\left[1 + \frac{\tau_{rad}}{\tau_{nrad}}\right]^{-1} \tag{41}$$

τ_{rad} and τ_{nrad} are the radiative and non-radiative free exciton lifetime respectively, both of them are found to increase with temperature. Thermally activated non-radiative recombination channels modify τ_{nr} as:

$$\tau_{nrad}(T) = \tau_{nr,0} * exp\left(-\frac{E_a}{K_B T}\right) \tag{42}$$

where E_a is the process activation energy. The above equation supposes that τ_{nrad} is initially constant at low temperature, as the temperature increases and excitons start to delocalize, τ_{nrad} starts to decrease as the now free excitons encounter more non-radiative channels.
The radiative QW rate τ_{rad} was also found to grow as T^m with $m > 1$.[96,100,101] One should note that due to momentum conservation, only excitons with small center-of-mass motion K-vector can recombine radiatively. This is typically accounted in the radiative lifetime, implicitly assuming that excitons from higher states scatter into the empty states after recombination. In this work, τ_{rad} is modeled as:

$$\tau_{rad}(T) = \tau_{rad,0}\left[1 + \left(\frac{T}{T_0}\right)^m\right] \tag{43}$$

with $\tau_{rad,0}$ the low temperature value, and T_0 and m chosen empirically to fit the data.[96,101] Temperature behaviour of the radiative decay time ($\tau_{rad}(T)$) can be extracted by optical spectroscopy using the formula:

$$\frac{\tau_{rad}(T)}{\tau_{rad}(4K)} = \frac{\tau_{QW}(T)}{\tau_{QW}(4K)} * \frac{\eta_{QW}(4K)}{\eta_{QW}(T)} \tag{44}$$

The latter equation correlates the temperature changes in the external well QY with the measured decay time τ_{QW}. Results are shown in Fig. 45.

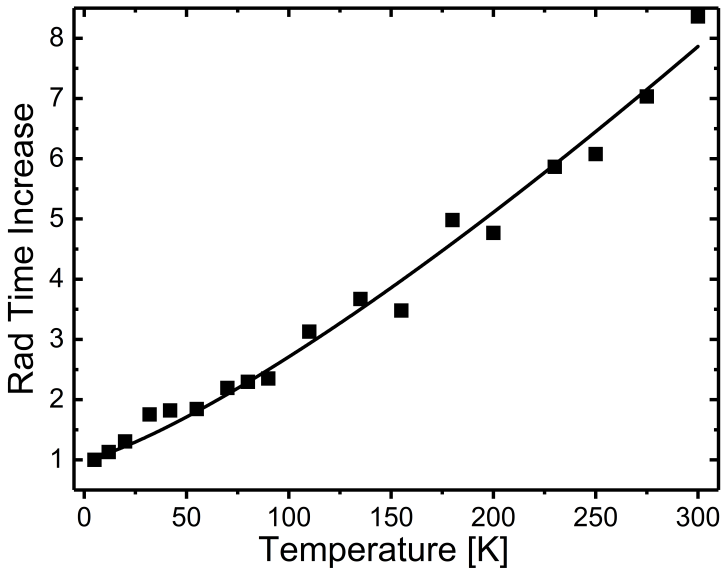

Figure 45: *Radiative time increase for a ZnO QW: the squares represent experimental data obtained from Eq. 44. The solid curve represents fit using Eq. 43, for such sample, the fitting parameters are* T_0=65 *ps and* m=1.24.

In the fitting curve, T_0 is found to be around 65 K and m takes a value of 1.24. It is worth mentioning here that a similar behaviour was obtained for several other samples with different cap thicknesses and Mg concentrations.
Finally, the fitting parameters can be given in details: Eq. 43 and 42 are substituted into the above formulas Eq. 41 and Eq. 40. A reasonably good fit for I_{Loc} is achieved using the parameters C_1=20 meV, E_1=10 meV. The I_{Free} function use the constants τ_{rad} of 200 ps and $\tau_{nr,0}$=7 ps and E_a=5 meV. The values of T_0 and m are obtained from the fit shown in Fig. 45.
All parameters have values of reasonable size. However, given the fairly unstructured dependence, these many parameters cannot be determined with great confidence. This thesis does not attempt to model in more detail the QW luminescence behavior, as the conversion from localized to free excitons was fairly demonstrated.
Finally, after observing the transition from localized to free excitons it is possible to explain the previous energy transfer results (Fig.). For temperatures between 4 and 110 K, the population of localized excitons decreases exponentially (Fig.) while their radiative decay time increases linearly (Fig.), these

two factors explain the initial increases of the transfer rate (Fig. B): excitons experience a higher mobility and a longer decay time, enhancing the changes of interactions with molecular excitons. Above 130K, free excitons start to dominate the ET, and the transfer rates (and efficiencies) start to decrease, as the wave-vector of free excitons becomes too large for efficient dipolar coupling.

5.4 CONCLUSIONS

In summary, this chapter studied resonance energy transfer from QW excitons to an overlayer of custom synthesized L4P-SP3. The newly triple-spiro-ladder-quaterphenyl (L4P-SP3) is a molecule well suited for efficient energy transfer as the introduction of spiro groups enables to evaporate stable amorphous films to be used in combination with a 2D ZnO heterostructures.
Non-radiative energy transfer was proven with a combination of photoluminescence excitation and time-resolved spectroscopy. Despite the energy red-shift of the 0-0 vibronic lines in respect with its L4P progenitor, new samples show efficiency of approx. 67% within a transfer time of approx. 60 ps.
A further proof of concept regarding the transfer mechanism was obtained by exciting the samples above the ZnMgO barrier band edge (E_{exc}=3.55 eV). For these excitation conditions, the long decay of the barrier was observed also in the decay curve measured on the QW and on the molecular emission.

Raising the temperature, the transfer efficiency decreases to 32% at room temperature. The temperature dependence of energy transfer can be influenced by possible variations of the spectral overlap and changes of the intrinsic properties of the QW excitons such as the dipole moments.
Matlab simulations enabled to exclude the spectral overlap as the main cause of the transfer rate behavior. It was demonstrated that the overlap factor increases of 3.5 times with increasing temperature, as the QW emission shifts towards lower energies. Observed result were interpreted in the context of the radiative properties of QW excitons as localised and free excitons show different energy transfer dynamics. In the samples under investigation the potential landscape experienced by excitons features a considerable density of traps that localize the electron-hole pairs at temperatures below approx. 110 K. Experiments showed that while the radiative decay rate intrinsically decreases with increasing temperature, non-radiative recombination is thermally activated resulting generally in low PL yields of inorganic semiconductor QW structures at room temperature.

Upon transfer experiments, charge separation at the organic/inorganic interface was found as the main obstacle for the molecular emission. In the actual configuration, an excited L4P-SP3 molecule transfers an electron to the ZnO conduction band resulting in quenching of the molecular emission. Time-resolved PL data show that the efficiency of the process can reach 90%. Thus 9 out of 10 excitons generated via ET in the organic layer do not decay radiatively. To overcome this intrinsic obstacle and for achieving HIOS with high luminescence yields, strategies have to be worked out for engineering the hybrid interface.

AUTHOR'S CONTRIBUTION

Heterostructures presented here are prepared by Dr. Sergey Sadovief who is responsible for the MBE apparatus.

Organic compounds were provided by Dr. Björn Kobin from the Prof. Ph.D Stefan Hecht laboratories.

Organic overlayers deposition, AFM imaging of the samples and optical characterizations were performed by the author. Time-transient evaluations (deconvolution and fitting) were performed by the author using a Matlab software provided by Dr. Sylke Blumstengel.

AFM pictures were taken thanks to a microscopy made available from Prof. Dr. Jürgen P. Rabe at the Humboldt University of Berlin.
AFM studies regarding the L4P-SP3 dewetting were performed by Moritz Eyer.

XRR measurements on the L4P-SP3 layers were performed by Anton Zykov, at the laboratory of Prof. Dr. Stefan Kowarik at the Humboldt University of Berlin.

UPS spectra were performed by Dr. Raphael Schlesinger, at the laboratories of Prof. Dr. techn. Norbert Koch always at the Humboldt University of Berlin.

6

CASCADE TRANSFER: FASTER THAN QUENCHING

This chapter presents a strategy to recover the molecular luminescence discussed in the previous chapter. Without modification of the hybrid design previously studied, the excitation energy is funnelled away from the hybrid interface by a secondary transfer step within the organic component, before interfacial exciton dissociation can take place. Parts of this chapter are based on the publications.[2,36]

6.1 MOTIVATION

In the previous chapter, efficient ET was demonstrated for the hybrid design consisting of ZnO/L4P-SP3. Unfortunately, despite the nominal transfer efficiency above 80 %, the total QY of the hybrid sample was found to be extremely small. The bottleneck for least luminescence was found to be the level alignment of the hybrid interface: in fact, previous experiments demonstrated that the molecular overlayer excitons are easily and effectively dissociated, darkening the samples. One can understand the dramatic effect of such interface as follow: in a series of process, in which each step-product is the reagent of following step, the total yield is defined as the product of each step efficiency as:

$$\eta_{tot} = \prod_i \eta_i$$

This concept can also be applied to the complete FRET process in HIOS. In this case the total yield of the molecule in a HIOS system, in absence of direct excitation, is defined as:

$$\eta_{L4P-SP3,H} = \eta_{ET} * \eta_{L4P-SP3}$$

The molecular QY ($\eta_{L4P-SP3}$), is defined as 1-$\eta_{Interface}$, so the more efficiently excitons are quenched, the less light is emitted. For such hybrid design, $\eta_{Interface}$ was measured to be approx. 90 %.[2,3]
Tuning the energy levels into a type-I alignment, by increasing the electron affinity of the molecules by chemical modification is difficult, as the energy offsets are very large.[102,103] Note that also the use of molecules with substantially

smaller HOMO-LUMO gaps will not completely circumvent the problem of competing charge separation. Experiments performed with the red-absorbing polymerpoly((9,9-dioctylfluorene) 2,7-diyl-alt-[4,7-bis(3-hexylthien-5-yl)-2,1, 3-benzothiadiazole]-20, 200-diyl),[104] showed a substantial decrease of the PL lifetime (from 1.1 ns to 315 ps) when deposited on ZnO.
To disable or at least limit the hybrid interface effect, a simple solution would be to introduce a wide band-gap interlayer to block electron (or holes) flow. Unfortunately, such solution is not a suitable approach for this system, as the ET rate strongly depend of the distance.[17,63]

This chapter presents a different strategy based on a fast and highly efficient ET cascade: following the primary transfer step starting at the ZnO QW, the excitation energy is funnelled away from the hybrid interface by a secondary energy transfer step within the organic HIOS part before interfacial exciton dissociation can take place.

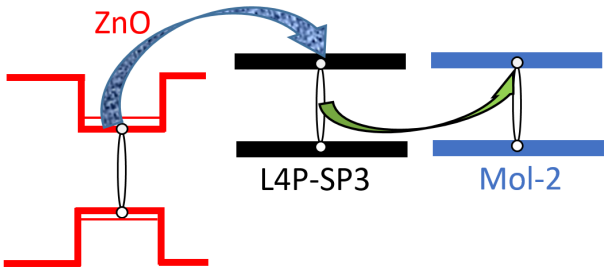

Figure 46: *Draft of the energy level alignment for a cascade sample: following the first energy transfer mechanism, another transfer step funnels the excitation towards Mol-2, away from the hybrid ZnO/L4P-SP3 interface.*

In this case, the new ET efficiency η_{ET2} and the new molecule QY will be introduced in the above formula. Supposing that all excitation gets transferred between to the second molecules, these two factors will replace $\eta_{L4P-SP3}$. The total yield becomes:

$$\eta_H = \eta_{ET} * \eta_{ET2} * \eta_{Mol-2}$$

It must be stressed that, introduction of these two additional factors could lead to a lower total efficiency, unless both η_{ET2} and η_{Mol-2} are close to unity. A proper second acceptor, must be chosen carefully so that η_{Mol-2} in solid state is as high as possible ($\eta_{L4P-SP3}$ = 50%) and that the second transfer step η_{ET2} reaches unity in the hybrid design considered, within a time shorter than the charges dissociation time. Supposing thus an accurate molecular choice, the limited luminescence efficiency of the primary molecule $\eta_{L4P-SP3}$ (in this case 0.1) is substituted by a much efficient double step process.

L6P: the cascade acceptor

As secondary acceptor and ET partner for L4P-SP3, a longer chain LOPP, namely ladder-type sexiphenyl (L6P) is selected (Fig. 47A). The ladder oligomer L6P, as for other LOPPs, can successively vacuum-deposited without undergoing thermal decomposition.[36]

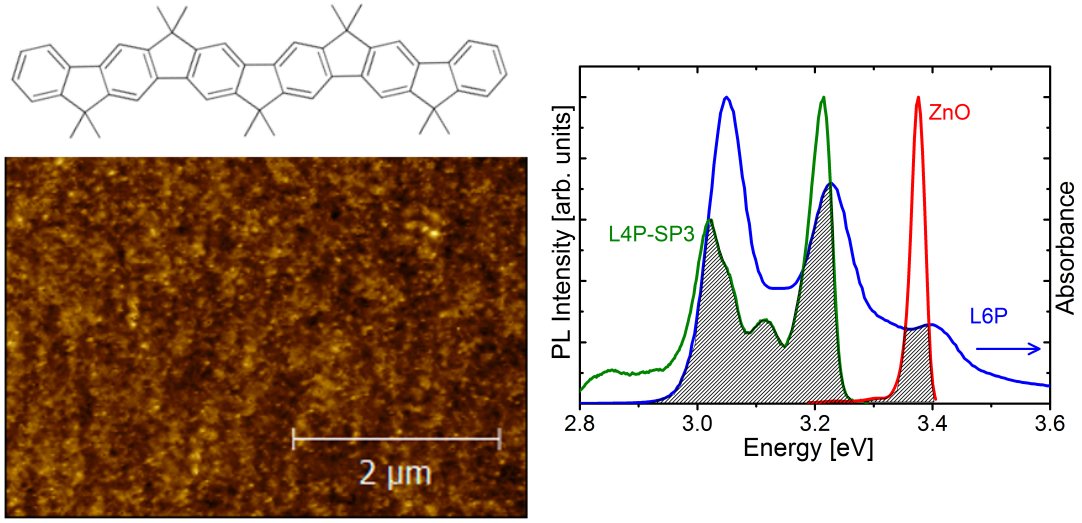

Figure 47: *Cascade acceptor: (A) Chemical structure of L6P.33 (B) Spectral overlap between the absorption spectrum of L6P dispersed in PS (green) with the emission spectra of L4P-SP3 (blue) and the ZnO QW (red). The inset shows the structure of L6P.*

The more extended π-electron system of L6P shifts its $S_0 \rightarrow S_1$ absorption in resonance with the L4P-SP3 emission, as shown in Fig. 47B. L6P has also some spectral overlap with the ZnO emission so that direct energy transfer from the QW to L6P is also possible.
The intermolecular coupling was maximized incorporating a small quantity of L6P into a L4P-SP3 layer by a co-evaporation method. A L6P fraction of 10% is low enough for avoiding phase separation, but still grantee high ET rates. The different mixing ratio was obtained by simultaneously evaporating the two molecules at different deposition rate (3 nm/min for L4P-SP3 and 0.3 nm/min for L6P). An AFM picture of the blend overlayer of sapphire is shown always in Fig. 47. A 3.5 nm layer of a L4P-SP3/L6P blend is grown on the chosen substrate.

6.2.1 *L4P-SP3-L6P Intermolecular Energy Transfer*

First, pure intermolecular ET is elucidated within the organic layer on an inert sapphire substrate. Energy transfer is demonstrated with a combination of PL, PL(t) and excitation spectroscopy. The PL spectrum of the blend sample is reported in Fig. 48A, the excitation wavelength is set to 3.41 eV. Such energy is in resonance with $S_{1,v=0}$ vibronic line of the L4P-SP3 and guarantees a negligible direct excitation of the L6P.

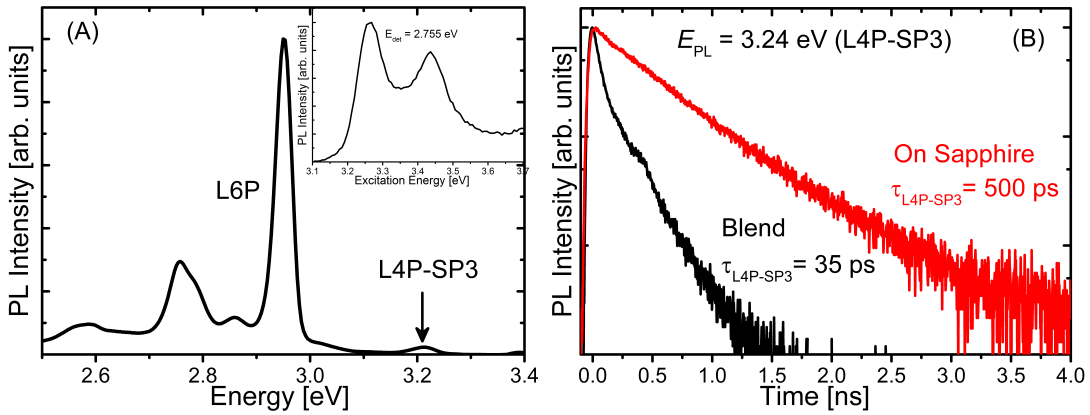

Figure 48: *ET in a L4P-SP3:L6P blend. (A) PL spectrum of a L4P-SP3:L6P blend evaporated on sapphire, E_{exc}=3.41 eV. Inset: PLE spectrum of the same blend recorded at the $S_{1,v=0} \rightarrow S_{0,v=1}$ PL transition of L6P (E_{det}=2.755 eV). (B) PL transients of L4P-SP3 in the blend (black curve) and in a reference sample (red curve). The excitation photon energy is E_{exc}=3.41 eV and T=5 K for all measurements.*

The blend PL is indeed dominated by the L6P emission, while the signal from L4P-SP3 is almost entirely quenched in presence of the acceptor molecules. PLE data corroborate highly efficient ET within the organic blend: the spectrum recorded at the vibronic $S_{1,v=0} \rightarrow S_{0,v=1}$ PL feature of L6P (E_{det}=2.775 eV) reproduces exactly the absorption spectrum of L4P-SP3 (inset Fig. 48A), and the direct excitation component of the luminescence is barely visible in the lower energy part of the spectrum. PL time traces for the blend are showed in Fig. 48B. The PL decay of L4P-SP3 in the blend can hardly be resolved by the photon counting device, providing an estimate of the time constant of the organic-organic ET $\tau_{ET} < 30$ ps at the present L4P-SP3/L6P mixing ratio. For such transfer time, a lower estimate of the efficiency is $\eta_{ET} > 0.9$. The decay time observed for L6P (curve not shown) is τ_{L6P} approx. 440 ps. High efficient energy transfer between the two molecules is thus demonstrated in a blend thin layer deposited on an inert substrate. The measured transfer time of 30 ps is obviously an upper estimation of the real transfer time, since it resembles the temporal resolution of the setup.

6.2.2 *Cascade ET in a Hybrid Sample*

Competition between the ET cascade and interfacial exciton dissociation is studied in a HIOS sample reported in the inset of Fig. 49. To avoid interaction between L6P and substrate, which in case of hybrid samples will be ZnO, a 0.5 nm thick interlayer of pure L4P-SP3 is introduced. To directly compare the benefits of the cascade process compared to the single step ET, 1/4 of the sample is covered with 4 nm of pure L4P-SP3 layer. The pump photons energy was chosen to be E_{exc}=3.46 eV, ensuring negligible direct excitation of L6P.

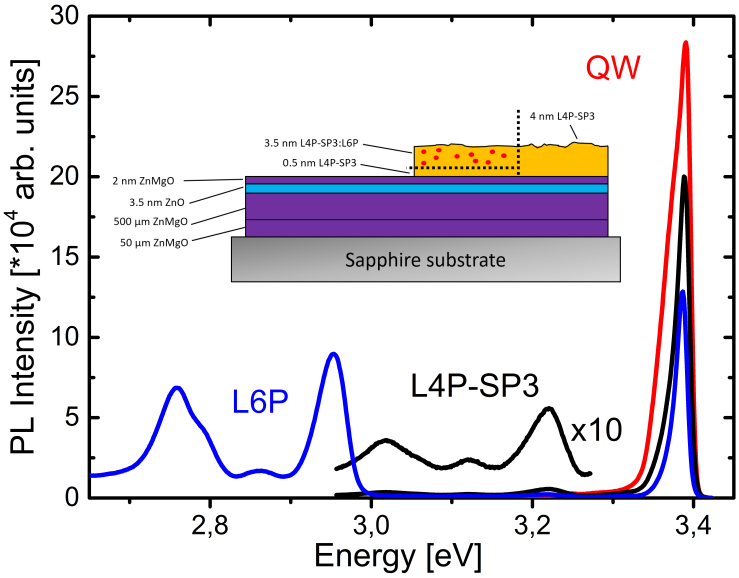

Figure 49: *Cascade ET in a L6P:L4P-SP3/ZnO/ZnMgO HIOS: PL spectra for all three areas of the sample. Emission of the reference QW (red curve) and for the hybrid sample (black curve), L4P-SP3 emission is magnified by a factor of* 10 *for better visibility. The blue curve is the spectrum acquired on the cascade hybrid sample. All spectra were acquired at T=5 K with an* E_{exc}=3.46 *eV. Inset: sketch of the cascade sample.*

Luminescence from the QW reference section (red line) decreases in presence of the L4P-SP3 layer (black curve), however, the molecular overlayer is barely emitting and is visible only after a 10 times magnification. These results are consistent with experiments presented in the previous chapter. Introduction of L6P (blue curve) changes this picture: the QW luminescence is further reduced by the second acceptor. In this case, a bright L6P luminescence dominates the spectrum, especially considering the extremely low concentration of the latter (10% of a 4 nm layer).

PLE experiments were performed on the blend. Excitation spectrum of the QW (red curve Fig. 50) displays the exciton ground and excited-state absorption features and the ZnMgO band edge ($E_{exc} > 3.57$ eV).

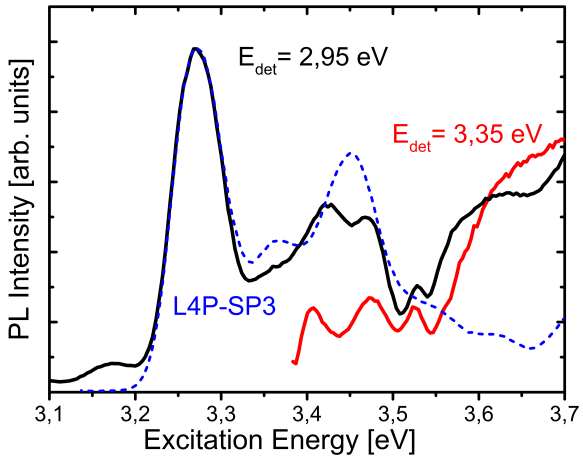

Figure 50: *Energy transfer in the cascade sample: spectrum detected on the ZnO emission (E_{det}=3.35 eV, red line) and spectrum detected on the L6P emission in the cascade sample (E_{det}=2.95 eV, black line). The blue dotted line is a PLE spectrum of L4P-SP3 evaporated on sapphire.*

Scanning the excitation wavelength on the L6P emission at 2.95 eV (black curve Fig. 50), the 0-0 vibronic line of L4P-SP3 is clearly visible at 3.27 eV, implying that the emission from L6P mainly originates from the donor molecule. In addition, direct contribution from the QW absorption can be seen, at 3.41, 3.47 and 3.53 eV respectively. Examining the spectrum at high energy ($E_{det} > 3.55$ eV) the barrier absorption feature also appear in the molecular spectrum. Finally, in the low energy part of the picture, direct excitation from the L6P can be seen at 3.17 eV, the small intensity of direct excitation confirm that L6P is almost entirely excited from energy transfer.

The non-radiative nature of the ZnO-L4P-SP3 energy transfer was already demonstrated and shown previously (Chapter 5). Nevertheless, comparison between the QW decay time τ_{QW} in presence or without the L6P should provide additional informations about any favourable effects. QW PL transients in the reference, hybrid and cascade HIOS are depicted in Fig. 51A. All time traces decay single exponentially, while the reference sample (red curve) has a time constant of τ_{QW}=200 ps, such time shortens to τ^{H}_{QW}=58 ps in presence of L4P-SP3 (green curve), a further shortening of the decay time is visible in presence of the blend (blue curve, 41 ps). The further shortening of the decay in presence of L6P confirm direct transfer from the QW. Using formulas previously discussed (Eq.31 and Eq.32), transfer time and efficiency for the cascade sample are respectively τ_{ET}=65 ps and η_{ET}=77%.

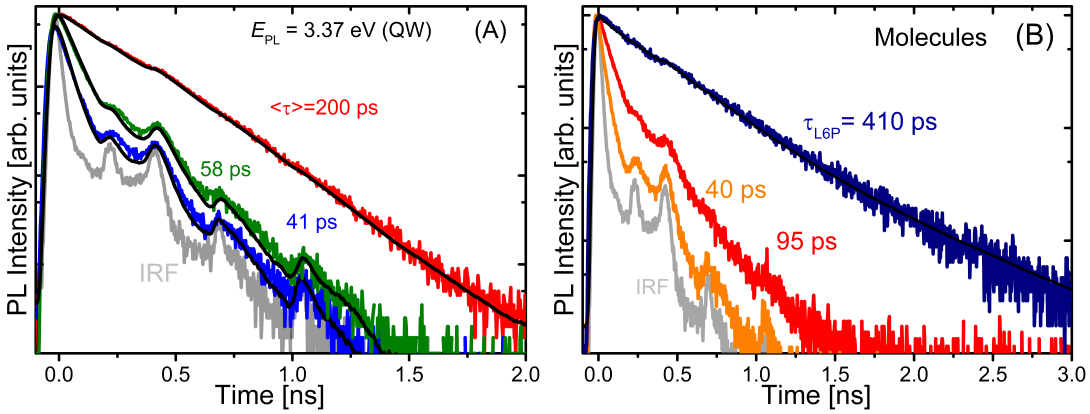

Figure 51: *ET in a L6P:L4P-SP3/ZnO HIOS. (A) PL transients of the ZnO QW in the reference (red curve), hybrid (green curve) and cascade (blue curve) part of the HIOS. The solid black lines are single-exponential fits obtained by convolution with the instrument response function (IRF) shown in grey. (B) PL transients of L4P-SP3in the hybrid (red curve) and in the cascade (orange curve) sample; PL transient of the L6P in the cascade sample is also reported (blue curve). The data fits are performed as in (A). The excitation photon energy is E_{exc}=3.46 eV and T=5 K.*

These findings indicate that the first step of the cascade is not flawed by the blend, but actually enhanced. The donor role of L4P-SP3 in the next cascade step is verified by a further shortening of its decay time (red curve Fig. 51B), from 95 ps to approximately 41 ps (orange curve Fig. 51B) and close to the 30 ps time resolution. Besides, in marked contrast to L4P-SP3 in the single-stepped ET, the PL decay time of L6P in the HIOS (dark blue curve τ_{L6P} approx. 410 ps) is nearly identical to that of the blend on an inert substrate. These observations imply that the excitation energy is effectively and efficiently funnelled away from the quenching effects of the ZnO surface.

Unfortunately, the decay time of L4P-SP3 in the non-blend part of the sample is already too short to estimate the intermolecular ET with the formula already used. Nevertheless η_M^H can be estimated by the quenching of the molecular emission in the presence of L6P acceptor, commonly defined as:[8,9]

$$\eta_{L4P-SP3\rightarrow L6P} = 1 - \frac{F_{DA}}{F_D}$$

where F_{DA} is the integrated fluorescence intensity of the donor (L4P-SP3) in presence of the acceptor (L6P) and F_D is the integrated fluorescence intensity of L4P-SP3 alone. By measuring the L4P-SP3 luminescence intensity change, an η_M^H approx. 0.9 is estimated. This finding reproduces the same value obtained on a sapphire substrate, confirming that the ZnO surface does not play any role in such transfer mechanism.

RECOVERY OF THE HYBRID LUMINESCENCE

After demonstrating the validity of the intermolecular ET independently from the substrate in use. The recovery of the molecular emission (R_{EM}) is measured by the ratio of the spectrally integrated L6P yield in the ”cascade” HIOS versus that of L4P-SP3 in the ”non-cascade” sample. As the inorganic-organic ET is practically identical, the experimental ratio R_{EM} approx. 10 can be inferred by scaling the yield in both samples relative to that of the QW emission. Theoretically, denoting by σ_{L6P} and $\sigma_{L4P-SP3}$ the radiative efficiency of the molecules in the respective HIOS, it holds:

$$R_{EM} = \eta_{ET}^{\infty} \frac{\sigma_{L6P}}{\sigma_{L4P-SP3}}$$

The radiative efficiency is:

$$\sigma_M = \frac{\tau_M^H}{\tau_M^{Rad}}$$

where the total molecular lifetime τ_M^H is directly measured (95 ps L4P-SP3, 410 ps L6P), while the ratio of the radiative lifetimes can be quantified by comparing the molecular extinction coefficients providing:

$$\frac{\tau_{L4P-SP3}^{Rad}}{\tau_{L6P}^{Rad}} \approx 2$$

finally, R_{EM}approx. $8\eta_{ET}^{\infty}$. This confirms the above estimate of η_{ET}^{∞} approx. 1 and demonstrates that ET from L4P-SP3 to L6P outpaced almost entirely the quenching of molecular excitons at the hybrid interface.

6.2.3 *Room Temperature Measurements*

Cascade ET persists up to room temperature as testified by the same set of measurements showed previously (Section 5.3.3). The primary transfer from the QW to L4P-SP3 stays reasonably efficient (η_{ET}^{RT}=0.32, extracted by Fig. 52B) and, most important, the L6P emission is bright (Fig. 52A). These findings are remarkable as the quantum yield of inorganic QW structures drastically declines at higher temperatures.

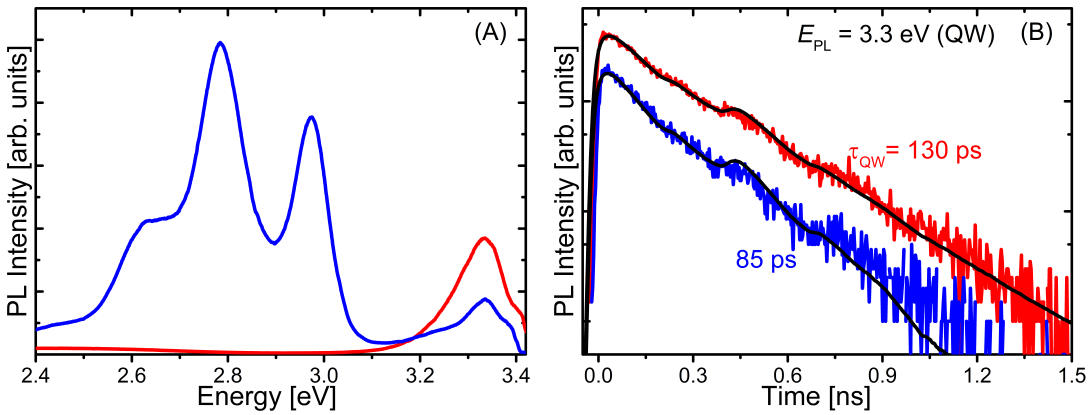

Figure 52: *Room temperature cascade ET in a L6P:L4P-SP3/ZnO/ZnMgO HIOS: (A) PL spectrum at T=300 K for the blend (blue curve) and for the sole QW (red curve). (B) PL transients of the ZnO QW (red curve) in the uncapped reference and in the cascade hybrid part (blue curve). The solid lines are fits to the data as described previously. The excitation photon energy is E_{exc}=3.46 eV.*

The most striking aspect of this spectrum is the bright L6P luminescence. While temperature behaviour and subsequent explanation for the ZnO→L4P-SP3 ET was discussed previously, here the cascade luminescence is the point of interest. The ET contribution from the QW excitons to the total L6P emission is measured under the present excitation conditions by the ratio:

$$\frac{\eta_{ET}^{RT} A_{QW}}{\eta_{ET}^{RT} A_{QW} + A_{L4P-SP3}} = 0.3$$

where $A_{L4P-SP3}$=0.07 and A_{QW}=0.1 are the fractions of photons absorbed in the L4P-SP3 layer and the QW, respectively. Therefore, a substantial part of QW excitons otherwise lost by non radiative recombination is recovered by ET for light emission.

6.3 CONCLUSIONS

This chapter presented an efficient solution to the detrimental charge separation happening at the hybrid interface. Molecular excitons quenching can be surpassed by a cascade ET, where the second step takes place within a blend of suitably adjusted organic components. L6P is chosen as candidate to pair L4P-SP3, intermolecular energy transfer reaches efficiencies of approx. 1 in blend nm-films on sapphire and on ZnO. OMBD films of L6P:L4P-SP3 blend manifest the same closed layer structure of pure L4P-SP3 together with a bright L6P emission. Finally, the intermolecular energy transfer can be considered as pure Förster type, as it is temperature independent.
Introduction of cascade mechanism in a hybrid sample does not reduce the total ET efficiency, which is actually enhanced by a direct ZnO-L6P transfer, as proven by the measured $\eta_{L4P-SP3}$=70% and η_{Blend}=77%. The more striking effect of the blend introduction is the bright luminescence measurable at RT, here about one third of the excitons primarily excited in the QW are passed to the LOPPs and emit light, whereas maximally one tenth would radiatively recombine in the sole QW.
Cascade ET could be furthermore used for efficient colour conversion: by introducing another molecular emitter in the range of yellow-green, the total emission would result in a bright white light. The design presented in this chapter could be further improved can be achieved by minimizing the ET distance or optimizing the molecular packing.

AUTHOR'S CONTRIBUTION

Heterostructures presented here are prepared by Dr. Sergey Sadovief who is responsible for the MBE apparatus.

Organic compounds were provided by Dr. Björn Kobin from the Prof. Ph.D Stefan Hecht laboratories. Organic overlayers deposition, AFM imaging of the samples and optical characterizations were performed by the author.

AFM pictures were taken thanks to a microscopy made available from Prof. Dr. Jürgen P. Rabe at the Humboldt University of Berlin.

UPS spectra were performed by Dr. Raphael Schlesinger, at the laboratories of Prof. Dr. techn. Norbert Koch always at the Humboldt University of Berlin.

7

HYBRID STRUCTURES: ENERGY-LEVEL TUNING

This chapter gives an alternative solution to the least HIOS luminescence discussed in the previous chapters. Here instead of funnelling excitons away from the hybrid interface, the level alignment itself is adjusted to inhibit the charge transfer and consequently recover the molecular luminescence.
Parts of this chapter are already published in.[3]

7.1 MOTIVATION

The energy level alignment across a heterostructure interface is one of the major parameters determining electronic device performance and thus, dictating materials selection.[70,105] Though the ZnO/L4P-SP3 HIOS appears ideally suited,[2] severe limitations originate from the level alignment discussed previously. In fact, instead of the target Type I alignment (Fig. 53A), a type-II discontinuity (Fig. 53B) is formed. Here, subsequent to energy transfer, charge separation occurs at the interface, leading to a strong quenching of the luminescence of the organic layer.

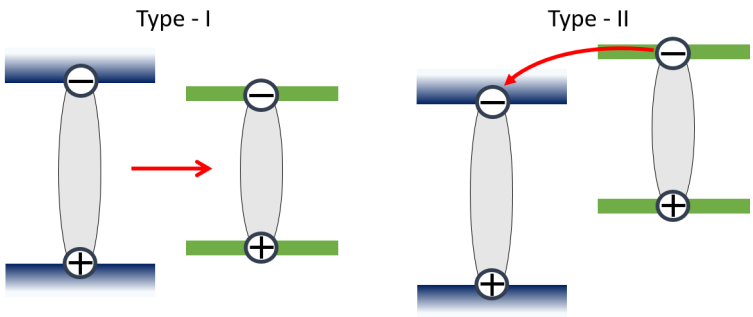

Figure 53: *Energy level alignment favourable for energy transfer and subsequent light emission (Type I) or charge separation (Type II).*

Aligning the frontier energy levels to switch off charge separation simply by molecular design can be difficult: partial fluorination of L4P shows yes an increasing of the electron affinity (fractions of 1 eV), but at the same time results detrimental for its optical properties with a decrease of QY and lower

photo-stability.[106]
A substantial lowering of the ZnO work function (WF, Φ) by more than 1 eV could be one way to arrive at the situation depicted in Fig. 53A. Consequently, the use of appropriate interlayers comprising dipoles between inorganic and organic layers to shift the electrostatic potential emerges as a natural way to tune the HIOS energy level alignment.
This chapter reports that employing the recently introduced air-stable donor $[RuCp^*mes]_2$[107–110] (chemical structure in Fig. 54), the Φ of ZnO reaches values of 2.2 eV, thus even rivalling those of alkali metals. This approach grants to achieve almost perfect alignment of the frontier levels of ZnO and of L4P-SP3, thereby drastically enhancing the radiative efficiency of the HIOS.

7.2 STATE OF THE ART

Molecular modification of semiconductor surfaces has long been studied as a method for surface state passivation and control of energy level alignment.[111] Usually, a material work-function (Φ) is modified using molecular layers, by one (or a combination) of two approaches:

1. A molecular dipole, perpendicular to the surface of the material, attached either by chemisorption or physisorption.

2. Charge transfer between an adsorbed molecule, and the material substrate.

Both approaches have been used successfully for Φ modification over a wide electrical potential range.
Surface modification of transparent conductors, using chemisorbed dipole layers, was studied[105,112] and a total change of Φ of 1.2 eV was achieved using molecules with different dipoles.
The approach of charge transfer between the molecule and the surface was employed successfully using polyethylenimine (PEI), polyethylenimine ethoxylated (PEIE)[113] and 2,3,5,6-tetrafluoro-7, 7,8,8- tetracyanoquinodimethane (F4TCNQ)[114] on many surfaces, including ZnO. Charge transfer between the organic modifier and the substrate, and resulting formation of a surface dipole (yielding Φ modification), can occur with electron donors or acceptors. Transfer of even a small fraction (e.g., 1/100) of an electron charge per molecule is sufficient to achieve a significant (tenths of V) Φ change, but the extent to which this occurs depends on the substrates initial conditions, such as the bulk doping level and the density and energies of the surface/interface states (which dictates the band bending of the free surface/interface[114]).
The change in electrostatics due to the charge transfer can extend beyond the exact position of the donor (acceptor) molecule[115] and even, in the case of low conductivity substrate, the excess charge carriers can significantly contribute to surface conductivity. Lowering the work function of ZnO using dipolar

self-assembled monolayers attached to ZnO has yet accomplished only moderate success; the lowest values achieved have been in the range of 3.5-4.3 eV,[102,116,117] which is insufficient to eliminate energy level offsets with most organic semiconductor materials.

7.3 EXPERIMENTAL

SAMPLE PREPARATION

$[RuCp^*mes]_2$ and L4P-SP3 were evaporated from resistively heated quartz crucibles onto bulk ZnO crystals purchased from Tokyo Denpa. Evaporation rates were in the range between 0.1 nm/min and 1 nm/min. Film thicknesses were monitored via quartz crystal microbalance and measured by AFM (Fig. 54). Scratching the sample surface by measuring in contact mode, the organic film breaks as seen in the picture. Extracted thickness corresponds to 0.3 nm. This confirms that $[RuCp^*mes]_2$, in the first few layers, forms homogeneous smooth films.

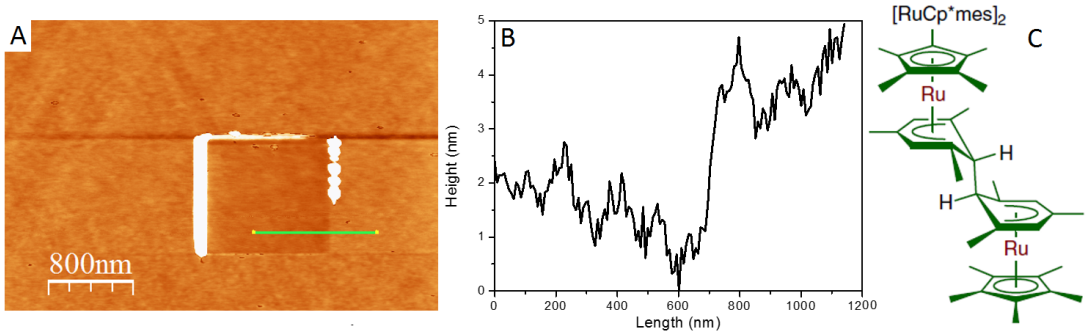

Figure 54: *$[RuCp^*mes]_2$ structural characterization. (A) AFM picture of a approx. 0.3 nm $[RuCp^*mes]_2$ layer grown on sapphire substrate. The height of the layer was deduced by scratching a portion of the sample (1μmx1μm) using the AFM in contact mode. (B) Height profile for the scratched portion to extract the thickness. (C) Chemical structure of $[RuCp^*mes]_2$.*

Prior to the experiments, ZnO crystals were cleaned by repeated Ar-sputter/annealing cycles (1 kV, 2μA, 40 min; 400 °C) and cleanliness verified by the C 1s emission below 1. Samples were handled with the same all-UHV procedure discussed previously.
Notably, by exposing a 5 nm L4P-SP3 film on $[RuCp^*mes]^*$/ZnO(000-1) to a nitrogen glove box atmosphere for 10 mins, only a minimal change of the interface energy levels is observed (lower than 0.1 eV). Therefore, these HIOS structures are remarkably robust with respect to handling outside of ultra-high vacuum conditions, which renders them of high practical relevance.

7.4.1 *Interface Energy Levels*

INTERLAYER EFFECTS ON ZNO

UPS photoelectrons spectroscopy (UPS and XPS, respectively) spectra are reported in Fig. 55. There, are shown the bare ZnO spectrum (black line) and the [RuCp*mes]$_2$ covered sample (green line).

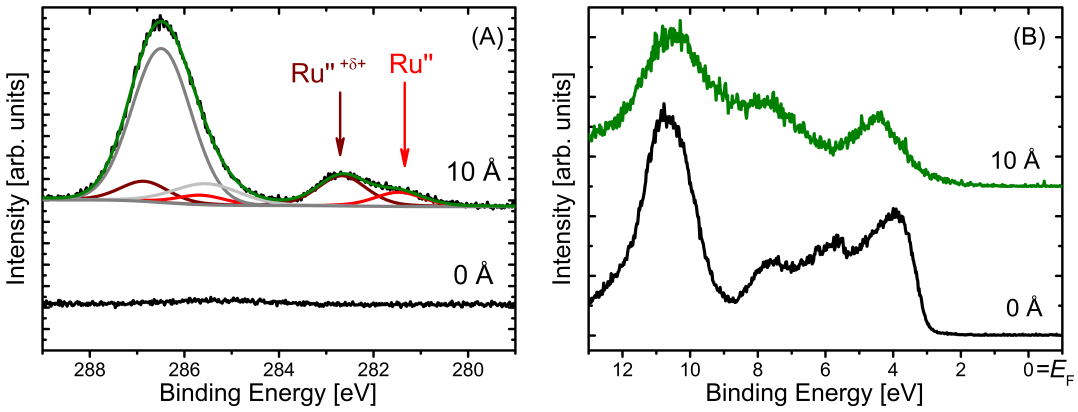

Figure 55: *Photo-emission spectra for [RuCp*mes]$_2$ deposited on O-terminated ZnO. (A) The left side panel shows the C 1s and Ru 3d core level regions. The two different Ru 3d5/2 peaks correspond to neutral [RuCp*mes]$_2$ dimer with Ru in (2) oxidation state (Ru^{II}) and to the cationic [RuCp*mes] with formal Ru oxidation state but lower electron density in the valence levels (Ru$^{II+\delta+}$). (B) The secondary electron cut-off (providing the work function Φ) and valence spectra are shown in the right panel. Black curves: bare ZnO. Green curves: after deposition of [RuCp*mes]$^+$ (nominal mass-thickness given in Å)*

Fig. 55A shows XPS data in the C 1s and Ru 3d core level regions and are consistent with the formation of [RuCp*mes]$^+$ on ZnO. On ZnO(000-1) two distinct Ru $3d_{5/2}$ peaks (the Ru $3d_{3/2}$ peaks are obscured by the C 1s peaks) are observed, providing evidence of two differently charged Ru species. Although the formal oxidation state of Ru is the same (2+) in both dimer and monomeric cations, the presence of the positive charge decreases the electron density in the Ru valence levels of [RuCp*mes]$^+$, which screens the core potential less efficiently and gives rise to a core-level shift to higher binding energy (BE); thus, the low BE peak is attributed to excess neutral (unreacted) [RuCp*mes]$_2$ and the high BE component to [RuCp*mes]$^+$.

UPS spectra in Fig. 55B show that the layer of [RuCp*mes]$_2$ reduces the ZnO work function by approx. 1.5 eV to a value of 2.7 eV. The Φ decreases is attributed to electron transfer from the interlayer to ZnO. It has been shown that [RuCp*mes]$_2$ and related dimers[118] react with organic acceptors to form two acceptors anions and two monomeric cations, in this case, [RuCp*mes]$^+$.[108,110]

It is noteworthy that the Φ change solely originates from the localized dipole formed by the $[RuCp^*mes]^+$ and the negatively charged ZnO as a result of the charge-transfer reaction. Contributions due to surface band bending are absent, as evidenced by the constant binding energy of Zn 3p and O 1s core levels even after deposition of [RuCp*mes] (see supplementary information in[3]).
This is fundamentally different from the situation of molecular acceptor interlayers, where a significant (0.8 eV) upward band bending in ZnO was observed.[114] However, this can easily be rationalized by the n-doped nature of ZnO: while molecular acceptors deplete the ZnO-native donor levels, molecular donors fill the ZnO conduction band. The orders-of-magnitude larger density of states of the conduction band, as compared with that of the native donors, strongly pins the Fermi level (E_F) as the ZnO turns degenerate.

Upon proving sole interlayer effects, UPS spectra were performed to asses the energy level alignment of bare and interlayer-covered ZnO, results are reported in Fig. 56.

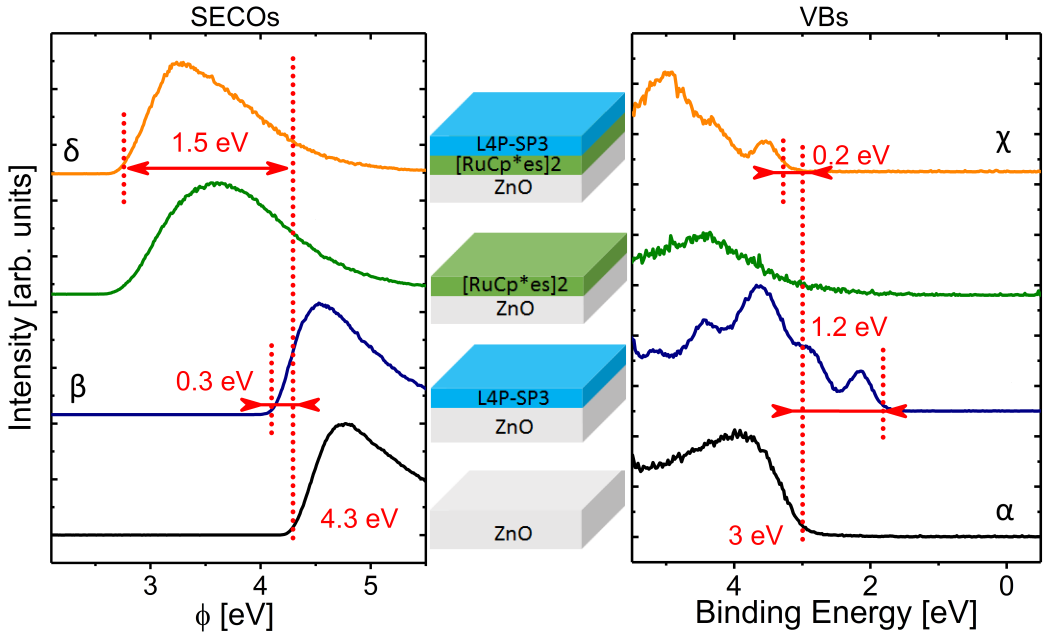

Figure 56: *HIOS energy levels with and without [RuCp*mes]$_2$ interlayer. UPS spectra of L4P-SP3 (blue curves) and ZnO (black curves). The effect of the interlayer is demonstrated on the O-terminated ZnO. The left panels (A) show the work function, the right panels (B) show the valence spectra. Corresponding HIOS structures (with/without interlayer) are sketched between the spectra.*

The valence band maxima of bare ZnO(000-1) is at 3.0 eV below E_F (α, black curve), implying slight upward surface band bending. Deposition of the sole L4P-SP3 layer reduces Φ by 0.3 eV (β, blue curve): this is often observed for organic materials physisorbed on metal oxides and attributed to a mechanism analogous to "push-back" on metal surfaces.[119] No new core level peaks arise in the O 1s and Zn 3p regions (curve not shown), suggesting that L4P-SP3 is physisorbed on the ZnO surface. It must be also noted that no L4P-SP3 thickness-dependent changes were observed in measurements up to 50 Å nominal coverage, i.e., multilayer.

The resulting HIOS energy level alignment without the interlayer, is thus of type-II with 1.2 eV of energy offset between the respective filled/empty frontier levels (blue curve Fig. 56 and Fig. 57A).

On [RuCp*mes]$^+$-covered ZnO(000-1), with a pristine Φ function of 2.7 eV (green curve Fig. 56), L4P-SP3 deposition does not induce a Φ change (δ, orange curve). The onset of emission from the level associated with the HOMO of L4P-SP3 is 3.2 eV below E_F (χ orange curve Fig. 56).

These observations, in combination with the the HOMO onset at 3.3 eV below E_F and in conjunction with the optical gap of 3.25 eV, lead to the conclusion that the level associated with the LUMO of L4P-SP3 is pinned at E_F (Fig. 56) This estimate ignores the effects of exciton-binding energy: although the transport gap of L4P-SP3 is yet unknown,[120] it is likely to be somewhat larger than the optical gap so that the actual LUMO level distribution is at and above E_F.[121] As Φ remains very low for both surfaces, no changes in the ZnO band bending occur.

The UPS spectral signature of L4P-SP3 with and without [RuCp*mes]* interlayer is the same (Fig. 57), so that the organic semiconductor levels are rigidly shifted in energy with respect to those of the inorganic component. Consequently, the interlayer aligns the energy levels of the HIOS system, with an offset of 0.1 eV Fig. 57B.

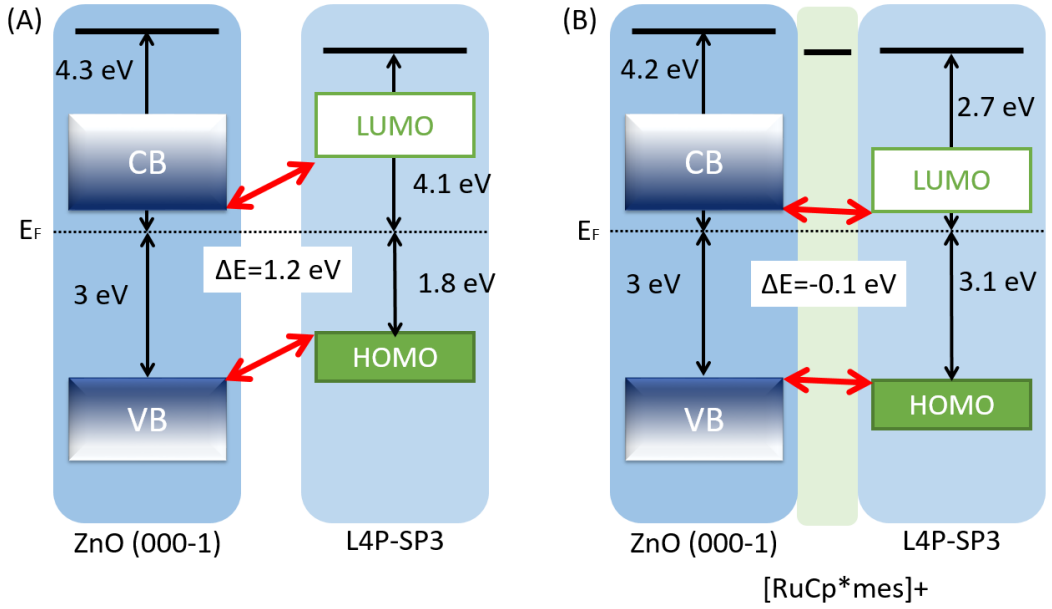

Figure 57: *Energy level diagrams: L4P-SP3 without interlayer on O-terminated ZnO(000-1) (A) and, with [RuCp*mes]$_2$ interlayer (B), respectively. Energy values are referenced to the Fermi level and in eV. The offset between L4P-SP3 and ZnO energy levels is highlighted in red. The L4P-SP3 LUMO region is shaded with a gradient to represent uncertainties due to the unknown transport gap.*

For efficient energy transfer, the conduction band minimum should also be in resonance with the LUMO level. L4P-SP3 transport gap (optical gap plus exciton binding energy) is assumed to be only slightly wider ($<$ 0.3 eV) than its optical gap as the rigidified structure lowers the binding energy. Thus, the offset between unoccupied frontier levels of the HIOS are estimated to be similar to those measured for the occupied levels.

7.4.2 *Energy Transfer and Radiative Recombination*

This section deals with the consequences of energy level optimization for the balance of energy transfer versus interfacial charge separation at the hybrid interface. Since efficient energy transfer was already largely demonstrated previously, results here concentrate on the beneficial effects of the $[RuCp^*mes]_2$ interlayer on the molecular luminescence.

SAMPLE PREPARATION

The inorganic part for this study consists of a $ZnO/Zn_{0.9}Mg_{0.1}O$ QW structure grown by molecular-beam epitaxy[30] with a 2 nm thin $Zn_{0.9}Mg_{0.1}O$ top barrier. The selected Mg content of 10% shifts the CBM (VBM) by 0.16 eV (0.06 eV) to higher (lower) energies as compared to ZnO.[22,122] This gap-widening of the top barrier is very small compared to the much larger inorganic/organic type-II level offset, thus charge separation is also expected for the pristine $Zn_{0.9}Mg_{0.1}O$/L4P-SP3 interface.
Using shadow masks during molecular deposition, three different hybrid structures were obtained on the same QW (Fig. 58): a 3 nm L4P-SP3 film on the QW structure (pristine HIOS, (ii)), ca. monolayer $[RuCp^*mes]_2$ embedded between the QW structure and 3 nm L4P-SP3 (optimized-HIOS, iii). For reference measurements, a portion of the sample surface is left without molecules (i).

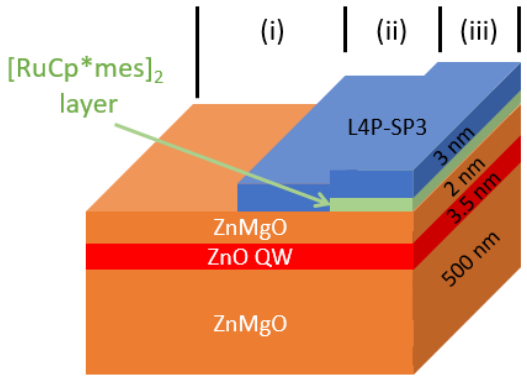

Figure 58: *Schematics and colour code of the investigated structures: grey (i) bare QW structure, blue (ii) HIOS consisting of the QW structure overgrown with 3 nm L4P-SP3, green (iii) HIOS with $[RuCp^*mes]_2$ interlayer.*

For the characterization of L4P-SP3 alone a further reference sample comprised an upright standing mono-layer of tetracontane[77] ($C_{40}H_{82}$) between L4P-SP3 and the QW structure, where neither energy transfer nor charge separation are of relevance.

The interplay of energy and electron transfer across the HIOS is elucidated by photoluminescence and time-resolved measurements at low temperature (T=5 K). At first, the transfer efficiency is investigated in the two hybrid samples. Because of the τ_{ET} distance-dependence,[17,31,63] the interlayer can be effectively used only if it doesn't shut off the transfer process. PL transient for the reference QW and for the two hybrid samples are reported in Fig. 59A.

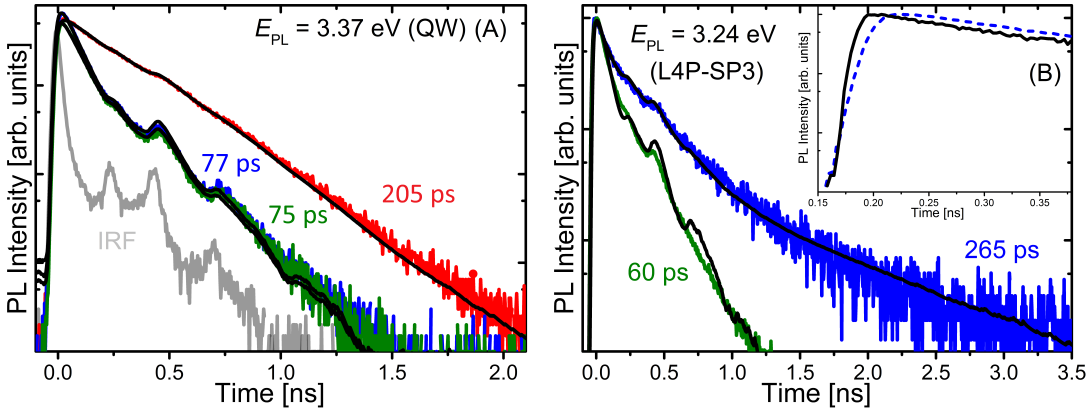

Figure 59: *Optical spectra of HIOS: (A) PL decay transients of the QW excitons (T=5K) of structures (i), (ii) and (iii). Light grey: instrumental response of the time-correlated single-photon counting set-up on the fs excitation pulse. Only the QW is primarily excited. Solid curves are fits to the data by convoluting exponential transients N(t) (up to three components) with the instrumental response function IRF. (B) L4P-SP3 PL transients of (ii, blue curve) and (iii, red curve) measured at E_{det}=3.24 eV. The excitation photon energy 3.3 eV. Inset: transients of (iii) right after excitation demonstrating the presence of a rise time (dashed curve) for an excitation energy (E_{exc}=3.46 eV).*

QW exciton lifetime, τ_{QW}=205 ps in the reference structure (red curve Fig. 59A), shortens to τ^{H}_{QW}=75 ps in the HIOS (ii) (green curve) sample. The lifetime of QW excitons in structure (iii) (blue curve) is not markedly changed, though the donor-acceptor spatial separation is widened by the ca. 0.3 nm thickness of the [RuCp*mes]* interlayer. With the formulas previously described (Eq.31, Eq. 32), transfer time of τ_{ET}=115 ps and efficiency of η_{ET}=0.65 are extracted, these values are in agreement with previous results presented on analogous structures (Chapter 5). Also in line with previous findings, a short molecular lifetime τ^{H}_{m}=60 ps is found for the structure (ii) (green curve Fig. 59B). The low emission yield and the short lifetime are a direct result of the type-II energy level alignment of pristine HIOS.

In the thin (3 nm) L4P-SP3 layer used here, diffusion of excitons towards the interface is not an important factor. Thus, the characteristic time and efficiency of the charge separation process can be estimated using the previous formulas (Eq. 37 and Eq . 38). Results are τ_{CT}=65 ps and η_{CT}=0.9 respectively. That

is, 9 out of 10 excitons generated (directly or indirectly) in L4P-SP3 are not converted into emitted light.
The $[RuCp^*mes]_+$ interlayer in structure (iii) alters the scenario profoundly. L4P-SP3 lifetime recovers to a value of τ_m^M=265 ps (blue curve Fig. 59B) proving suppression of excitons quenching. Evidence of efficient energy transfer is provided by the presence of a rise time in the L4P-SP3 emission, now resolvable due to the longer decay time (inset Fig. 59B), displaying the arrival of the excitons in the organic layer.
Fully consistent with the change in lifetime, the molecular emission in the optimized-HIOS increases by a factor of seven compared to structure (ii) (Fig. 60, blue and green curve respectively).

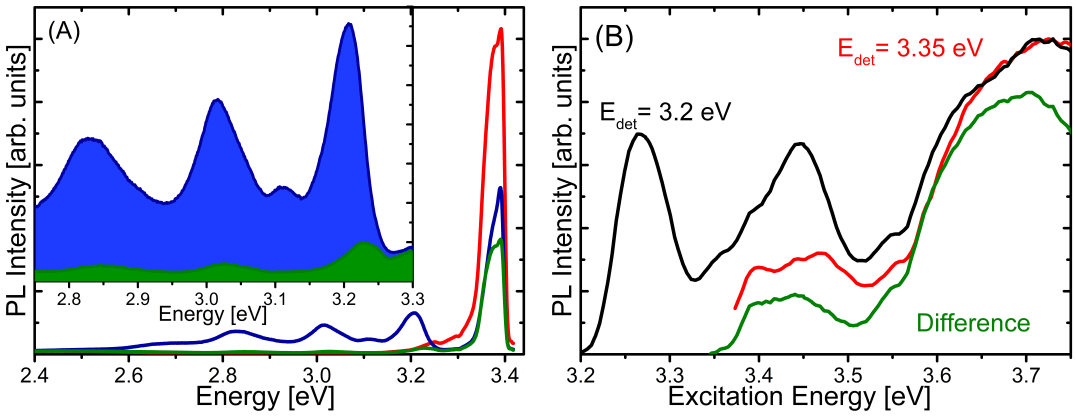

Figure 60: *Optical spectra of HIOS: (A) PL spectra of structures reference QW (red curve), HYBRID and optimized-HIOS (green and blue curve respectively). Inset: sevenfold increase of the molecular luminescence of the optimized-HIOS. The excitation energy was E_{exc}=3.46 eV. (B) PLE spectra for the QW reference (E_{det}=3.35 eV, red curve) and optimized-HIOS (E_{det}=3.2 eV, black curve). The green curve is obtained subtracting a reference L4P-SP3 absorption spectra from the black curve. All spectra were obtained at T=4 K.*

The energy transfer from the QW to L4P-SP3 in structure (iii) is also demonstrated by PLE (Fig. 60). The excitation spectrum taken on the $S_{1,0}$-S0, 1 line of the molecular emission exhibits the absorption features of both QW and ZnMgO barrier.
The yield of photons emitted by the L4P-SP3 layer per electron-hole pair generated in the QW is:

$$\eta = \eta_{ET} * \eta_{PL,L4P-SP3}$$

The latter quantity is the emission yield of L4P-SP3 in the hybrid structure. As there is still residual exciton quenching at the ZnMgO interface, $\eta_{PL,L4P-SP3}$ approx. 0.55 assuming that the intrinsic PL yield of L4P-SP3 approaches unity. Hence, the total luminescence yield of HIOS (iii) is η approx. 0.35.

7.4.3 *Molecular Luminescence at Room Temperature*

At room temperature, the role of the interlayer is crucial for the molecular emission. Normalized RT spectra for the HIOS (ii) and optimized-HIOS (iii) are reported in Fig. 61A.

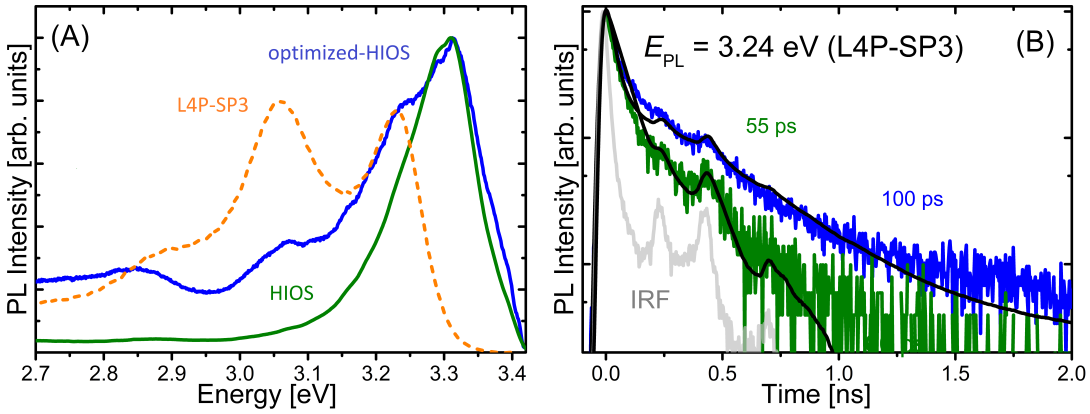

Figure 61: *Room temperature effect of [RuCp*mes]$_2$. (A) PL spectrum for the HIOS sample (ii) (green curve) compared with the optimized-HIOS (iii) (blue curve). The orange dotted line is a RT luminescence spectrum of a L4P-SP3 reference sample. (B) L4P-SP3 PL transients of (ii, blue curve) and (iii, red curve) measured at the detection energy E_{PL}=3.24 eV. The excitation photon energy 3.3 eV is below the ZnO absorption edge. Solid black curves are fits to the data by convoluting exponential transients (2 components) with the instrumental response function IRF (grey curve).*

Whereas L4P-SP3 emission from structure (ii) is no longer detectable (green curve Fig. 61A), the molecular signal remains visible in case of structure (iii) (blue curve Fig. 61A).
In agreement with the luminescence spectra, the interlayer effect can be observed on time traces acquired on the molecular luminescence in Fig. 61B. L4P-SP3 lifetime recovers to a value of τ_m^M approx. 100 ps (blue curve Fig. 61B) for structure (iii) from an initial value of τ_m^M=55 ps of unmodified structure (ii) (green curve).
Despite this improvement of radiative emission yield, particularly at room temperature, the present HIOS can further be optimized, since a considerable fraction of excitons still is not converted into light. This might be traced back to interface states, which are too low in intensity to be directly revealed by photo-emission.

7.5 CONCLUSIONS

This chapter presented a simple method to tune the energy level alignment for hybrid inorganic-organic semiconductor structures. The work function of the ZnO is lowered to a record value of 2.2 eV by depositing the organometallic donor dimer $[RuCp^*mes]_2$, which adopts the cation monomeric $[RuCp^*mes]^*$ form in contact with the oxide surfaces.
Upon deposition of $[RuCp^*mes]_2$, the ZnO work function decreases till the record value of $\Delta\phi$=−1.5 eV. The subsequently deposited L4P-SP3 rigidly shifts its energy levels with respect to those of ZnO. Hence, the $[RuCp^*mes]_2$ interlayer aligns the filled/empty frontier levels of the HIOS.
For such tailored interface, excitons dissociation and charge separation are found to be significantly reduced: current design shows a sevenfold increase of the emission yield of the L4P-SP3 overlayer while the transfer efficiency (67%) was not reduced by the interlayer.
Even at room temperature, where the luminescence yields of inorganic semiconductors is notoriously low, a substantial part of the ZnO excitons, otherwise lost by non-radiative recombination, is recovered by energy transfer to the organic emitter layer and then used for light emission.
These results in combination with high ambience stability of $[RuCp^*mes]_2$, substantiates the huge potential of such structures in light emitting applications. Usage of such layers is applicable to optimize the energy levels in a wide range of HIOS, especially with wide-gap inorganic semiconductors.

AUTHOR'S CONTRIBUTION

Dr. Raphael Schlesinger, the author, C. C. and R. O. performed the experiments.

The organic overlayers were deposited by Dr. Sylke Blumstengel on heterostructures prepared by Dr. Sergey Sadovief.

Dr. Raphaels Schlesinger and Dr. Sylke Blumstengel analysed the data. Björn Kobin, K. M., S. Barlow, Stephan Hecht and S. M. provided the organic molecules.

8

CONCLUSIONS

This work focussed on the design, preparation and characterization of organic-inorganic hybrid structures for energy transfer studies. The investigated system consists of a high quality ZnO single quantum well as energy transfer donor and an organic layer of ladder-type oligo(p-phenylene)s (LOPPs) as acceptor. Organic-inorganic hybrid structures are possible candidates for new generations of white light emitting diodes; characterized by better performances of commercial phosphors-based, or fully organic, devices. The rich emission variety and the tunability of organic materials would allow a better colour rendering of the final device which would combine the high carrier injection of the inorganic UV component and the fast decay times (ps-ns) of the organic emitter, so that ultra-fast modulation would be also achievable.
At the starting point of this work, the hybrid FRET-based device under study suffered from two main push-backs:

- No electrical injection for ZnO heterostructures: ZnO is intrinsically an n-type semiconductor. Any attempt of p-doping is compensated by the formation of Oxygen vacancies, balancing for the extra holes.[42,49]

- Improper alignment of the frontier energy levels: π-conjugated molecules in contact with wide gap inorganic materials such as ZnO display a strong or even complete suppression of their luminescence[13,18,29] caused by a Type II interface.[68]

The newly synthesized ladder-type quaterphenyl (L4P), because of its high extinction coefficient (100000 cm^{-1}[36]) and its quantum yield, which is close to unity in solution, L4P was found to be an ideal emitter for a hybrid system. L4P displays sharp intense vibronic features (FWHM approx. 0.1 eV) and its absorption spectrum is in resonance with the low temperature emission of the ZnO heterostructure (Fig.21, Ch.4). Energy transfer was demonstrated in a hybrid design consisting of a 3.5 nm ZnO single quantum well sandwiched between two ZnMgO barriers with a thin molecular layer (Ch.4) spincasted on top.
Layers of sole L4P display a Volmer-Weber growth mode,[36] which is detrimental for energy transfer experiments. For these measurements, L4P was encapsulated into a high glass-transition temperature Poly-Styrene (PS) layer

and spin-coated on top of the quantum well.[17,18,81] Experiments were carried out using a 3 nm layer of PS with a 20 wt.% (weight percent) concentration of L4P.
In the resulting hybrid samples, energy transfer was demonstrated by following methods: photoluminescence excitation and time resolved spectroscopy. The transfer efficiency reached 50% within a transfer time of 230 ps. The above results have to be considered as proof-of-concept experiments, confirming that LOPPs are suitable candidate for FRET-based hybrid devices.
However, the transfer efficiency value of 50% does not represent a state-of-the-art result. The bottleneck of the transfer mechanism turns out to be the actual sample geometry (Section 4.4 Ch. 4). The low density of molecules in the layer reduces the effective transfer rate, as only molecules directly at the ZnO interface are eligible to be sensitized.
A crucial disadvantage of L4P found in further experiments is its extremely low photo-stability.[1] Thin films and solutions of L4P decompose in seconds under UV excitation, indicated by conversion of the blue emission into a green-yellow emission (Fig. 26). Such a molecular degradation and colour conversion was already largely studied in L4P forefathers such as poly-fluorene and poly-para-fluorene. In our investigation, kinetic and mass spectrometry degradation studies revealed two important findings about the photo-degradation mechanism L4P and poly-fluorene:

- the degradation product was found to be a formylated-substituted L4P, named here L4P-deg, and not a fluorenone as largely stated in literature (chemical structure shown in Fig. 30).

- studies of L4P solutions[1] and thin films (Section 4.6 Ch.4) showed that the green luminescence of the L4P-deg species is steamed by pristine L4P molecules via fast end efficient L4P-L4P-deg FRET.

Before further experiments, L4P was chemically modified to improve its structural properties and its photo-stability. Triple-spired L4P (L4P-SP3) was selected for further experiments (Ch.5): unlike its parent, L4P-SP3 can be evaporated in amorphous closed layers on different surfaces including ZnO (Fig. 34) and shows the best photo-stability compared to other spiro-substituted LOPPs (Fig. 32). For the combination ZnO/L4P-SP3, energy transfer reaches an efficiency of $\approx$ 67% within a transfer time of 77 ps.
A further proof of the carrier transfer from the ZnO to the molecules was obtained by exciting the samples above the ZnMgO barrier band-edge (E_{exc}=3.55 eV). For these excitation conditions, the long decay time of the barrier was observed also in the decay curves measured on the QW and on the molecular emission, respectively.

At room temperature, the transfer efficiency decreases to about 32%. This was the first measurable energy transfer result at room temperature for ZnO based hybrid structures. The temperature behaviour of the energy transfer could be influenced by variations of the spectral overlap and changes of

the intrinsic properties of the QW excitons. Thanks to simulations (Fig. 43), variations of the spectral overlap was excluded as the main cause of the transfer efficiency behaviour.
The observed results on the temperature dependence of the energy transfer efficiencies (Section 5.3.3 Ch.5) were interpreted in the context of the QW excitons properties. A combination of photoluminescence and time-resolved spectroscopy unveiled the transition a change in the excitons nature from bound to free excitons with increasing temperature. Section 5.3.3 shown that below 110 K the electron-hole pairs in the QW are localized within energy traps in the potential landscape; above that temperature, excitons acquire sufficient kinetic energy to escape potential traps and become free (Fig. 44). This excitonic transition was used to explain the behaviour of the transfer rate with increasing temperature, as the free excitons wave-vector becomes too large for efficient dipolar coupling.
Despite the efficient transfer mechanism, the molecular layer in contact with ZnO barely shines light. Photoluminescence and UPS experiments revealed an efficient charge separation in these samples as approximately 90% of the molecular excitons are shut-off by the hybrid interface. UPS data estimated the energy offset between the valence band maximum of ZnO and the L4P-SP3 HOMO to 1.2 eV.

Following experiments focussed on the solution, or the avert, of the above observed molecular excitons destruction.

One successful approach was the introduction of a secondary energy transfer step within the organic layer (Ch.6). A longer π-chain ladder phenyl (L6P) was selected as energy transfer partner of L4P-SP3.
Blend films with a molecular ratio of 1:10 were deposited by OMBD. The molecular ratio was tuned by changing the deposition rate of the two molecules (3 nm/min for L4P-SP3 and 0.3 nm/min for L6P). Overlayers prepared with this mixing ratio display the closed layer structure of L4P-SP3 (Fig. 47) together with the emission characteristics of the sole L6P. Energy transfer experiments showed an intermolecular transfer efficiency close to unity (Fig. 48).
The same blend film was successfully deposited on ZnO heterostructures (sample structure in inset Fig. 49). The total ET efficiency measured reaches approx. 80% within a transfer time of 45 ps, the higher efficiency from previous result was attributed to direct transfer between ZnO and L6P. Importantly, the cascade samples show a radiant L6P luminescence (Fig. 49). Time resolved measurements on the L6P emission revealed the absence of quenching effects of the ZnO surface. L6P shows identical lifetimes ($\tau_{L6P} \approx 400$ ps) both on sapphire substrate and on ZnO substrate. Remarkably, the beneficial outcomes of the cascade mechanism manifest especially at room temperature. Here, one third of the QW excitons are passed to the molecules, but the samples still show intense L6P emission (Fig. 52).

The last chapter (Ch. 7) described another approach to the charge separation push-back. The energy level alignment at the hybrid interface was tuned

using a newly synthesized solution-processable organometallic donor dimer reductant $[RuCp^*mes]_2$ interlayer.
Employing $[RuCp^*mes]_2$, strong downward energy-level shifts of 1.3 eV were observed, which realigned the energy levels of L4P-SP3 to match the ZnO conduction band. Upon deposition of the interlayer, the subsequently deposited L4P-SP3 molecules realign their energy levels turning the Type II interface into the targeted Type I. This strategy was used to lower the ZnO work function to the record value of 2.2 eV (Fig. 57A).
Although further optimization is needed, it was shown that the interlayer does not disturb the transfer mechanism: the efficiency of the energy transfer in interlayer-modified structures is comparable to the energy transfer efficiency in samples without the interlayer (67% efficiency). Investigation on L4P-SP3 emission showed a sevenfold increase of the molecular luminescence and of the decay time (Fig. 59), respectively.

It was also observed that in hybrid structures without the interlayer, approximately 10% of the the excitons generated in the organic layer recombine radiatively. Such percentage triples to approximately 30% with the introduction of the Ru-interlayer. At room temperature, the interlayer enables a detection of the molecular emission which is not visible in structures without the interlayer.

8.1 FUTURE WORK

The results presented in this work demonstrate that organic/inorganic hybrid nanostructures with well-defined interfaces and bright molecular emission can be realized.
Basing on these findings, future work could proceed following two parallel strategies:

- exchanging the L4P-SP3 acceptor, to further optimize the spectral overlap with ZnO.
- interchanging the ZnO inorganic donor with a donor that allows injection of carriers.

In the following these two strategies are described in details.

iso-LOPPs as Organic Acceptor

A variation of LOPPs, with a different bended configuration called iso-LOPPs (chemical structure of iso-L4P-SP2 in Fig. 62A) can be now synthesized. This class of molecules posses an absorption maximum approximately 40 meV blue-shifted compared to L4P (Fig. 62B) and thus a higher spectral overlap with ZnO heterostructures. The Stokes-shift for iso-L4P-SP2 is still small and the fluorescence quantum yield in solution is close to unity.

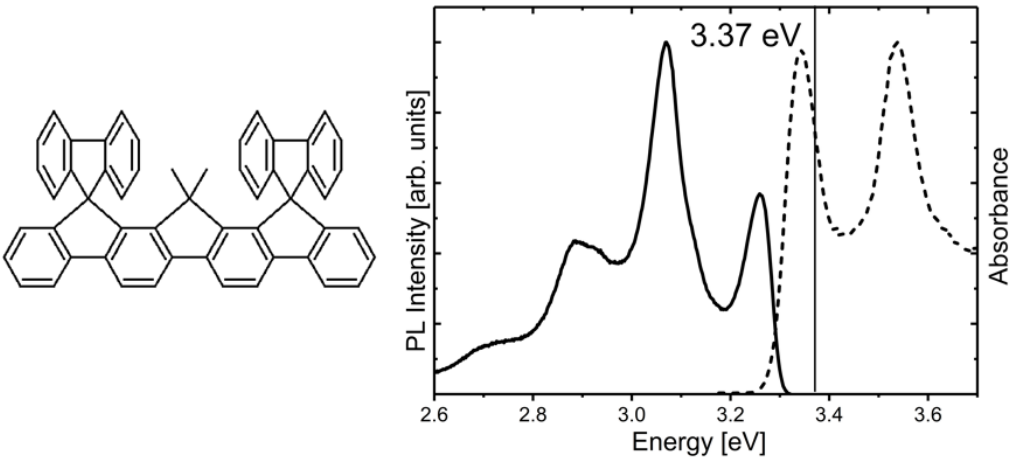

Figure 62: *Optical properties of an evaporated layer of iso-L4P-SP2 at room temperature. The thin black line at 3.37 eV corresponds to the ZnO QW low temperature emission. Spectra were acquired upon excitation at 4.2 eV by a Xenon lamp.*

Preliminary OMBD tests on iso-L4P-SP2 show the same closed layer growth regime that characterizes L4P-SP3, making these molecules suitable for HIOS devices. Simulations show that with the above molecule, it could be possible to reach transfer efficiencies above 80% within shorter transfer times.

For the ZnO/iso-L4P-SP2 pair, the results of chapters Ch. 6 and Ch. 7 would still be valid: an active interlayer can tune the Type-II interface into a desired Type-I interface, or a cascade FRET-blend could reduce the charge dissociation at the hybrid interface.

Electrically Pumped QW

In this work, the sample studied employed ZnO quantum wells as inorganic donor. Despite strong efforts, ZnO still cannot be electrically pumped, as reliable p-doping is yet to be achieved. Thus, future work should involve other donor materials like p-GaN and p-type oxides such as Li-doped NiO and NiMgO. On this basis, 2D bipolar heterojunctions could be produced. Epitaxial growth experiments show that a combination of n-ZnO on p-GaN is possible.[123,124] Using these materials, preliminary inorganic LEDs were already prepared. Electro-luminescence spectra of a n-ZnO and p-GaN heterostructure are reported in Fig. 63.

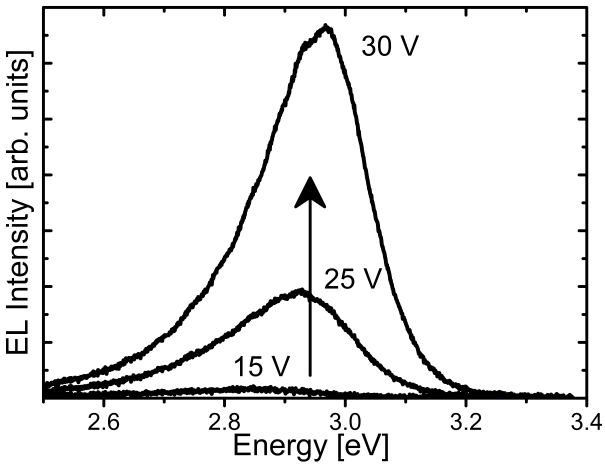

Figure 63: *Electro-luminescence spectra for n-ZnO epitaxially grown on p-GaN.*

Further experiments are required to understand the origins of the detected emission and to gain a better understanding of these structures. If this material combination is going to be used in hybrid light-emitting devices, it is also necessary to shift the emission to higher energies via carrier blocking, quantum confinement or polarity inversions.

BIBLIOGRAPHY

[1] B. Kobin, F. Bianchi, S. Halm, J. Leistner, S. Blumstengel, F. Henneberger, and S. Hecht. Green Emission in Ladder-Type Quarterphenyl: Beyond the Fluorenone-Defect. *Advanced Functional Materials*, 24(48):7717–7727, **2014**. http://dx.doi.org/10.1002/adfm.201402638.

[2] F. Bianchi, S. Sadofev, R. Schlesinger, B. Kobin, N. Koch, F. Henneberger, and S. Blumstengel. Cascade Energy Transfer versus Charge Separation in Ladder-type oligo(p-phenylene)/ZnO Hybrid Structures for Light-Emitting Applications. *Applied Physics Letters*, (23), **2014**. http://scitation.aip.org/content/aip/journal/apl/105/23/10.1063/1.4903517.

[3] R. Schlesinger, F. Bianchi, S. Blumstengel, C. Christodoulou, R. Ovsyannikov, B. Kobin, K. Moudgil, S. Barlow, S. Hecht, S. B. R. Marder, F. Henneberger, and N. Koch. Efficient Light Emission from Inorganic and Organic Semiconductor Hybrid Structures by Energy-Level Tuning. *Nature Communication*, **2015**. http://www.nature.com/ncomms/2015/150415/ncomms7754/abs/ncomms7754.html.

[4] V. M. Agranovich, Yu. N. Gartstein, and M. Litinskaya. Hybrid Resonant Organic-Inorganic Nanostructures for Optoelectronic Applications. *Chemical Reviews*, 111(9):5179–5214, **2011**. http://dx.doi.org/10.1021/cr100156x.

[5] V. M. Agranovich, D. M. Basko, G. C. La Rocca, and F. Bassani. New concept forOrganic LEDs: non-radiative Electronic Energy Transfer from Semiconductor Quantum Well toOrganic overlayer. *Synthetic Metals*, 116(1-3):349–351, **2001**. http://dx.doi.org/10.1016/S0379-6779(00)00435-5.

[6] V. M. Agranovich, G.C. La Rocca, and F. Bassani. Efficient Electronic Energy Transfer from a Semiconductor Quantum Well to an Organic Material. *Journal of Experimental and Theoretical Physics Letters*, 66(11):748–751, **1997**. http://dx.doi.org/10.1134/1.567592.

[7] T. Makino, Y. Segawa, M. Kawasaki, and H. Koinuma. Optical Properties of Excitons in ZnO-Based Quantum Well Heterostructures. *Semiconductor Science and Technology*, 20(4):78, **2005**. http://stacks.iop.org/0268-1242/20/i=4/a=010.

[8] M. Pope and H. E. Swenberg. *Electronic Processes in Organic Crystals and Polymers*. 2nd edition edition, December **1999**. OUP USA.

[9] B. Di Bartolo and X. Chen. *Advances in Energy Transfer Processes*. **2001**. World Scientific Pub Co Inc.

[10] F. Bassani and V. M. Agranovich. *Electronic Excitations in Organic Based Nanostructures*. **2003**. Academic Pr.

[11] C. Sommer, J. R. Krenn, P. Hartmann, P. Pachler, M. Schweighart, S. Tasch, G. Leising, and F. P. Wenzl. On the Requirements for Achieving Angular Homogeneity in Phosphor Converted High Power Flip-Chip Light-Emitting Diodes. *Japanese Journal of Applied Physics*, 48(7*R*), **2009**. http://stacks.iop.org/1347-4065/48/i=7R/a=070208.

[12] C. W. Tang and S. A. VanSlyke. Organic Electroluminescent Diodes. *Applied Physics Letters*, 51(12):913–915, **1987**. http://scitation.aip.org/content/aip/journal/apl/51/12/10.1063/1.98799.

[13] S. Blumstengel, H. Glowatzki, S. Sadofev, N. Koch, S. Kowarik, J. P. Rabe, and F. Henneberger. Band-offset Engineering in Organic/Inorganic Semiconductor Hybrid Structures. *Phys. Chem. Chem. Phys.*, 12:11642–11646, **2010**. http://dx.doi.org/10.1039/C004944C.

[14] G. Itskos, G. Heliotis, P. G. Lagoudakis, J. Lupton, N. P. Barradas, E. Alves, S. Pereira, I. M. Watson, M. D. Dawson, J. Feldmann, R. Murray, and D. D. C. Bradley. Efficient dipole-dipole coupling of Mott-Wannier and Frenkel Excitons in (Ga,In)N Quantum Well/Polyfluorene Semiconductor Heterostructures. *Physical Review B*, 76:035344, Jul **2007**. http://link.aps.org/doi/10.1103/PhysRevB.76.035344.

[15] G. Itskos, C. R. Belton, G. Heliotis, I. M. Watson, M. D. Dawson, R. Murray, and D.D.C. Bradley. White Light Emission via Cascade förster Energy Transfer in (Ga, In)N Quantum Well/Polymer blend Hybrid Structures. *Nanotechnology*, 275207(20), **2009**. http://link.aps.org/doi/10.1103/PhysRevB.76.035344.

[16] S. Chanyawadee, P. G. Lagoudakis, R. T. Harley, D. G. Lidzey, and M. Henini. Nonradiative Exciton Energy Transfer in Hybrid Organic-Inorganic Heterostructures. *Physical Review B*, 77:193402, **2008**. http://link.aps.org/doi/10.1103/PhysRevB.77.193402.

[17] S. Blumstengel, S. Sadofev, C. Xu, J. Puls, and F. Henneberger. Converting Wannier into Frenkel Excitons in an Inorganic/Organic Hybrid Semiconductor Nanostructure. *Physical Review Letters*, 97:237401, **2006**. http://link.aps.org/doi/10.1103/PhysRevLett.97.237401.

[18] S. Blumstengel, S. Sadofev, and F. Henneberger. Electronic Coupling of Optical Excitations in Organic/Inorganic Semiconductor Hybrid Structures. *New Journal of Physics*, 10(6):065010, **2008**. http://stacks.iop.org/1367-2630/10/i=6/a=065010.

[19] R. Smith, B. Liu, J. Bai, and T. Wang. Hybrid III-nitride/Organic Semiconductor Nanostructure with High Efficiency Nonradiative Energy Transfer for White Light Emitters. *Nano Letters*, 13(7):3042–3047, **2013**. http://dx.doi.org/10.1021/nl400597d.

[20] V. M. Agranovich, G. C. La Rocca, and F. Bassani. Organic-Inorganic Interfaces and Microcavities with Hybrid Excitons. *Pure and Applied Optics: Journal of the European Optical Society Part A*, 7(2):119, **1998**. http://dx.doi.org/http://stacks.iop.org/0963-9659/7/i=2/a=002.

[21] D. Basko, G. C. La Rocca, F. Bassani, and V. M. Agranovich. Förster Energy Transfer from a Semiconductor Quantum Well to an Organic Material Overlayer. *The European Physical Journal B - Condensed Matter and Complex Systems*, 8(3):353–362, **1999**. http://dx.doi.org/10.1007/s100510050700.

[22] H. H. Zhang, X. H. Pan, B. Lu, J. Y. Huang, P. Ding, W. Chen, H. P. He, J. G. Lu, S. S. Chen, and Z. Z. Ye. Mg Composition dependent band offsets of $Zn_{1-x}Mg_xo$/ZnO Heterojunctions. *Phys. Chem. Chem. Phys.*, 15:11231–11235, **2013**. http://dx.doi.org/10.1039/C3CP51156A.

[23] Andrey A. Lutich, Guoxin Jiang, Andrei S. Susha, Andrey L. Rogach, Fernando D. Stefani, and Jochen Feldmann. Energy Transfer versus Charge Separation in Type-II Hybrid Organic/Inorganic Nanocomposites. *Nano Letters*, 9(7):2636–2640, **2009**. http://dx.doi.org/10.1021/nl900978a.

[24] K. Ema, M. Inomata, Y. Kato, H. Kunugita, and M. Era. Nearly Perfect Triplet-Triplet Energy Transfer from Wannier Excitons to Naphthalene in Organic-Inorganic Hybrid Quantum-Well Materials. *Physical Review Letters*, 100:257401, Jun **2008**. http://link.aps.org/doi/10.1103/PhysRevLett.100.257401.

[25] M. Tabachnyk, B. Ehrler, S. Glinas, B. J. Böhm, M. L. andWalker, K. P. Musselman, N. C. Greenham, R. H. Friend, and A. Rao. Resonant Energy Transfer of Triplet Excitons from Pentacene to PbSe Nanocrystals. *Nature Materials*, 13, Aug **2014**. http://www.nature.com/nmat/journal/v13/n11/full/nmat4093.html.

[26] M. Achermann, A. M. Petruska, D. D. Koleske, M. H. Crawford, and V. I. Klimov. Nanocrystal-Based Light-Emitting Diodes Utilizing High-Efficiency Nonradiative Energy Transfer for Color Conversion. *Nano Letters*, 6(7):1396–1400, **2006**. http://dx.doi.org/10.1021/nl060392t.

[27] S. Blumstengel, S. Sadofev, J. Puls, and F. Henneberger. An Inorganic/Organic Semiconductor "Sandwich" Structure Grown by Molecular Beam Epitaxy. *Advanced Materials*, 21(47):4850–4853, **2009**. http://dx.doi.org/10.1002/adma.200900703.

[28] S. Blumstengel, S. Sadofev, H. Kirmse, and F. Henneberger. Extreme Low-Temperature Molecular Beam Epitaxy of ZnO-based Quantum Structures. *Applied Physics Letters*, 98(3), **2011**. http://scitation.aip.org/content/aip/journal/apl/98/3/10.1063/1.3544575.

[29] S. Blumstengel, N. Koch, S. Duhm, H. Glowatzky, R. L. Johnson, C. Xu, A. Yassar, J. P. Rabe, and F. Henneberger. Morphology, Interfacial Electronic Structure, and Optical Properties of Oligothiophenes grown on ZnSe(100) by Molecular Beam Deposition. *Physical Review B*, 73:165323, **2006**. http://link.aps.org/doi/10.1103/PhysRevB.73.165323.

[30] S. Sadofev, S. Blumstengel, J. Cui, J. Puls, S. Rogaschewski, P. Schaefer, Yu.G. Sadofyev, and F. Henneberger. Growth of High-Quality ZnMgO Epilayers and ZnO/ZnMgO Quantum Well Structures by Radical-Source Molecular-Beam Epitaxy on Sapphire. *Applied Physics Letters*, 87(9), **2005**. http://dx.doi.org/10.1063/1.2034113.

[31] S. Blumstengel, S. Sadofev, C. Xu, J. Puls, R. L. Johnson, H. Glowatzki, N. Koch, and F. Henneberger. Electronic Coupling in Organic-Inorganic Semiconductor Hybrid Structures with type-II Energy Level Alignment. *Physical Review B*, 77:085323, **2008**. http://link.aps.org/doi/10.1103/PhysRevB.77.085323.

[32] Y. Wu, J. Zhang, Z. Fei, and Z. Bo. Spiro-Bridged Ladder-Type Poly(p-phenylene)s: Towards Structurally Perfect Light-Emitting Materials. *Journal of the American Chemical Society*, 130(23):7192–7193, **2008**. http://dx.doi.org/10.1021/ja801422n.

[33] L. Liu, S. Tang, M. Liu, M. Xie, W. Zhang, P. Lu, M. Hanif, and Y. Ma. Photodegradation of Polyfluorene and Fluorene Oligomers with Alkyl and Aromatic Disubstitutions. *The Journal of Physical Chemistry B*, 110(28):13734–13740, **2006**. http://dx.doi.org/10.1021/jp062612x.

[34] J. Jacob, S. Sax, M. Gaal, E. J. W. List, A. C. Grimsdale, and K. Müllen. A Fully Aryl-Substituted Poly(ladder-type pentaphenylene): A Remarkably Stable Blue-Light-Emitting Polymer. *Macromolecules*, 38(24):9933–9938, **2005**. http://dx.doi.org/10.1021/ma0517143.

[35] U. Scherf and K. Müllen. Polyarylenes and poly(arylenevinylenes),7. A Soluble Ladder Polymer via Bridging of Functionalized poly(p-phenylene)-precursors. *Die Makromolekulare Chemie, Rapid Communications*, 12(8):489–497, **1991**. http://dx.doi.org/10.1002/marc.1991.030120806.

[36] B. Kobin, L. Grubert, S. Blumstengel, F. Henneberger, and S. Hecht. Vacuum-Processable Ladder-type Oligophenylenes for Organic-Inorganic Hybrid structures: Synthesis, Optical and Electrochemical Properties upon Increasing Planarization as Well as Thin Film Growth. *Journal of Materials Chemistry*, 22:4383–4390, **2012**. http://dx.doi.org/10.1039/C2JM15868J.

[37] J. Frenkel. On the Transformation of Light into Heat in solids. *Physical Review*, 37:17–44, Jan 1931. http://link.aps.org/doi/10.1103/PhysRev.37.17.

[38] G. H. Wannier. The Structure of Electronic Excitation Levels in Insulating Crystals. *Physical Review*, 52:191–197, **1937**. http://link.aps.org/doi/10.1103/PhysRev.52.191.

[39] F. Bassani, G. C. La Rocca, D. M. Basko, and V. M. Agranovich. Excitons in HybridOrganic-Inorganic Nanostructures. *Physics of the Solid State*, 41(5):701–703, **1999**. http://dx.doi.org/10.1134/1.1130852.

[40] S. Pearton. *GaN and ZnO-based Materials and Devices*. **2012**. Springer-Verlag.

[41] E. Rosencher and V. Borge. *Optoelectronics*. 1st edition edition, May **2002**. Cambridge University Press.

[42] L. Bergman and J. L. McHale. *Handbook of Luminescent Semiconductor Materials*. CRC Press, 7 Sebember **2011**.

[43] G. Bastard. *Wave Mechanics Applied to Semiconductor Heterostructures*. **1990**. Wiley-Interscience.

[44] C. J. Bardeen. The Structure and Dynamics of Molecular Excitons. *Annual Review of Physical Chemistry*, 65(1):127–148, **2014**. http://dx.doi.org/10.1146/annurev-physchem-040513-103654.

[45] S. Wolf. *Organic Molecular Solids*. **2006**. Vch Verlagsgesellschaft Mbh.

[46] M. Grundmann. *The Physics of Semiconductors: An Introduction Including Devices and Nanophysics*. 3rd edition edition, December **2015**. Springer-Verlag.

[47] B.R. Nag. *Physics of Quantum Well Devices*. **2002**. Kluwer Academic Print on Demand.

[48] D. A. B. Miller. *Optical Physics of Quantum Wells*.

[49] Litton Cole W., Reynolds Donald C., and Collins Thomas C. *Zinc Oxide Materials for Electronic and Optoelectronic Device Applications*.

[50] G. Bastard, C. Delalande, M. H. Meynadier, P. M. Frijlink, and M. Voos. Low-Temperature Exciton trapping on interface defects in Semiconductor Quantum Wells. *Physical Review B*, 29:7042–7044, Jun **1984**. http://link.aps.org/doi/10.1103/PhysRevB.29.7042.

[51] M. Hadis. *Zinc Oxide Fundamentals, Materials and Device Technology*.

[52] C. Klingshirn. ZnO: Material, Physics and Applications. *ChemPhysChem*, 8(6):782–803, **2007**. http://dx.doi.org/10.1002/cphc.200700002.

[53] W. J. Fan, J. B. Xia, P. A. Agus, S. T. Tan, S. F. Yu, and X. W. Sun. Band Parameters and Electronic Structures of Wurtzite ZnO and ZnO/MgZnO Quantum Wells. *Journal of Applied Physics*, 99(1), **2006**. http://dx.doi.org/10.1063/1.2150266.

[54] D. G. Thomas. The Exciton Spectrum of Zinc Oxide. *J. Phys. Chem. Solids*, 86-96(15), **1960**. http://www.sciencedirect.com/science/article/pii/0022369760901049.

[55] J. Fraxedas. *Molecular Organic Materials: From Molecules to Crystalline Solids*. 1st edition edition, June **2008**. Cambridge University Press.

[56] Peter Atkins and Ronald Friedman. *Molecular Quantum Mechanics*. 5th edition, November **2010**. OUP Oxford.

[57] W. Brütting. *Physics of Organic Semiconductors*. 2nd edition edition, **2012**. Wiley-VCH.

[58] J. R. Lakowicz. *Principles of Fluorescence Spectroscopy*. 3rd edition edition, August **2006**. Springer-Verlag.

[59] R. S. Swathi and K. L. Sebastian. Distance Dependence of Fluorescence Resonance Energy Transfer. *Journal of Chemical Sciences*, 121(5):777–787, **2009**. http://dx.doi.org/10.1007/s12039-009-0092-x.

[60] T. Förster. Zwischenmolekulare Energiewanderung und Fluoreszenz. *Annalen der Physik*, 437(1-2):55–75, 1948. http://dx.doi.org/10.1002/andp.19484370105.

[61] I. Medintz and N. Niko Hildebrandt. *FRET - Förster Resonance Energy Transfer: From Theory to Applications*. 1st edition edition, **2013**. Wiley-VCH.

[62] V. May and O. Kuhn. *Charge and Energy Transfer Dynamics in Molecular Systems*. **2004**. Vch Pub.

[63] H. Kuhn. Classical Aspects of Energy Transfer in Molecular Systems. *The Journal of Chemical Physics*, 53(1):101–108, **1970**. http://scitation.aip.org/content/aip/journal/jcp/53/1/10.1063/1.1673749.

[64] J. J. Rindermann, G. Pozina, B. Monemar, L. Hultman, H. Amano, and P. G. Lagoudakis. Dependence of Resonance Energy Transfer on Exciton Dimensionality. *Physical Review Letters*, 107:236805, **2011**. http://link.aps.org/doi/10.1103/PhysRevLett.107.236805.

[65] J. J. Rindermann, G. Pozina, B. Monemar, L. Hultman, H. Amano, and P. G. Lagoudakis. The Effect of Exciton Dimensionality on Resonance Energy Transfer: Advances for Organic Color Converters in Hybrid Inorganic/Organic LEDs, **2012**. http://dx.doi.org/10.1117/12.908339.

[66] D. M. Basko, G. C. La Rocca, F. Bassani, and V. M. Agranovich. Interaction of Quantum Well Excitons with a Resonant LocalizedExcitation. *Physical Review B*, 71, Apr **2005**. http://link.aps.org/doi/10.1103/PhysRevB.71.165330.

[67] B. K. Meyer, J. Sann, S. Eisermann, S. Lautenschlaeger, M. R. Wagner, M. Kaiser, G. Callsen, J. S. Reparaz, and A. Hoffmann. Excited State Properties of Donor Bound Excitons in ZnO. *Physical Review B*, 82:115207, Sep **2010**. http://link.aps.org/doi/10.1103/PhysRevB.82.115207.

[68] G. Margaritondo. *Electronic Structure of Semiconductor Heterojunctions*, volume 1. Springer Netherlands, reprint edition, **1988**. Springer-Verlag.

[69] Harald Ibach. *Physics of Surfaces and Interfaces*. 1st edition, **2006**. Springer-Verlag Berlin Heidelberg.

[70] L. Hans. *Solid Surfaces, Interfaces and Thin Films*. 5th edition edition, **2012**. Springer-Verlag.

[71] M. Eyer, S. Sadofev, J. Puls, and S. Blumstengel. Charge Transfer Excitons at ZnMgO/P3HT Heterojunctions: Relation to Photovoltaic Performance. *Applied Physics Letters*, 107(22), **2015**. http://dx.doi.org/10.1063/1.4936759.

[72] H. Kim, Z.-L. Guan, Q. Sun, A. Kahn, J. Han, and A. Nurmikko. Surface and Interface States of Gallium-polar versus Nitrogen-polar GaN: Impact of thin Onorganic Semiconductor Overlayers. *Journal of Applied Physics*, 113707(107), **2010**.

[73] S. Rangan, S. Katalinic, R. Thorpe, R. A. Bartynski, J. Rochford, and E. Galoppini. Energy Level Alignment of a Zinc(II) Tetraphenylporphyrin Dye Adsorbed onto TiO2(110) and ZnO(11 − 20) Surfaces. *The Journal of Physical Chemistry C*, 114(2):1139–1147, **2010**. http://dx.doi.org/10.1021/jp909320f.

[74] S. H. Park, H. J. Kim, M.-H. Cho, Y. Yi, S. W. Cho, J. Yang, and H. Kim. The Effect of ZnO Surface Conditions on the Electronic Structure of the ZnO/CuPc Interface. *Applied Physics Letters*, 98(8), **2011**. http://scitation.aip.org/content/aip/journal/apl/98/8/10.1063/1.3555440.

[75] R. J. Davis, M. T. Lloyd, S. R. Ferreira, M. J. Bruzek, S. E. Watkins, L. Lindell, P. Sehati, M. Fahlman, J. E. Anthony, and J. W. P. Hsu. Determination of Energy Level Alignment at Interfaces of Hybrid and Organic Solar Cells under Ambient Environment. *Journal of Materials Chemistry*, 21:1721–1729, **2011**. http://dx.doi.org/10.1039/C0JM02349C.

[76] M. Schneider, E. Umbach, A. Langner, and M. Sokolowski. Luminescence of Molecules Adsorbed on Surfaces of Wide Gap Materials. *Journal of Luminescence*, 110(4):275–283, **2004**. http://www.sciencedirect.com/science/article/pii/S0022231304002601.

[77] D. W. Jennings and K. Weispfennig. Experimental Solubility data of Various n-Alkane Waxes: Effects of Alkane Chain length, Alkane odd versus Even Carbon number Structures, and Solvent Chemistry on Solubility. *Fluid Phase Equilibria*, 227(1), **2005**. http://dx.doi.org/10.1016/j.fluid.2004.10.021.

[78] R. Abbel, M. Wolffs, R. A. A. Bovee, J. L. J. van Dongen, X. Lou, O. Henze, W. J. Feast, E. W. Meijer, and A. P. H. J. Schenning. Side-Chain Degradation of Ultrapure-Conjugated Oligomers: Implications for Organic Electronics. *Advanced Materials*, 21(5):597–602, **2009**. http://dx.doi.org/10.1002/adma.200802416.

[79] S. Sadofev, P. Schäfer, Y.-H. Fan, S. Blumstengel, F. Henneberger, D. Schulz, and D. Klimm. Radical-Source Molecular beam Epitaxy of ZnMgO and ZnCdO alloys on ZnO Substrates. *Applied Physics Letters*, **2007**. http://dx.doi.org/10.1063/1.2815662.

[80] Stephen R. Forrest. Ultrathin Organic Films Grown by Organic molecular Beam Deposition and Related Techniques. *Chemical Reviews*, 97(6):1793–1896, **1997**. http://dx.doi.org/10.1021/cr941014o.

[81] E. Mohajerani, F. Farajollahi, R. Mahzoon, and S. Baghery. Morphological and Thickness Analysis for PMMA Spin Coated Films.

[82] Raphael Schlesinger. *Energy-Level Control at Hybrid Inorganic/Organic Semiconductor Interfaces*. 1st edition, **2016**. Springer Theses.

[83] G. Itskos, A. Othonos, S. A. Choulis, and E. Iliopoulos. Förster Resonant Energy Transfer from an Inorganic Quantum Well to a Molecular Material: Unexplored Aspects, Losses, and Implications to Applications. *The Journal of Chemical Physics*, 143(21), **2015**.

[84] U. Scherf and E. J. W. List. Semiconducting Polyfluorenes-Towards Reliable Structure-Property Relationships. *Advanced Materials*, 14(7):477–487, **2002**. http://onlinelibrary.wiley.com/doi/10.1002/1521-4095(20020404)14:7⟨477::AID-ADMA477⟩3.0.CO;2-9/abstract.

[85] L. Linlin, Q. Song, W. Baoling, W. Huan, X. Zengqi, and M. Yuguang. Morphology and Optical Properties of Fluorene-Based Ladder-type Poly(paraphenylenes): Origin of Low-Energy Emission. *The Journal of Physical Chemistry C*, 113(14):5799–5804, **2009**. http://dx.doi.org/10.1021/jp8090733.

[86] E. Zojer, A. PogZojer, E. Hennebicq, D. Beljonne, J. Brdas, P. Scandiucci de Freitas, U. Scherf, and E. J. W. List. Green Emission from poly(fluorene)s: The Role of Oxidation. *The Journal of Chemical Physics*, 117(14):6794–6802, **2002**. http://scitation.aip.org/content/aip/journal/jcp/117/14/10.1063/1.1507106.

[87] L. Romaner, G. Heimel, H. Wiesenhofer, P. Scandiucci de F., U. Scherf, J.-L. Brdas, E. Zojer, , and E. J. W. List. Ketonic Defects in Ladder-type Poly(p-phenylene)s. *Chemistry of Materials*, 16(23):4667–4674, **2004**. http://dx.doi.org/10.1021/cm0496164.

[88] W. Zhao, T. Cao, and J.?M. White. On the Origin of Green Emission in Polyfluorene Polymers: The Roles of Thermal Oxidation Degradation and Crosslinking. *Advanced Functional Materials*, 14(8):783–790, **2004**. http://dx.doi.org/10.1002/adfm.200305173.

[89] U. V. Mallavadhani and N. Fleury-Bregeot. *Encyclopedia of Reagents for Organic Synthesis*. John Wiley and Sons, **2001**.

[90] M. Höfner, B. Kobin, S. Hecht, and F. Henneberger. Strong Coupling and Laser Action of Ladder-Type Oligo(pphenylene)s in a Microcavity. *ChemPhysChem*, 15, **2014**.

[91] M. Sparenberg, A. Zykov, P. Beyer, L. Pithan, C. Weber, Y. Garmshausen, F. Carl, S. Hecht, S. Blumstengel, F. Henneberger, and S. Kowarik. Controlling the Growth Mode of Para-Sexiphenyl (6P) on ZnO by Partial Fluorination. *Physical Chemistry Chemical Physics*, 16, **2014**. http://www.ncbi.nlm.nih.gov/pubmed/25361069.

[92] Y. Xu, O. T. Hofmann, R. Schlesinger, S. Winkler, J. Frisch, J. Niederhausen, A. Vollmer, S. Blumstengel, F. Henneberger, N. Koch, P. Rinke, and M. Scheffler. Space-Charge Transfer in Hybrid Inorganic-Organic Systems. *Physical Review Letters*, 111:226802, **2013**. http://link.aps.org/doi/10.1103/PhysRevLett.111.226802.

[93] M. Kemerink, S. F. Alvarado, P. Müller, P. M. Koenraad, H. W. M. Salemink, J. H. Wolter, and R. A. J. Janssen. Scanning Tunneling Spectroscopy on Organic semiconductors: Experiment and Model. *Physical Review B*, 70:045202, **2004**. http://link.aps.org/doi/10.1103/PhysRevB.70.045202.

[94] T. Makino, C. H. Chia, Nguen T. Tuan, H. D. Sun, Y. Segawa, M. Kawasaki, A. Ohtomo, K. Tamura, and H. Koinuma. Room-Temperature LuminescenceOf Excitons in ZnO/(Mg,Zn)o Multiple Quantum Wells on Lattice-Matched Substrates. *Applied Physics Letters*, 77(7), **2000**. http://dx.doi.org/10.1063/1.1289066.

[95] W. F. Yang, R. Chen, B. Liu, L. M. Wong, S. J. Wang, and H. D. Sun. Temperature Dependence of Weak localization Effects of Excitons in ZnMgO/ZnO single Quantum Well.

[96] M. Grundmann and C. P. Dietrich. Lineshape Theory of Photoluminescence from Semiconductor Alloys. *Journal of Applied Physics*, 106(12), **2009**. http://dx.doi.org/10.1063/1.3267875,.

[97] D. Bimberg, M. Sondergeld, and E. Grobe. Thermal Dissociation of Excitons Bounds to Neutral Acceptors in High-Purity GaAs. *Physical Review B*, 4:3451–3455, Nov **1971**. http://link.aps.org/doi/10.1103/PhysRevB.4.3451.

[98] D. G. Chtchekine, Z. C. Feng, S. J. Chua, and G. D. Gilliland. Temperature-varied Photoluminescence and Magnetospectroscopy study of near-band-edge Emissions in GaN. *Physical Review B*, 63:125211, Mar **2001**. http://link.aps.org/doi/10.1103/PhysRevB.63.125211.

[99] M. Hideaki, Y. Yoichi, T. Tsunemasa, I. Akihiko, K. Yasutoshi, and Toshiya. Y. Temperature Dependence of Localized exciton Transitions in AlGaN Ternary Alloy Epitaxial Layers. *Journal of Applied Physics*, 104(5), **2008**. http://dx.doi.org/10.1063/1.2975970.

[100] S. F. Chichibu, T. Onuma, M. Kubota, A. Uedono, T. Sota, A. Tsukazaki, A. Ohtomo, and M. Kawasaki. Improvements in Quantum Efficiency of Excitonic Emissions in ZnO Epilayers by the Elimination of Point Defects. *Journal of Applied Physics*, 99(9):2636–2640, **2006**. http://scitation.aip.org/content/aip/journal/jap/99/9/10.1063/1.2193162.

[101] Y. Zhong, A. B. Djurii, Y. F. Hsu, K. S. Wong, G. Brauer, C. C. Ling, and W. K. Chan. Exceptionally Long Exciton Photoluminescence Lifetime in ZnO Tetrapods. *The Journal of Physical Chemistry C*, 112(42):16286–16295, **2008**. http://dx.doi.org/10.1021/jp804132u.

[102] N. Kedem, S. Blumstengel, F. Henneberger, H. Cohen, H. Hodes, and D. Cahen. Morphology-, Synthesis- and Doping Independent Tuning of ZnO Work Function using Phenylphosphonates. *Phys. Chem. Chem. Phys.*, 8310(16), **2014**.

[103] O. T. Hofmann, J.-C. Deinert, Y. Xu, P.k Rinke, J. Stähler, M. Wolf, and M. Scheffler. Large Work Function Reduction by Adsorption of a Molecule with a Negative Electron Affinity: Pyridine on ZnO(101-0). *The Journal of Chemical Physics*, 139(17), **2013**. http://scitation.aip.org/content/aip/journal/jcp/139/17/10.1063/1.4827017.

[104] C. R. McNeill, A. Abrusci, J. Zaumseil, R.d Wilson, M. J. McKiernan, J. H. Burroughes, J. J. M. Halls, N. C. Greenham, and R. H. Friend. Dual Electron Donor/Electron Acceptor Character of a Conjugated Polymer in Efficient Photovoltaic Diodes. *Applied Physics Letters*, 90(19), **2007**. http://scitation.aip.org/content/aip/journal/apl/90/19/10.1063/1.2738197.

[105] Y. Itzhaik, G. Hodes, and H. Cohen. Band Alignment and Internal Field Mapping in Solar Cells. *The Journal of Physical Chemistry Letters*, 2(22):2872–2876, **2011**. http://dx.doi.org/10.1021/jz201265z.

[106] B. Kobin, L. Grubert, S. Mebs, B. Braun, and S. Hecht. Gradual Fluorination of Ladder-type Quarterphenyl. *Israel Journal of Chemistry*, 54(5-6):789–795, **2014**. http://dx.doi.org/10.1002/ijch.201400044.

[107] S. Guo, S. B. Kim, S. K. Mohapatra, Y. Qi, T. Sajoto, A. Kahn, S. R. Marder, and S. Barlow. n-doping of Organic Electronic Materials using Air-Stable Organometallics. *Advanced Material*, 24:699–703, **2012**. http://dx.doi.org/10.1002/adma.201103238.

[108] S. Guo, S. K. Mohapatra, A. Romano, T. V. Timofeeva, K. I. Hardcastle, K. Yesudas, C. Risko, J. L. Bredas, S. R. Marder, and S. Barlow. n-doping of Organic Electronic Materials using Air-Stable Organometallics: A Mechanistic Study of Reduction by Dimeric Sandwich Compounds. *Chem. Eur. J.* 10.1002/chem.20120259.

[109] A. J. Giordano, F. Pulvirenti, T. M. Khan, C. Fuentes-Hernandez, K. Moudgil, J. H. Delcamp, B. Kippelen, S. Barlow, and S. R. Marder. Organometallic Dimers: Application to Work-Function Reduction of Conducting Oxides. *ACS Applied Materials & Interfaces*, (7):4320–4326, **2015**. http://dx.doi.org/10.1021/am5087648.

[110] S. Olthof, S. Mehraeen, S. K. Mohapatra, S. Barlow, V. Coropceanu, J.-L. Brédas, S. R. Marder, and A. Kahn. Ultralow Doping in Organic Semiconductors: Evidence of Trap Filling. *Physical Review Letters*, 109:176601, Oct **2012**. http://link.aps.org/doi/10.1103/PhysRevLett.109.176601.

[111] P. Amsalem, J. Niederhausen, A. Wilke, G. Heimel, R. Schlesinger, S. Winkler, A. Vollmer, J. P. Rabe, and N. Koch. Role of harge Transfer, dipole-dipole interactions, and Electrostatics in Fermi-level pinning at a Molecular Heterojunction on a Metal Surface. *Physical Review B*, 87:035440, **2013**. http://dx.doi.org/10.1103/PhysRevB.87.035440.

[112] P. J. Hotchkiss, S. H. Jones, S. A. Paniagua, A. Sharma, B. Kippelen, N. R. Armstrong, and S. R. Marder. The Modification of Indium Tin Oxide with Phosphonic Acids: Mechanism of Binding, Tuning of Surface Properties, and Potential for Use Inorganic Electronic Applications. *Accounts of Chemical Research*, 45(3):337–346, **2012**. http://dx.doi.org/10.1021/ar200119g,.

[113] Y. Zhou, C. Fuentes-Hernandez, J. Shim, J. Meyer, A. J. Giordano, H. Li, P. Winget, T. Papadopoulos, H. Cheun, J. Kim, M. Fenoll, A. Dindar, W. Haske, E. Najafabadi, T. M. Khan, H. Sojoudi, S. Barlow, S. Graham, J.-L. Brédas, S. R. Marder, A. Kahn, and B. Kippelen. A Universal Method to Produce Low–Work Function Electrodes for Organic Electronics. *Science*, 336(6079):327–332, **2012**. http://science.sciencemag.org/content/336/6079/327.

[114] R. Schlesinger, Y. Xu, O. T. Hofmann, S. Winkler, J. Frisch, J. Niederhausen, A. Vollmer, S. Blumstengel, F. Henneberger, Pa. Rinke, M. Scheffler, and N. Koch. Controlling the Work function of ZnO and the Energy-Level Alignment at the Interface to Organic semiconductors with a Molecular Electron Acceptor. *Physical Review B*, 87:155311, **2013**.

[115] R. T. Tung. The Physics and Chemistry of the Schottky Barrier Height. *Applied Physics Reviews*, 1, **2014**. http://scitation.aip.org/content/aip/journal/apr2/1/1/10.1063/1.4858400.

[116] Ye Eun Ha, Mi Young Jo, Juyun Park, Yong-Cheol Kang, Seong Il Yoo, and Joo Hyun Kim. Inverted Type Polymer Solar Cells with Self-Assembled Monolayer Treated ZnO. *The Journal of Physical Chemistry C*, 117(6):2646–2652, **2013**. http://dx.doi.org/10.1021/jp311148d.

[117] M. Timpel, M. V. Nardi, G. Ligorio, B. Wegner, M. Pätzel, B. Kobin, S. Hecht, and N. Koch. Energy-Level Engineering at ZnO-Oligophenylene Interfaces with Phosphonate-Based Self-Assembled Monolayers. *ACS Appl. Mater. Interfaces*, 7, **2015**. http://pubs.acs.org/doi/abs/10.1021/acsami.5b01669.

[118] O. V. Gusev, M. A. Ievlev, M. G. Peterleitner, S. M. Peregudova, L. I. Denisovich, P. V. Petrovskii, and N. A. Ustynyuk. Reduction of Ruthenium Arenecyclopentadienyl Complexes Reactions Induced by Electron Transfer. *Journal of Organometallic Chemistry*, 534, **1997**. http://www.sciencedirect.com/science/article/pii/S0022328X9606888X.

[119] M. T. Greiner, M. G. Helander, Tang W.-M., Z.-B. Wang, J. Qiu, and Z.-H. Lu. Universal Energy-Level Alignment of Molecules on Metal Oxides. *Nature Materials*, 11:76–81, **2012**. http://www.nature.com/nmat/journal/v11/n1/pdf/nmat3159.pdf.

[120] W. Gao and A. Kahn. Electronic Structure and Current Injection in Zinc Phthalocyanine doped with Tetrafluorotetracyanoquinodimethane: Interface versus Bulk Effects. *Organic Electronics*, 3(2):53–63, **2002**. http://www.sciencedirect.com/science/article/pii/S1566119902000332.

[121] H. Wang, P. Amsalem, G. Heimel, I. Salzmann, N. Koch, and M. Oehzelt. Band-Bending in Organic Semiconductors: the Role of Alkali-Halide Interlayers. *Advanced Materials*, 26(6):925–930, **2014**. http://dx.doi.org/10.1002/adma.201303467.

[122] A. Bakin, A. El-Shaer, A. C. Mofor, M. Al-Suleiman, E. Schlenker, and A. Waag. ZnMgO-ZnO Quantum Wells Embedded in ZnO Nanopillars: Towards Realisation of nano-LEDs. *Physica status solidi (c)*, 4(1):158–161, **2007**. http://dx.doi.org/10.1002/pssc.200673557.

[123] Hui Wang, Yang Zhao, Chao Wu, Xin Dong, Baolin Zhang, Guoguang Wu, Yan Ma, and Guotong Du. Ultraviolet Electroluminescence from n-ZnO/NiO/p-GaN Light-Emitting diode Fabricated by MOCVD. *Journal of Luminescence*, 158:6–10, **2015**. http://dx.doi.org/10.1016/j.jlumin.2014.09.007.

[124] L. Zhang, Q. Li, L. Shang, F. Wang, C. Qu, and F. Zhao. Improvement of UV Electroluminescence of nZnO/p-GaN Heterojunction LED by ZnS Interlayer. *Opt Express.*, **2013**. http://www.ncbi.nlm.nih.gov/pubmed/23938509.